The Dissertation Committee for Li Quan Certifies that this is the approved version of the following Dissertation:

Nonlocality and Willis Coupling in Acoustic Metamaterials and Metasurfaces

Committee:

Andrea Alù, Supervisor

Mark F. Hamilton

Neal A. Hall

Mikhail Belkin

Michael R. Haberman

Nonlocality and Willis Coupling in Acoustic Metamaterials and Metasurfaces

by

Li Quan

Dissertation

Presented to the Faculty of the Graduate School of

The University of Texas at Austin

in Partial Fulfillment

of the Requirements

for the Degree of

Doctor of Philosophy

The University of Texas at Austin

May 2020

Dedication

To my wife Yaodan, and my mom Guozhen.

ACKNOWLEDGEMENTS

Coming to the United States to study for my Ph.D. is an important decision in my life. I could still clearly remember the scenario five years ago at the airport on the day I was traveling and how reluctant I was to leave my family. Time flies, and now I have finished my Ph.D. study and reached a milestone in my career. Looking back to the past, so many people offered me great support during this journey, and its time to express my gratitude to them.

Having a good advisor is essentially important for a graduate student, and I am among one of the luckiest students who made this. So first of all, I would like to express my sincere gratitude to my advisor, Prof. Andrea Alù. Prof. Alù is one of the leading researchers in the field of metamaterials in the world and I am proud of being one of the members in his group. He never hesitated to involve me in his impactful research and always shares his idea and knowledge with me during the past five years. Without his constant guidance, I could not achieve my fruitful research accomplishments and have my work be recognized in the field. Prof. Alù's support and encouragement not only exist in my research but also in my daily life. So many things happened during the past five years, Prof. Alù is always the first one I would seek help from, and from him, I could always get tremendous support, which I deeply appreciate.

I am also thankful to Prof. Mark F. Hamilton, from whom I took four graduate acoustic courses. Without exaggeration, most of my basic knowledge in acoustics is from Prof. Hamilton. I would also like to express my thankfulness to Prof. Hamilton for his

significant help during my US immigration and job applications. I am grateful to Prof. Michael R. Haberman, who had shared with me many experiences and provided me continuous support in my immigration and job applications. I thank Prof. Dimitrios Sounas from Wayne State University, the former postdoc and research scientist in our group, for his constant guidance, support and input in multi-projects we have collaborated and his support during my job application. I would also thank Prof. Mikhail Belkin and Prof. Neal A. Hall for agreeing to be my committee members and willing to review my Ph.D. work.

My labmates and friends make my Ph.D. journey meaningful. Special thanks to my American friends Matthew Byrne, Curtis Wiederhold, and Robert Duggan, who help proofread and provide input in many of my drafts. I would also like to thank Zhicheng Xiao, Chenyang Luo and Liuyang Sun for their support in my move. I also thank Mykhailo Tymchenok, Yarden Mazor, Ahmed Kord, Hoyeong Kown, Yoshiaki Kasahara, Caleb Sieck, Francesco Monticone, Nasim Mohammadi Estakhri, Hussein Esfahlani, Mohammad-Ali Miri, Juan Sebastian Gomez-Diaz, Younes Radi, Simon Yves, Yugui Peng, Sander Mann, Guangwei Hu, Diego Farfan, with whom I spent great five years.

Finally, I shall not hesitate to thank my wife Yaodan and my mon Guozhen, who loved, supported, accompanied, and encouraged me for so many years and continuous for the rest of my life.

ABSTRACT

Nonlocality and Willis Coupling in Acoustic Metamaterials and Metasurfaces

Li Quan, Ph.D.

The University of Texas at Austin, 2020

Supervisor: Andrea Alù

Acoustic metamaterials and metasurfaces are artificial materials and surfaces composited with meta-atoms and inclusions at the subwavelength scale but behave homogeneously in the macroscopic scale with unusual properties in the manipulation of sound waves. Most of the research in this field has focused so far on the study of the local response of the materials and surface properties but neglected the nonlocality. This dissertation focuses on the study of nonlocal phenomena in acoustics, and explore their unusual abilities in the control and manipulation of sound waves. The dissertation starts with the exploration of pressure-velocity coupling phenomena, also known as Willis coupling or acoustic bianisotropy, in a single subwavelength inclusion and derived general bounds on the Willis response of acoustic scatterers, indicating these bounds can be reached through proper design. A systematic design approach of reciprocal Willis inclusion has been outlined for the realistic implementation of acoustic inclusions with

Willis response from zero, mild to maximum. My study shows that reciprocal Willis responses can be mainly attributed to geometrical asymmetries. By breaking the system's time-reversal symmetry through bias flow, Willis coupling has also been observed in geometry-symmetrical systems. Then, I changed my viewpoint from single inclusion to the collective response of metamaterials at the macroscopic level. By combining moving media with zero-index acoustic propagation, giant bianisotropy and extreme nonreciprocity were achieved in the metamaterials with modest mechanical motion. This special acoustic response was utilized to induce non-reciprocal positive-to-negative sound refraction and the non-reciprocal metamaterial lens which could focus object when the excitation is from a specific side. Finally, the study was extended to metasurface, and explore their unusual properties by considering the strong coupling between neighboring elements. The general impedance relation with the consideration of coupling between neighboring elements was proposed and the mechanism was applied to the design of nonlocal passive metasurfaces which could overcome the limitations of local designs, and achieve unitary efficiency for extreme beam steering. The nonlocal metasurface has also been applied to the design of acoustic hyperbolic metasurface requiring extreme anisotropic impedance which was considered impossible in the local metasurface.

Table of Contents

List of Tables

List of Figures

CHAPTER 1. INTRODUCTION

1.1 Motivation

Sound waves are ubiquitous in our daily life, from common communications with our neighbors to sophisticated surface acoustic wave technology in our electronic gadgets. Strong interactions between matter and sound waves not only provide an extra degree of freedom to manipulate sound waves, but they also offer a useful tool to extract information from unknown bodies. Typical applications are ultrasound imaging used in medical diagnosis [1][2], ultrasonic therapy and drug delivery used in medical treatment [3]-[5], non-destructive testing used in industrial diagnosis [6]-[8], underwater communications [9][10], etc.

Advanced functional materials and metamaterials have been providing new opportunities in acoustics, enabling scientists to explore opportunities in sound-matter interactions that are not available in nature, and discover exotic phenomena and significant applications that were considered impossible in traditional views [11][12]. For example, acoustic metamaterials with negative dynamic bulk modulus and negative dynamic mass can support negative refraction of sound waves [13]-[19], which have a significant impact on sound imaging. Acoustic radiation pattern control, such as sound collimation technologies [20]-[22], have the potential for great applications in medical therapy and drug delivery. Acoustic non-reciprocal metamaterials, which allow asymmetric transmission of sound in opposite propagation directions [23]-[26], have

potential applications in sound communication and noise control. The discovery of acoustic metamaterials is only about two decades old, and several fundamental questions remain unsolved and/or unexplored in the field. However, the design of novel acoustic devices with medical and industrial applications is based on the full understanding of the interaction between matter and sound waves. My research goals during my Ph.D. study are motivated by addressing basic open questions in the explorations of acoustic metamaterials, shedding light on the underlying physical mechanisms behind exotic sound phenomena and design novel acoustic devices with multiple applications.

1.2 From Local Metamaterials to Nonlocal Metamaterials

Designing and exploring materials with special properties has been of interest throughout human development. In ancient times, our ancestors recovered different metals from ores and through metalworking, employed them into people's daily life, which greatly changed the pace of human development, resulting in historic phrases such as Stone Age, Bronze Age, Iron Age, and Steel Age. With the development of science and technology, the research and exploration of materials gradually change from materials found naturally to artificial materials. The study of artificial materials for the manipulation of waves has a very long time history and can be traced back to the end of the 19^{th} century. In 1898, Jagadis Chunder Bose researched substance with chiral properties, which was considered as some of the earliest explorations of metamaterials [27]. In 1968, Viktor Veselago first theoretically studied the wave propagation properties

of negative-index materials and proposed the concept of negative refraction [28]. However, due to the technical limitations, his proposal did not cause much attention at that time. The practical way to achieve negative permeability was firstly identified by John Pendry [29], resulting in the experimental realization of left-handed metamaterials and negative refraction [30]. With extreme potential applications in high-resolution imaging [31], the researches of metamaterials continue to flourish [32]-[42].

The researches in the field of acoustic metamaterials were extended from electromagnetic metamaterials and began in 2000 [13]. After that, the exploration of acoustic metamaterials with negative density and negative bulk modulus becomes a hot topic [43]-[47]. Other topics explored at the same time in the fields also including acoustic cloak [48]-[51], acoustic superlens [52][53], anisotropic mass density [54][55], etc. All the acoustic metamaterials mentioned before could be summarized in Fig. 1.1. In acoustics, the propagation of sound waves is governed by two equations, the mass conservation law, and the momentum law:

$$\nabla \cdot \vec{v} + \kappa \frac{\partial p}{\partial t} = 0 \tag{1.1}$$

$$\nabla p + \rho \frac{\partial \vec{v}}{\partial t} = 0 \tag{1.2}$$

Here p, $\vec{v}$, κ, and ρ indicate acoustic pressure, particle velocity, material compressibility, and density, respectively. And the speed of sound can be express as

$$c = \frac{1}{\sqrt{\rho\kappa}} \tag{1.3}$$

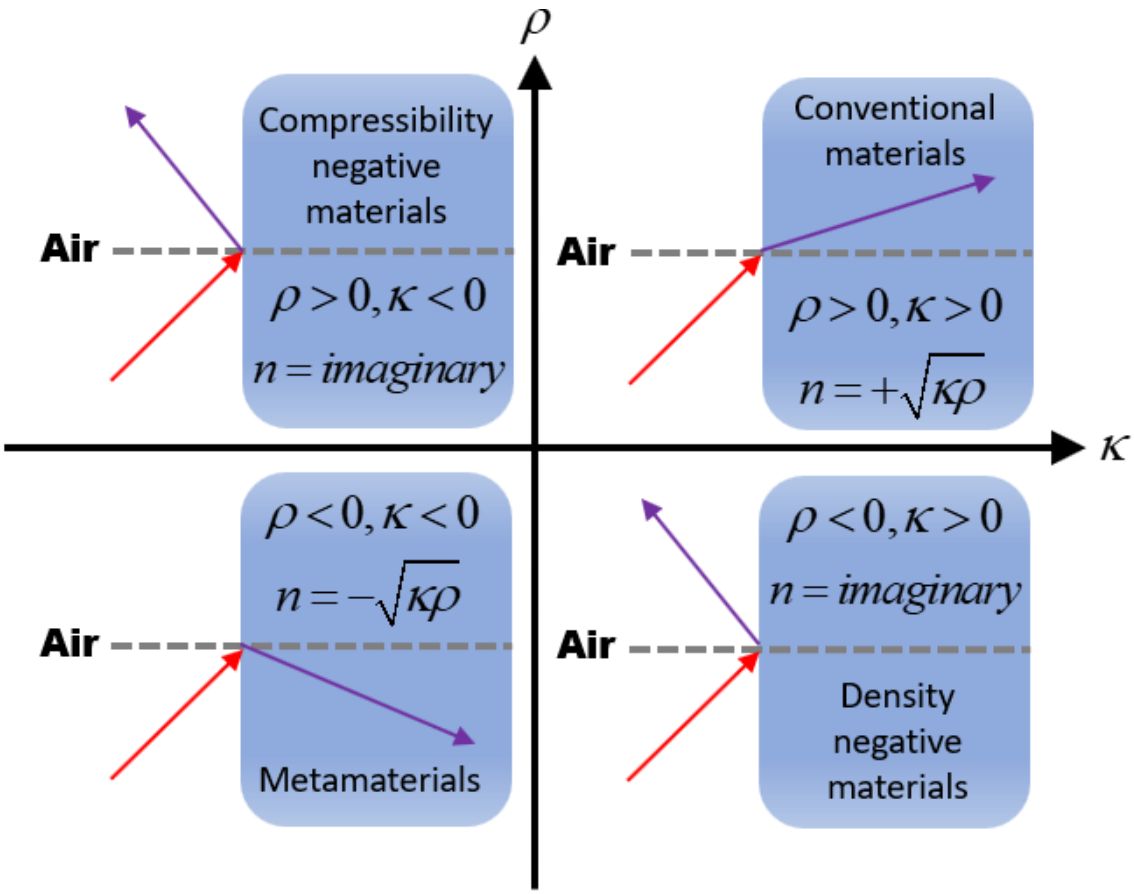

Figure 1.1. Acoustic wave behavior in metamaterials as functions of density and bulk module.

When both material compressibility and density are positive, the refraction index is also positive. When a beam of sound wave incident from air to this medium, the incident beam and the refracted beam will lie on both sides of the normal line. When one of compressibility and density is negative while the other keeps positive, given by the square root in the expression of sound speed, the sound speed is imaginary, and hence, sound waves cannot travel inside this media. When both compressibility and density are

negative, the refraction index becomes negative, resulting in the negative refraction. In this case, for a sound beam coming from air into this media, the incident beam and the refracted beam will lie on the same side of the normal line.

Extending materials properties from both positive region to single negative and/or both negative regions has greatly enriched our abilities in the manipulation of acoustic waves. In acoustics, typically volume compression is only a function of the applied pressure, and the unit mass momentum is solely dependent on the applied velocity. All the metamaterials obey Equations (1.1) and (1.2), summarized in Fig. 1.1, are classified as local metamaterials, which means that the response at any point in space is related to the excitation at that point. However, there are still so many things that local metamaterials cannot achieve in acoustic. Extending the exploration of acoustic metamaterials into the nonlocal region will greatly enhance our ability in the control and manipulation of acoustic waves. A simple example of nonlocal phenomena in acoustic is the Willis coupling, also known as acoustic bianisotropy, by relating volume compression and unit mass momentum to both applied pressure and velocity [56]. However, the nonlocal effect in acoustic is typically very small and is negligible in most of the scenarios. And hence the previous exploration of acoustic metamaterials often neglects the effect of nonlocality. In my study, I found that the nonlocal phenomena in acoustics could actually be engineered to be very strong, and could greatly enrich our ability in the control of acoustic waves and realize acoustic metamaterials which were considered impossible previously, which results in this dissertation.

1.3 Dissertation Outline

This dissertation studies and analyzes nonlocal phenomena in acoustics in different aspects, from a single scatterer, to bulk metamaterials and metasurfaces. The main purpose of this dissertation is to provide comprehensive research and understanding of how nonlocal phenomena could extend our ability in the manipulation of sound waves. Although the nonlocal phenomena were considered to be small in most cases and are neglected in most of the study, in this dissertation, I will show through specific engineering and optimization, the nonlocal phenomena could be greatly enhanced and achieving several amazing and unusual properties. This dissertation partially contains the results of my publications in [57]-[61].

In Chapter 2, this dissertation starts with discussing nonlocal phenomena in a single acoustic scatterer. In the subwavelength scale, monopole radiation and dipole radiation dominants the scattering properties of a scatterer. I first study the scattering properties of the reciprocal scatterer and provide the constraints on the polarizability tensor. Based on the energy conservation law, I derived a general bound of the Willis coupling, indicating that the Willis response could actually be as strong at the direct polarizability effect. Through analyzing the basic physical mechanism, acoustic scatterers with different levels of Willis response are designed and analyzed. Research indicates the realization of reciprocal Willis scatterer is based on breaking the system's spatial inversion symmetry, i.e. design asymmetrical scatterers. The application of Willis scatterers in the unitary acoustic meta-grating has also been discussed. The research then

has been extended to the study of non-reciprocal inclusion. My results indicate breaking reciprocal cannot increase Willis response, and in the non-reciprocal inclusion, the maximum Willis coupling is identical to the reciprocal case. Research also indicates breaking the system's spatial inversion symmetry is a sufficient condition but not the necessary condition to achieve Willis response. Through breaking the system's time-reversal symmetry with bias flow, I observed Willis response in a geometry symmetrical scatterer. And such inclusion was also utilized in the design of non-reciprocal meta-grating.

In Chapter 3, I changed the viewpoint from a single inclusion to bulk metamaterials. The relation between Willis coupling and non-reciprocal metamaterials has been clarified. We first discussed the realization of giant non-reciprocity and bianisotropy by modest mechanical motion. Combing resonant metamaterials with bias flow, the wavenumber contains two portions, the reciprocal portion, and the non-reciprocal portion. Operating the system in the zero-index region, i.e. letting the reciprocal portion to be zero, only the non-reciprocal portion will exist in the wavenumber, resulting in the positive-to-negative sound refraction. Specifically, when the wave coming from one direction the medium is with a positive index, but the medium will achieve a negative index when the wave coming from the opposite direction. Through specific modulation of mechanical motion in different channels, I also realized a non-reciprocal lens that could focus object when the excitation is from one side but not on the opposite side. The modulation of bias flow has then been extended into a lattice system, acoustic cyclotron and topological effect have been achieved, respectively.

In Chapter 4, I extended the study of nonlocal phenomena to metasurfaces. By considering the coupling effect between neighboring elements, a new impedance constitutive relation was proposed. The nonlocal metasurface was first applied to beam steering metasurface design, which could overcome the limitation of local design, and achieve unitary efficiency with the use of only passive units. The proposed nonlocal metasurface has also been applied to acoustic hyperbolic metasurface design. In acoustic, due to the longitudinal basics of sound propagation in fluids, the surface impedance must be isotropic, and hence the acoustic hyperbolic metasurface wave considered impossible in the traditional view. Introducing nonlocality into metasurface design and engineering strong coupling between neighboring impedance elements could enable extreme anisotropic responses of surface impedance, support not only hyperbolic transportation of sound waves but also negative phase and energy velocities.

In Chapter 5, a summary and conclusion of the dissertation are provided.

CHAPTER 2: NONLOCAL RESPONSE OF A SINGLE SCATTER

2.1 Research Background

Metamaterials and metasurfaces have enabled exciting opportunities in the manipulation of both electromagnetic waves [62]-[66] and provided a great platform for giant light-matter interactions. These fascinating developments have stimulated efforts in making analogies between different wave engineering fields, resulting in the concepts being rapidly extended into acoustic. Acoustic metamaterials have enabled unprecedented sound-matter interaction with different applications such as acoustic collimators, nonlinear acoustic metamaterials, and cloaks of inaudibility [48]-[51],[67]-[70]. There are various subwavelength resonant and non-resonant inclusions to realize these artificial acoustic metamaterials, such as membrane-type inclusions [71][72], Helmholtz resonators [73], and space-coiling structures [74][75], which will provide the required and enhanced dipole and/or monopole responses.

In electromagnetics, magnetoelectric coupling, or also known as bianisotropy, has provided an additional knob in tailoring the wave-matter response by coupling of magnetic and electric phenomena at the subwavelength scale. A direct analogy in elastodynamics proposed by Dr. Willis in the 1980s [56] has attracted great attention recently in the exploration of acoustic metamaterials [76]-[81]. Specifically, Willis coupling describes the coupling between pressure and velocity, and the effect was found to be small in many realizations [77]-[81]. In order to explore the full extent bianisotropy

in elastodynamics and acoustics, realizing inclusions with giant Willis coupling is important and urgent.

2.2 Constraints on Willis Coupling

Consider a subwavelength inclusion located in a fluid background and induced by an incident acoustic wave. Since the particle is in the subwavelength scale, the monopole mode and the dipole mode dominate the scattering field. For traditional non-bianisotropic linear inclusion, the monopole is proportional to the excited pressure field and the dipole is proportional to the excited velocity field. For Willis scatterers, however, monopole and dipole could be excited by both pressure and velocity fields, and the general relation could be written as

$$\begin{pmatrix} M \\ \mathbf{D} \end{pmatrix} = \overleftrightarrow{\boldsymbol{\alpha}} \begin{pmatrix} p \\ \mathbf{v} \end{pmatrix} = \begin{pmatrix} \alpha^{pp} & \overleftrightarrow{\boldsymbol{\alpha}}^{pv} \\ \overleftrightarrow{\boldsymbol{\alpha}}^{vp} & \overleftrightarrow{\boldsymbol{\alpha}}^{vv} \end{pmatrix} \begin{pmatrix} p \\ \mathbf{v} \end{pmatrix} \tag{2.1}$$

Here $M = \int_V \rho dV$ is the acoustic monopole, and $\mathbf{D} = \int_V \rho \mathbf{r} dV$ is the acoustic dipole moment. p indicates the local pressure, $\mathbf{v}$ indicates the local velocity, $\overleftrightarrow{\boldsymbol{\alpha}}$ is the polarizability tensor and ρ is the density distribution of the inclusion. The diagonal terms α^{pp} and $\overleftrightarrow{\boldsymbol{\alpha}}^{vv}$ are the direct polarizabilities, while the off-diagonal terms $\overleftrightarrow{\boldsymbol{\alpha}}^{pv}$ and $\overleftrightarrow{\boldsymbol{\alpha}}^{vp}$ are the cross-coupling terms, indicating Willis response of the scatterers.

2.2.1 CONSTRAINTS ON ENERGY CONSERVATION IN 2D

For simplicity but without loss of generality, we first consider the Willis response in two-dimensional (2D) scenario, and hence the polarizabilities expressed in (2.1) would be simplified as

$$\begin{pmatrix} M \\ D_x \\ D_y \end{pmatrix} = \begin{pmatrix} \alpha^{pp} & \alpha_x^{pv} & \alpha_y^{pv} \\ \alpha_x^{vp} & \alpha_{xx}^{vv} & \alpha_{xy}^{vv} \\ \alpha_y^{vp} & \alpha_{yx}^{vv} & \alpha_{yy}^{vv} \end{pmatrix} \begin{pmatrix} p \\ v_x \\ v_y \end{pmatrix} \tag{2.2}$$

For an acoustic subwavelength scatterer, the scattered pressure field of a monopole can be expressed as

$$p_{Ms} = -ik_0^2 \frac{Mc_0^2}{4} H_0^{(1)}(k_0 r) e^{-i\omega t} \tag{2.3}$$

Here $H_0^{(1)}(k_0 r)$ is the zeroth-order Hankel function to the first kind. By taking the asymptotic form of Hankel function, we can get the far-field scattered pressure as

$$p_{Ms} = k_0^2 \frac{Mc_0^2}{4} \sqrt{\frac{2}{\pi k_0 r}} e^{ik_0 r} e^{-i\frac{3\pi}{4}} e^{-i\omega t} \tag{2.4}$$

And hence we could also get the far-field scattered velocity field in the radial direction as

$$v_{r,Ms} = k_0^3 \frac{Mc_0^2}{4\omega\rho_0} e^{-i\frac{3\pi}{4}} e^{-i\omega t} \sqrt{\frac{2}{\pi k_0 r}} e^{ik_0 r} \tag{2.5}$$

The Poynting vector in the radial direction for the acoustic monopole reads

$$\mathbf{I}_{Ms} = \hat{r} \frac{1}{2} p_{Ms}^* v_{r,Ms} = \frac{c_0^3}{16\pi r \rho_0} k_0^3 |M|^2 \tag{2.6}$$

And hence the total radiation power for the acoustic monopole is

$$P_{Ms} = \int_S \mathbf{I}_{Ms} \cdot d\mathbf{A} = \frac{c_0^3}{8\rho_0} k_0^3 \left|M\right|^2 \tag{2.7}$$

Similarly, for the case of an acoustic dipole, the scattered pressure field could be expressed as

$$p_{Ds} = -i\frac{k_0^3 c_0^2}{4}\left(D_x \cos\theta + D_y \sin\theta\right) H_1^{(1)}\left(k_0 r\right) e^{-i\omega t} \tag{2.8}$$

And by taking the asymptotic forms of the Hankel function, we could get the far-field scattered pressure as

$$p_{Ds} = \frac{k_0^3 c_0^2}{4}\left(D_x \cos\theta + D_y \sin\theta\right) e^{-i\omega t} \sqrt{\frac{2}{\pi k_0 r}} e^{ik_0 r} e^{i\frac{3\pi}{4}} \tag{2.9}$$

In the far-field, the radial component of the scattered velocity field from a dipole could be expressed as

$$v_{r,Ds} = \frac{k_0^3 c_0}{4\rho_0}\left(D_x \cos\theta + D_y \sin\theta\right) e^{-i\omega t} \sqrt{\frac{2}{\pi k_0 r}} e^{ik_0 r} e^{i\frac{3\pi}{4}} \tag{2.10}$$

And hence, the Poynting vector in the radial direction could be written as

$$\mathbf{I}_{Ds} = \hat{r}\frac{1}{2} p_{Ds}^* v_{r,Ds} = \frac{\left(D_x^* \cos\theta + D_y^* \sin\theta\right)\left(D_x \cos\theta + D_y \sin\theta\right)}{16\pi r \rho_0} c_0^3 k_0^5 \tag{2.11}$$

So the corresponding radiated power could be written as

$$P_{Ds} = \int_S \mathbf{I}_{Ds} \cdot d\mathbf{A} = c_0^3 k_0^5 \frac{\left|D_x\right|^2 + \left|D_y\right|^2}{16\rho_0} = c_0^3 k_0^3 \frac{\left|ik_0 D_x\right|^2 + \left|ik_0 D_y\right|^2}{16\rho_0} \tag{2.12}$$

Based on Eqs. (2.7) and (2.12), the total scattered power can be expressed as

$$\int_S p_s \mathbf{v}_s \cdot d\mathbf{A} = P_{Ms} + P_{Ds} = \frac{c_0^3 k_0^3}{16\rho_0}\left(2\left|M\right|^2 + \left|ik_0 D_x\right|^2 + \left|ik_0 D_y\right|^2\right) \tag{2.13}$$

The extinction power of an acoustic scatterer can be written as

$$P_{ext} = -\int_S \left(p_s \mathbf{v}_i + p_i \mathbf{v}_s \right) \cdot d\mathbf{A} \tag{2.14}$$

For a subwavelength scatterer, we could also rewrite the expression of extinction power related to dipole source and monopole source as

$$P_{ext} = -\mathbf{v}_i \cdot \frac{\partial^2 \mathbf{D}}{\partial t^2} - \frac{p_i}{\rho_0} \frac{\partial M}{\partial t} \tag{2.15}$$

In the frequency domain, the extinction power can be written as

$$P_{ext} = \frac{\omega^2}{2} \mathrm{Re}\left(\mathbf{v}_i^* \cdot \mathbf{D} \right) - \frac{\omega}{2\rho_0} \mathrm{Im}\left(p_i^* M \right) = \frac{\omega}{2\rho_0} \mathrm{Im}\left(\rho_0 c_0 \mathbf{v}_i^* \cdot i k_0 \mathbf{D} - p_i^* M \right) \tag{2.16}$$

The conservation of energy requires that for passive scatterers, the scattered power to be not greater than the extinction power

$$\int_S p_s \mathbf{v}^*{}_s \cdot d\mathbf{A} \le -\int_S \left(p_s \mathbf{v}^*{}_i + p_i \mathbf{v}^*{}_s \right) \cdot d\mathbf{A} \tag{2.17}$$

resulting in

$$\omega^2 \left(\left| \sqrt{2} M \right|^2 + \left| i k_0 D_x \right|^2 + \left| i k_0 D_y \right|^2 \right) \le 8 \,\mathrm{Im}\left(\rho_0 c_0 \mathbf{v}_i^* \cdot i k_0 \mathbf{D} - \frac{p_i^*}{\sqrt{2}} \sqrt{2} M \right) \tag{2.18}$$

The left side of the equation indicated the scattered power by acoustic monopole and dipole while the right side represents the extinction power.

We could write the constitutive relation in Eq. (2.2) in a normalized form as

$$\begin{pmatrix} -\sqrt{2} M \\ i k_0 D_x \\ i k_0 D_y \end{pmatrix} = \begin{pmatrix} -2\alpha^{pp} & -\sqrt{2}\alpha_x^{pv} / \rho_0 c_0 & -\sqrt{2}\alpha_y^{pv} / \rho_0 c_0 \\ i k_0 \sqrt{2} \alpha_x^{vp} & i k_0 \alpha_{xx}^{vv} / \rho_0 c_0 & i k_0 \alpha_{xy}^{vv} / \rho_0 c_0 \\ i k_0 \sqrt{2} \alpha_y^{vp} & i k_0 \alpha_{yx}^{vv} / \rho_0 c_0 & i k_0 \alpha_{yy}^{vv} / \rho_0 c_0 \end{pmatrix} \begin{pmatrix} p_i / \sqrt{2} \\ \rho_0 c_0 v_{ix} \\ \rho_0 c_0 v_{iy} \end{pmatrix} \tag{2.19}$$

And now we get the normalized polarizability tensor with all components having the same dimension

$$\ddot{\boldsymbol{\alpha}}' = \begin{pmatrix} -2\alpha^{pp} & -\sqrt{2}\alpha_x^{pv}/\rho_0 c_0 & -\sqrt{2}\alpha_y^{pv}/\rho_0 c_0 \\ ik_0\sqrt{2}\alpha_x^{vp} & ik_0\alpha_{xx}^{vv}/\rho_0 c_0 & ik_0\alpha_{xy}^{vv}/\rho_0 c_0 \\ ik_0\sqrt{2}\alpha_y^{vp} & ik_0\alpha_{yx}^{vv}/\rho_0 c_0 & ik_0\alpha_{yy}^{vv}/\rho_0 c_0 \end{pmatrix} \tag{2.20}$$

The left side of Eq. (2.18) would be rewritten to be

$$\begin{aligned} &\omega^2\left(\left|\sqrt{2}M\right|^2 + \left|ik_0 D_x\right|^2 + \left|ik_0 D_y\right|^2\right) \\ &\qquad = \omega^2 \begin{pmatrix} -\sqrt{2}M^* & \left(ik_0 D_x\right)^* & \left(ik_0 D_y\right)^* \end{pmatrix} \begin{pmatrix} -\sqrt{2}M \\ ik_0 D_x \\ ik_0 D_y \end{pmatrix} \end{aligned} \tag{2.21}$$

Substitute Eq. (2.19) into Eq. (2.21), we have

$$\omega^2\left(\left|\sqrt{2}M\right|^2 + \left|ik_0 D_x\right|^2 + \left|ik_0 D_y\right|^2\right) = \omega^2 \begin{pmatrix} p_i/\sqrt{2} & \rho_0 c_0 v_{ix} & \rho_0 c_0 v_{iy} \end{pmatrix}^* \ddot{\boldsymbol{\alpha}}'^{*T} \ddot{\boldsymbol{\alpha}}' \begin{pmatrix} p_i/\sqrt{2} \\ \rho_0 c_0 v_{ix} \\ \rho_0 c_0 v_{iy} \end{pmatrix} \tag{2.22}$$

Using $\mathrm{Im}() = \frac{1}{2i}\left[() - ()^*\right]$, the right side of Eq. (2.18) can be simplified to

$$\begin{aligned} &8\,\mathrm{Im}\left(\rho_0 c_0 \mathbf{v}_i^* \cdot ik_0 \mathbf{D} - \frac{p_i^*}{\sqrt{2}}\sqrt{2}M\right) \\ &\qquad = -4i\left[\begin{pmatrix} \frac{p_i^*}{\sqrt{2}} & \rho_0 c_0 v_{ix}^* & \rho_0 c_0 v_{iy}^* \end{pmatrix}\left(\ddot{\boldsymbol{\alpha}}' - \ddot{\boldsymbol{\alpha}}'^{T*}\right)\begin{pmatrix} p_i/\sqrt{2} \\ \rho_0 c_0 v_{ix} \\ \rho_0 c_0 v_{iy} \end{pmatrix}\right] \end{aligned} \tag{2.23}$$

Combing Eqs. (2.18), (2.22) and (2.23), we have

$$\omega^2 \begin{pmatrix} p_i/\sqrt{2} & \rho_0 c_0 v_{ix} & \rho_0 c_0 v_{iy} \end{pmatrix}^* \ddot{\boldsymbol{\alpha}}'^{*T} \ddot{\boldsymbol{\alpha}}' \begin{pmatrix} p_i/\sqrt{2} \\ \rho_0 c_0 v_{ix} \\ \rho_0 c_0 v_{iy} \end{pmatrix} \leq -4i \left[\begin{pmatrix} \dfrac{p_i^*}{\sqrt{2}} & \rho_0 c_0 v_{ix}^* & \rho_0 c_0 v_{yi}^* \end{pmatrix} \left(\ddot{\boldsymbol{\alpha}}' - \ddot{\boldsymbol{\alpha}}'^{T*} \right) \begin{pmatrix} p_i/\sqrt{2} \\ \rho_0 c_0 v_{ix} \\ \rho_0 c_0 v_{iy} \end{pmatrix} \right] \tag{2.24}$$

Here $(.)^T$ and $(.)^*$ indicate the transpose operator and complex conjugate, respectively. And the condition could be written in a more compact way as

$$\mathrm{Diag}\left[\omega^2 \left(\ddot{\boldsymbol{\alpha}}'^{*T} \ddot{\boldsymbol{\alpha}}' \right) \right] \leq \mathrm{Diag}\left[4i \left(\ddot{\boldsymbol{\alpha}}'^{T*} - \ddot{\boldsymbol{\alpha}}' \right) \right] \tag{2.25}$$

2.2.2 CONSTRAINTS ON RECIPROCITY

In this section, we present the detailed derivation of the conditions imposed by reciprocity on the polarizabilities of an acoustic scatterer. The study in electrodynamics could be found in [82]. For a subwavelength scatterer, the scattered pressure and velocity fields are dominant by a set of monopole and dipole and could be expressed through Green function

$$\begin{pmatrix} p_s(\mathbf{r})/\sqrt{2} \\ \rho_0 c_0 v_{sx}(\mathbf{r}) \\ \rho_0 c_0 v_{sy}(\mathbf{r}) \end{pmatrix} = \ddot{\mathbf{G}}(\mathbf{r}, \mathbf{r}') \begin{pmatrix} -\sqrt{2} M(\mathbf{r}') \\ ik_0 D_x(\mathbf{r}') \\ ik_0 D_y(\mathbf{r}') \end{pmatrix} \tag{2.26}$$

Here $\ddot{\mathbf{G}}(\mathbf{r}, \mathbf{r}')$ is the green function tensor which is defined as [83].

$$\begin{aligned}\overleftrightarrow{\mathbf{G}}(\mathbf{r},\mathbf{r}') &= \begin{pmatrix} G^{pp}(\mathbf{r},\mathbf{r}') & \overleftrightarrow{\mathbf{G}}^{pv}(\mathbf{r},\mathbf{r}') \\ \overleftrightarrow{\mathbf{G}}^{vp}(\mathbf{r},\mathbf{r}') & \overleftrightarrow{\mathbf{G}}^{vv}(\mathbf{r},\mathbf{r}') \end{pmatrix} \\ &= \begin{pmatrix} \dfrac{k_0^2 c_0^2}{2} G(\mathbf{r},\mathbf{r}') & -\dfrac{ik_0 c_0^2}{\sqrt{2}} \dfrac{\partial G(\mathbf{r},\mathbf{r}')}{\partial x} & -\dfrac{ik_0 c_0^2}{\sqrt{2}} \dfrac{\partial G(\mathbf{r},\mathbf{r}')}{\partial y} \\ -\dfrac{ik_0 c_0^2}{\sqrt{2}} \dfrac{\partial G(\mathbf{r},\mathbf{r}')}{\partial x} & -c_0^2 \dfrac{\partial^2 G(\mathbf{r},\mathbf{r}')}{\partial x^2} & -c_0^2 \dfrac{\partial^2 G(\mathbf{r},\mathbf{r}')}{\partial x \partial y} \\ -\dfrac{ik_0 c_0^2}{\sqrt{2}} \dfrac{\partial G(\mathbf{r},\mathbf{r}')}{\partial y} & -c_0^2 \dfrac{\partial^2 G(\mathbf{r},\mathbf{r}')}{\partial x \partial y} & -c_0^2 \dfrac{\partial^2 G(\mathbf{r},\mathbf{r}')}{\partial y^2} \end{pmatrix} \end{aligned} \tag{2.27}$$

Here $G(\mathbf{r},\mathbf{r}') = \dfrac{i}{4} H_0^{(1)}(k_0 r)$ is the Green function in the free space of a point source in the origin. Reciprocity principle requires the Green function to satisfy

$$\begin{pmatrix} G^{pp}(\mathbf{r},\mathbf{r}') & \overleftrightarrow{\mathbf{G}}^{pv}(\mathbf{r},\mathbf{r}') \\ \overleftrightarrow{\mathbf{G}}^{vp}(\mathbf{r},\mathbf{r}') & \overleftrightarrow{\mathbf{G}}^{vv}(\mathbf{r},\mathbf{r}') \end{pmatrix} = \begin{pmatrix} G^{pp}(\mathbf{r}',\mathbf{r}) & -\overleftrightarrow{\mathbf{G}}^{pv}(\mathbf{r}',\mathbf{r}) \\ -\overleftrightarrow{\mathbf{G}}^{vp}(\mathbf{r}',\mathbf{r}) & \overleftrightarrow{\mathbf{G}}^{vv}(\mathbf{r}',\mathbf{r}) \end{pmatrix}^{T} \tag{2.28}$$

If we use the operator $T-$ to take the transpose and then reverse signs of off-diagonal blocks, the equation can be simplified to

$$\overleftrightarrow{\mathbf{G}}(\mathbf{r},\mathbf{r}') = \left[\overleftrightarrow{\mathbf{G}}(\mathbf{r}',\mathbf{r})\right]^{T-} \tag{2.29}$$

for a scatterer located at $\mathbf{r}_s$, a source located at $\mathbf{r}_1$, and the observation point at $\mathbf{r}_2$ we have

$$\begin{pmatrix} p_s(\mathbf{r}_2)/\sqrt{2} \\ \rho_0 c_0 v_{sx}(\mathbf{r}_2) \\ \rho_0 c_0 v_{sy}(\mathbf{r}_2) \end{pmatrix} = \overleftrightarrow{\mathbf{G}}(\mathbf{r}_2,\mathbf{r}_1) \begin{pmatrix} -\sqrt{2} M(\mathbf{r}_1) \\ ik_0 D_x(\mathbf{r}_1) \\ ik_0 D_y(\mathbf{r}_1) \end{pmatrix} \tag{2.30}$$

The field at $\mathbf{r}_2$ can also be expressed using free-space Green function $\overleftrightarrow{\mathbf{G}}_0$ tensor:

$$\begin{pmatrix} p_s(\mathbf{r}_2)/\sqrt{2} \\ \rho_0 c_0 v_{sx}(\mathbf{r}_2) \\ \rho_0 c_0 v_{sy}(\mathbf{r}_2) \end{pmatrix} = \ddot{\mathbf{G}}^0(\mathbf{r}_2,\mathbf{r}_1) \begin{pmatrix} -\sqrt{2}M(\mathbf{r}_1) \\ ik_0 D_x(\mathbf{r}_1) \\ ik_0 D_y(\mathbf{r}_1) \end{pmatrix} + \ddot{\mathbf{G}}^0(\mathbf{r}_2,\mathbf{r}_s)\ddot{\boldsymbol{\alpha}}'\ddot{\mathbf{G}}^0(\mathbf{r}_s,\mathbf{r}_1) \begin{pmatrix} -\sqrt{2}M(\mathbf{r}_1) \\ ik_0 D_x(\mathbf{r}_1) \\ ik_0 D_y(\mathbf{r}_1) \end{pmatrix} \quad (2.31)$$

Comparing Eqs. (2.30) and (2.31), we have

$$\ddot{\mathbf{G}}(\mathbf{r}_1,\mathbf{r}_2) = \ddot{\mathbf{G}}^0(\mathbf{r}_1,\mathbf{r}_2) + \ddot{\mathbf{G}}^0(\mathbf{r}_1,\mathbf{r}_s)\ddot{\boldsymbol{\alpha}}'\ddot{\mathbf{G}}^0(\mathbf{r}_s,\mathbf{r}_2) \quad (2.32)$$

Apply the operator $T-$, we get

$$\left[\ddot{\mathbf{G}}(\mathbf{r}_2,\mathbf{r}_1)\right]^{T-} = \left[\ddot{\mathbf{G}}^0(\mathbf{r}_2,\mathbf{r}_1)\right]^{T-} + \left[\ddot{\mathbf{G}}^0(\mathbf{r}_s,\mathbf{r}_1)\right]^{T-} \ddot{\boldsymbol{\alpha}}'^{T-} \left[\ddot{\mathbf{G}}^0(\mathbf{r}_2,\mathbf{r}_s)\right]^{T-} \quad (2.33)$$

According to the reciprocity relation shown in Eq. (2.29), the Onsager relation for acoustic dynamic polarizability could be written as

$$\ddot{\boldsymbol{\alpha}}' = \ddot{\boldsymbol{\alpha}}'^{T-} \quad (2.34)$$

In the 2D version, the Onsager relation can be written as

$$\alpha_{xy}^{vv} = \alpha_{yx}^{vv},\ \alpha_x^{pv} = ik_0\rho_0 c_0 \alpha_x^{vp},\ \text{and}\ \alpha_y^{pv} = ik_0\rho_0 c_0 \alpha_y^{vp} \quad (2.35)$$

2.2.3 BOUND OF WILLIS COUPLING IN 2D

In the non-bianisotropic limit, the off-diagonal terms in Eq. (2.20) are zero, and the reciprocity condition is always satisfied. So the energy conservation in Eq. (2.25) requires

$$\mathrm{Im}\left(1/\alpha^{pp'}\right) \le -\omega^2/8 \text{ and } \mathrm{Im}\left(1/\alpha_{xx}^{vv'}\right) = \mathrm{Im}\left(1/\alpha_{yy}^{vv'}\right) \le -\omega^2/8 \quad (2.36)$$

Here the constraints on the imaginary part of the direct polarizability terms reflect the radiation loss of the scatterers, and the inequalities become equalities when the particle is

passive but lossless. In the general situation with non-zero bianisotropy, by substitute full polarizability tensor into Eq. (2.25), we could derive the bound of Willis response

$$\begin{cases} \sqrt{\left|\alpha_x^{vp\prime}\right|^2+\left|\alpha_y^{vp\prime}\right|^2} \le \sqrt{\dfrac{-\dfrac{8}{\omega^2}\mathrm{Im}\left(1/\alpha^{pp\prime}\right)-1}{\left|1/\alpha^{pp\prime}\right|^2}} \le \dfrac{4}{\omega^2} \\ \sqrt{\left|\alpha_x^{vp\prime}\right|^2+\left|\alpha_{xy}^{vv\prime}\right|^2} \le \sqrt{\dfrac{-\dfrac{8}{\omega^2}\mathrm{Im}\left(1/\alpha_{xx}^{vv\prime}\right)-1}{\left|1/\alpha_{xx}^{vv\prime}\right|^2}} \le \dfrac{4}{\omega^2} \\ \sqrt{\left|\alpha_y^{vp\prime}\right|^2+\left|\alpha_{xy}^{vv\prime}\right|^2} \le \sqrt{\dfrac{-\dfrac{8}{\omega^2}\mathrm{Im}\left(1/\alpha_{yy}^{vv\prime}\right)-1}{\left|1/\alpha_{yy}^{vv\prime}\right|^2}} \le \dfrac{4}{\omega^2} \end{cases} \tag{2.37}$$

Since $\left|\alpha_x^{vp\prime}\right|$ and $\left|\alpha_y^{vp\prime}\right|$ cannot be negative, the first condition in Eq. (2.37) could interpret the condition shown in Eq. (2.36), indicating it is general and suitable for both bianisotropy and non-bianisotropy cases.

Now if we simplify our model and assume that the particle is only resonant in the *y*-direction, i.e. $\left|\alpha_y^{vp\prime}\right| >> \left|\alpha_x^{vp\prime}\right|$, the renormalized polarizability tensor could be simplified as

$$\ddot{\boldsymbol{\alpha}}' = \begin{pmatrix} \alpha^{pp\prime} & 0 & \alpha_y^{pv\prime} \\ 0 & 0 & 0 \\ \alpha_y^{vp\prime} & 0 & \alpha_{yy}^{vv\prime} \end{pmatrix} \tag{2.38}$$

In this case, the bound of Willis coupling could be simplified as $\left|\alpha_y^{vp\prime}\right| \le 4\omega^{-2}$. From Eq. (2.37), we could find the maximum bound of Willis coupling can be reached only when

the particle is at resonance for both monopole and dipole, and having $1/\alpha_{yy}^{vv'} = -i\omega^2/4$ and $1/\alpha^{pp'} = -i\omega^2/4$ are purely imaginary. Substituting these conditions back to the polarizability tensor, we could get the polarizability tensor of an optimized inclusion reaching maximum Willis response satisfies

$$\begin{pmatrix} \left|\alpha_{pp}{}'\right| & \left|\alpha_x^{pv'}\right| & \left|\alpha_y^{pv'}\right| \\ \left|\alpha_x^{vp'}\right| & \left|\alpha_{xx}^{vv'}\right| & \left|\alpha_{xy}^{vv'}\right| \\ \left|\alpha_y^{vp'}\right| & \left|\alpha_{yx}^{vv'}\right| & \left|\alpha_{yy}^{vv'}\right| \end{pmatrix} = \frac{4}{\omega^2}\begin{pmatrix} 1 & 0 & 1 \\ 0 & 0 & 0 \\ 1 & 0 & 1 \end{pmatrix} \tag{2.39}$$

These results indicate the maximum Willis coupling response of the off-diagonal terms can become of the same order as the diagonal terms of the polarizability tensor, providing new possibilities in the design of small scatterers and metamaterial inclusions.

From Eq. (2.37), we could get a general bound on the cross-coupling polarizability in another form

$$\sqrt{\frac{\left|\alpha_x^{vp'}\right|^2 + \left|\alpha_y^{vp'}\right|^2}{\left|\alpha^{pp'}\right|\sqrt{\left|\alpha_{xx}^{vv'}\right|^2 + \left|\alpha_{yy}^{vv'}\right|^2}}} \leq$$

$$\sqrt[4]{\left(-\frac{8}{\omega^2}\mathrm{Im}\left(1/\alpha^{pp'}\right)-1\right)\left[\frac{\left(-\frac{8}{\omega^2}\mathrm{Im}\left(1/\alpha_{xx}^{vv'}\right)-1\right)\left|\alpha_{xx}^{vv'}\right|^2 + \left(-\frac{8}{\omega^2}\mathrm{Im}\left(1/\alpha_{yy}^{vv'}\right)-1\right)\left|\alpha_{yy}^{vv'}\right|^2 - 2\left|\alpha_{xy}^{vv'}\right|^2}{\left|\alpha_{xx}^{vv'}\right|^2 + \left|\alpha_{yy}^{vv'}\right|^2}\right]} \tag{2.40}$$

If we suppose again the response is along the *y*-direction, and have $\alpha_x^{vp'} \approx 0$, $\alpha_{xx}^{vv'} \approx 0$ and $\alpha_{xy}^{vv'} \approx 0$, the condition could be simplified to

$$\frac{\left|\alpha_x^{vp'}\right|}{\sqrt{\left|\alpha^{pp'}\right|\left|\alpha_{yy}^{vv'}\right|}} \le \sqrt[4]{\left(-\frac{8}{\omega^2}\mathrm{Im}\left(1/\alpha^{pp'}\right)-1\right)\left(-\frac{8}{\omega^2}\mathrm{Im}\left(1/\alpha_{yy}^{vv'}\right)-1\right)} \tag{2.41}$$

This condition is general and works for all the frequency range. In general, there is no limit to the normalized Willis response compared to the direct response of the scatterer to pressure and velocity. However, when the Willis coupling reaches its maximum, i.e. $\left|\alpha_x^{vp'}\right| = 4\omega^{-2}$, we get

$$\left|\alpha_x^{vp'}\right| \le \sqrt{\left|\alpha^{pp'}\right|\left|\alpha_{yy}^{vv'}\right|} \tag{2.42}$$

As an excursus, there were also explorations of maximum bound of bianisotropy for small scatterers in electromagnetics. In Ref. [82][84][85], a similar bound consistent with Eq. (2.42) are derived under the assumption of a single coupled electromagnetic resonance in the scatterers. In Ref. [86], the study showed the cross-coupling effect can be greater than the direct polarizabilities when the particles are operating far from the resonance frequency. The general bound derived in Eq. (2.42), if extended to electromagnetics, could fully address this issue, and show that Eq. (2.41) is generally applied, except if we operate the scatterer near its resonance frequency, then the more stringent condition Eq. (2.42) holds.

2.2.4 CROSS-COUPLING BOUND FOR 3D

The radiation power for the acoustic monopole in 3D case could be expressed as

$$P_{Ms} = \int_S \mathbf{I}_{Ms} \cdot d\mathbf{A} = \frac{k_0^4 c_0^3}{8\pi\rho_0} |M|^2 \tag{2.43}$$

Also, the radiation power for acoustic dipole moment could be expressed as

$$P_{Ds} = \int_S \mathbf{I}_{Ds} \cdot d\mathbf{A} = \frac{k_0^6 c_0^3}{24\pi\rho_0} \left(|D_x|^2 + |D_y|^2 + |D_z|^2 \right) \tag{2.44}$$

Based on both Eqs. (2.43) and (2.44), the total scattered power can be written as

$$\iint p_s \mathbf{v}_s \cdot d\mathbf{A} = P_{Ms} + P_{Ds} = \frac{k_0^4 c_0^3}{24\pi\rho_0} \left(\left|\sqrt{3}M\right|^2 + \left|ik_0 D_x\right|^2 + \left|ik_0 D_y\right|^2 + \left|ik_0 D_z\right|^2 \right) \tag{2.45}$$

And the normalized polarizability tensor in 3D case is

$$\begin{pmatrix} -\sqrt{3}M \\ ik_0 D_x \\ ik_0 D_y \\ ik_0 D_z \end{pmatrix} = \begin{pmatrix} -3\alpha_{pp} & -\sqrt{3}\alpha_x^{pv}/\rho_0 c_0 & -\sqrt{3}\alpha_y^{pv}/\rho_0 c_0 & -\sqrt{3}\alpha_z^{pv}/\rho_0 c_0 \\ ik_0\sqrt{3}\alpha_x^{vp} & ik_0\alpha_{xx}^{vv}/\rho_0 c_0 & ik_0\alpha_{xy}^{vv}/\rho_0 c_0 & ik_0\alpha_{xz}^{vv}/\rho_0 c_0 \\ ik_0\sqrt{3}\alpha_y^{vp} & ik_0\alpha_{yx}^{vv}/\rho_0 c_0 & ik_0\alpha_{yy}^{vv}/\rho_0 c_0 & ik_0\alpha_{yz}^{vv}/\rho_0 c_0 \\ ik_0\sqrt{3}\alpha_z^{vp} & ik_0\alpha_{zx}^{vv}/\rho_0 c_0 & ik_0\alpha_{zy}^{vv}/\rho_0 c_0 & ik_0\alpha_{zz}^{vv}/\rho_0 c_0 \end{pmatrix} \begin{pmatrix} p/\sqrt{3} \\ \rho_0 c_0 v_x \\ \rho_0 c_0 v_y \\ \rho_0 c_0 v_z \end{pmatrix} \tag{2.46}$$

Following the same procedure as 2D case, we can get the energy conservation constraint in 3D

$$\mathrm{Diag}\left[k_0^3 c_0^2 \left(\ddot{\boldsymbol{\alpha}}'^{*T} \ddot{\boldsymbol{\alpha}}' \right) \right] \le \mathrm{Diag}\left[i6\pi \left(\ddot{\boldsymbol{\alpha}}'^{T^*} - \ddot{\boldsymbol{\alpha}}' \right) \right] \tag{2.47}$$

For non-bianisotropic inclusion, Eq. (2.47) requires

$$\mathrm{Im}\left(1/\alpha_{pp}'\right) \le -\frac{c_0^2 k_0^3}{12\pi} \text{ and } \mathrm{Im}\left(1/\alpha_{xx}^{vv\prime}\right) = \mathrm{Im}\left(1/\alpha_{yy}^{vv\prime}\right) \le -\frac{c_0^2 k_0^3}{12\pi} \tag{2.48}$$

For bianisitorpic scatterers, the general bound derived from Eq. (2.47) is

$$\begin{cases} \sqrt{\left|\alpha_x^{vp\prime}\right|^2+\left|\alpha_y^{vp\prime}\right|^2+\left|\alpha_z^{vp\prime}\right|^2} \le \sqrt{\dfrac{-\dfrac{12\pi}{c_0^2k_0^3}\mathrm{Im}\left(1/\alpha_{pp}{}'\right)-1}{\left|1/\alpha_{pp}{}'\right|^2}} \le \dfrac{6\pi}{c_0^2k_0^3} \\ \sqrt{\left|\alpha_x^{vp\prime}\right|^2+\left|\alpha_{xy}^{vv\prime}\right|^2+\left|\alpha_{xz}^{vv\prime}\right|^2} \le \sqrt{\dfrac{-\dfrac{12\pi}{c_0^2k_0^3}\mathrm{Im}\left(1/\alpha_{xx}^{vv\prime}\right)-1}{\left|1/\alpha_{xx}^{vv\prime}\right|^2}} \le \dfrac{6\pi}{c_0^2k_0^3} \\ \sqrt{\left|\alpha_y^{vp\prime}\right|^2+\left|\alpha_{xy}^{vv\prime}\right|^2+\left|\alpha_{yz}^{vv\prime}\right|^2} \le \sqrt{\dfrac{-\dfrac{12\pi}{c_0^2k_0^3}\mathrm{Im}\left(1/\alpha_{yy}^{vv\prime}\right)-1}{\left|1/\alpha_{yy}^{vv\prime}\right|^2}} \le \dfrac{6\pi}{c_0^2k_0^3} \\ \sqrt{\left|\alpha_z^{vp\prime}\right|^2+\left|\alpha_{xz}^{vv\prime}\right|^2+\left|\alpha_{yz}^{vv\prime}\right|^2} \le \sqrt{\dfrac{-\dfrac{12\pi}{c_0^2k_0^3}\mathrm{Im}\left(1/\alpha_{zz}^{vv\prime}\right)-1}{\left|1/\alpha_{zz}^{vv\prime}\right|^2}} \le \dfrac{6\pi}{c_0^2k_0^3} \end{cases} \tag{2.49}$$

2.3 Design of Reciprocal Willis Scatterer

2.3.1 POLARIZABILITY TENSOR RETRIEVAL

Here, I provide a basic polarizability retrieval method similar to the methods proposed in electromagnetics in Ref. [87][88]. We also focus our study in 2D. The acoustic pressure generated by monopole and dipole D_x and D_y can be expressed as

$$
\begin{aligned}
p_M &= -ik_0^2 \frac{M}{4\rho_0\kappa_0} H_0^{(1)}(k_0 r) \\
p_{Dx} &= -ik_0^3 \frac{D_x}{4\rho_0\kappa_0} H_1^{(1)}\left(k_0 r\right)\cos\theta \\
p_{Dy} &= -ik_0^3 \frac{D_y}{4\rho_0\kappa_0} H_1^{(1)}\left(k_0 r\right)\sin\theta
\end{aligned}
\tag{2.50}
$$

We can retrieve the monopole and dipole moments according to the orthogonality of each harmonics

$$
\begin{aligned}
M &= i\frac{2\rho_0\kappa_0}{\pi k_0^2 H_0^{(1)}(k_0 r)} \int_0^{2\pi} p d\theta \\
D_x &= i\frac{4\rho_0\kappa_0}{\pi k_0^3 H_1^{(1)}\left(k_0 r\right)} \int_0^{2\pi} p\cos\theta d\theta \\
D_y &= i\frac{4\rho_0\kappa_0}{\pi k_0^3 H_1^{(1)}\left(k_0 r\right)} \int_0^{2\pi} p\sin\theta d\theta
\end{aligned}
\tag{2.51}
$$

In the simulation, we excite the inclusion with four incident waves coming from *x*-direction, -*x*-direction, *y*-direction and -*y*-direction, respectively, and assuming that the incident pressure is 1 pa, then the velocity for *x*-direction and *y*-direction are $v^+ = \frac{1}{\rho_0 c_0}$ and the velocity for -*x*-direction and -*y*-direction are $v^- = -\frac{1}{\rho_0 c_0}$. Then we can get the expressions for monopole and dipole moments as

$$
\begin{aligned}
&{}^{+}_{x}M = \alpha^{pp} + \frac{\alpha_x^{pv}}{\rho_0 c_0},\ {}^{-}_{x}M = \alpha^{pp} - \frac{\alpha_x^{pv}}{\rho_0 c_0},\ {}^{+}_{y}M = \alpha^{pp} + \frac{\alpha_y^{pv}}{\rho_0 c_0},\ {}^{-}_{y}M = \alpha^{pp} - \frac{\alpha_y^{pv}}{\rho_0 c_0},\\
&{}^{+}_{x}D_x = \alpha_x^{vp} + \frac{\alpha_{xx}^{vv}}{\rho_0 c_0},\ {}^{-}_{x}D_x = \alpha_x^{vp} - \frac{\alpha_{xx}^{vv}}{\rho_0 c_0},\ {}^{+}_{y}D_x = \alpha_x^{vp} + \frac{\alpha_{xy}^{vv}}{\rho_0 c_0},\ {}^{-}_{y}D_x = \alpha_x^{vp} - \frac{\alpha_{xy}^{vv}}{\rho_0 c_0},\\
&{}^{+}_{x}D_y = \alpha_y^{vp} + \frac{\alpha_{yx}^{vv}}{\rho_0 c_0},\ {}^{-}_{x}D_y = \alpha_y^{vp} - \frac{\alpha_{yx}^{vv}}{\rho_0 c_0},\ {}^{+}_{y}D_y = \alpha_y^{vp} p + \frac{\alpha_{yy}^{vv}}{\rho_0 c_0},\ {}^{-}_{y}D_y = \alpha_y^{vp} p - \frac{\alpha_{yy}^{vv}}{\rho_0 c_0}
\end{aligned}
$$

(2.52)

Here ${}^{+}_{x}X$, ${}^{-}_{x}X$, ${}^{+}_{y}X$ and ${}^{-}_{y}X$ represent the harmonics for the incident waves coming from *x*-, *-x*-, *y*-, and *-y*-directions, respectively. From these equations, finally, we get the polarizability tensor as

$$
\begin{aligned}
&\alpha^{pp} = \frac{{}^{+}_{x}M + {}^{-}_{x}M + {}^{+}_{y}M + {}^{-}_{y}M}{4},\ \alpha_x^{pv} = \frac{{}^{+}_{x}M - {}^{-}_{x}M}{2}\rho_0 c_0,\ \alpha_y^{pv} = \frac{{}^{+}_{y}M - {}^{-}_{y}M}{2}\rho_0 c_0,\\
&\alpha_x^{vp} = \frac{{}^{+}_{x}D_x + {}^{-}_{x}D_x + {}^{+}_{y}D_x + {}^{-}_{y}D_x}{4},\ \alpha_{xx}^{vv} = \frac{{}^{+}_{x}D_x - {}^{-}_{x}D_x}{2}\rho_0 c_0,\ \alpha_{xy}^{vv} = \frac{{}^{+}_{y}D_x - {}^{-}_{y}D_x}{2}\rho_0 c_0,\\
&\alpha_y^{vp} = \frac{{}^{+}_{x}D_y + {}^{-}_{x}D_y + {}^{+}_{y}D_y + {}^{-}_{y}D_y}{4},\ \alpha_{yx}^{vv} = \frac{{}^{+}_{x}D_y - {}^{-}_{x}D_y}{2}\rho_0 c_0,\ \alpha_{yy}^{vv} = \frac{{}^{+}_{y}D_y - {}^{-}_{y}D_y}{2}\rho_0 c_0
\end{aligned}
$$

(2.53)

Through these equations, we could retrieve the polarizability tensor for an arbitrary acoustic scatterer. To confirm the effectiveness of our retrieve method, we study the polarizability tensor for a rigid cylinder with 5 cm in radius as shown in Fig. 2.1. We also compare these results with the theoretical results from Mie theory. According to Mie theory, the direct coupling coefficient are $\alpha^{pp} = i\frac{4\rho_0\kappa_0 A_0}{k_0^2}$ and $\alpha^{vv} = -\frac{8A_1\rho_0}{c_0 k_0^3}$, respectively, and the indirect cross-coupling coefficient is zero. Here A_0 and A_1 are Mie

scattering coefficients for monopole and dipole, respectively. In Fig. 2.1, we see that the FEM retrieval results are identical to Mie theory, which verifies the effectiveness of our approaches.

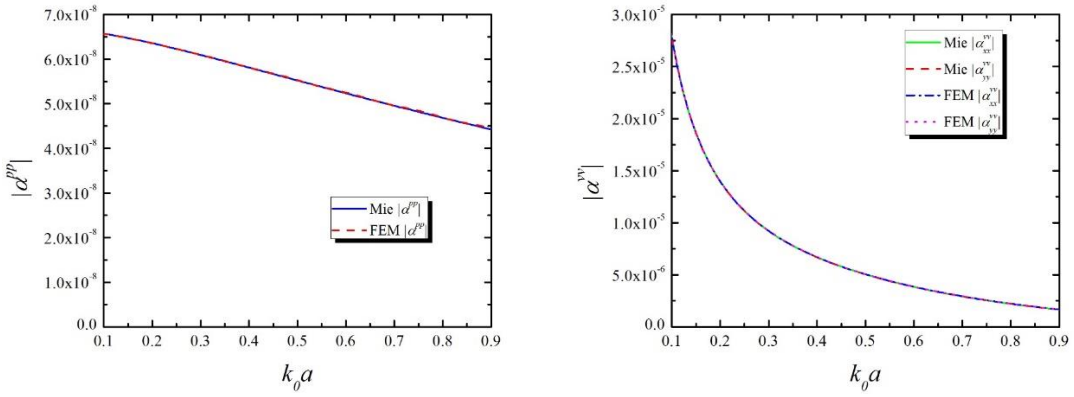

Figure 2.1. (a) and (b) Direct polarizability tensor of a rigid cylinder with radius 5 cm calculated by Mie theory and our numerical retrieval method.

2.3.2 PHYSICAL INTERPRETATION OF WILLIS COUPLING

The general bound shown in Eq. (2.39) indicates that the Willis coupling of a small scatterer could be as strong as the direct diagonal terms in the polarizability tensor. In order to explore the possibilities offered by the bianisotropic coupling and create giant sound-matter interactions, we have to design scatterers that approach the fundamental bound of the Willis coupling. In the following, we will show how we could systematically design particles with different levels of bianisotropic and through which way we could reach the maximum bound.

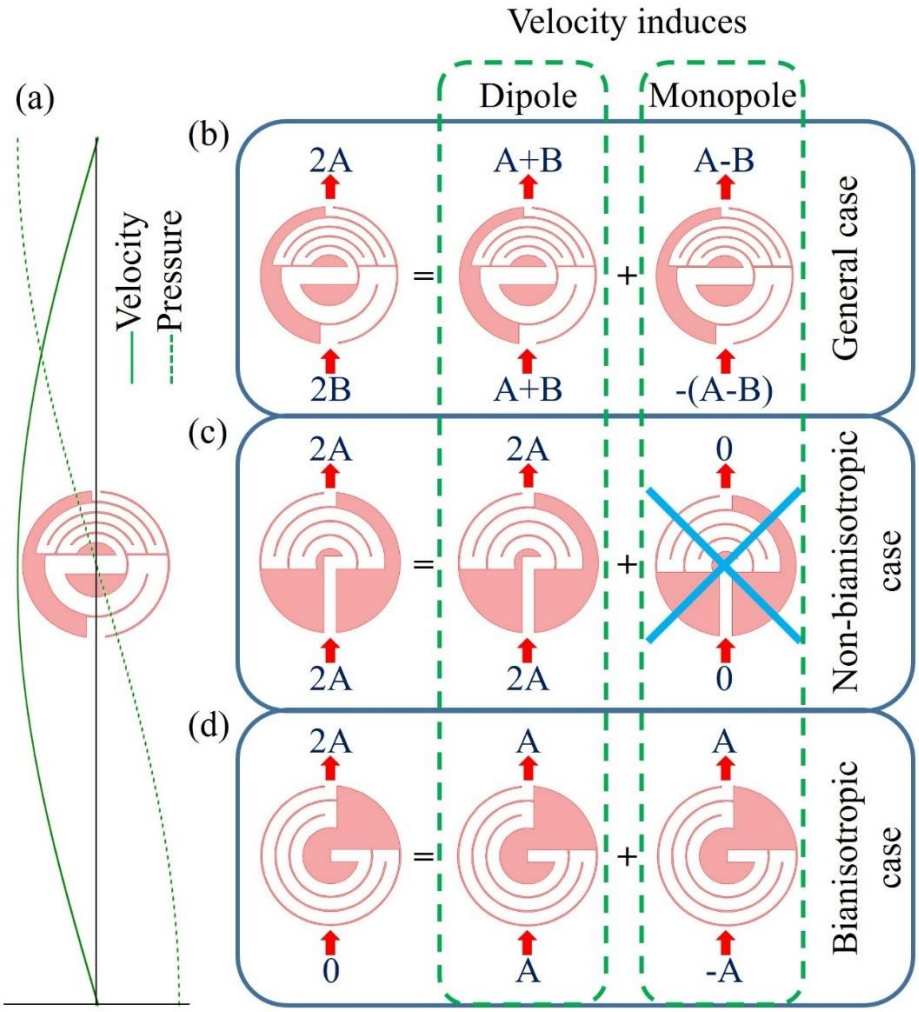

Figure 2.2. The physical interpretation of bianisotropic coupling for an acoustic bianisotropic particle. (a) A general bianisotropic particle located in a standing acoustic wave where the applied velocity has its maximum and the pressure is almost zero. (b) A general acoustic particle: Here, 2A indicates the total volume velocity coming out from the upper outlet and 2B indicates the total volume velocity getting into the lower outlet at a specific instant. (c) Symmetric acoustic scatterer. (d) Example of an asymmetric acoustic inclusion.

Consider a 2D cylindrical scatterer with mazelike channels, shown in Fig. 2.2 (a). The scatterer was placed in the pressure node of a standing wave where the velocity field reaches its maximum. For conventional non-bianisotropic scatterer, the velocity field can only generate a dipole scattered field. However, if the particle is bianisotropic, an applied background velocity can induce not only dipole but also monopole contribution. Since the scatterer is asymmetrical in the *y*-direction, the vibration going in and out of the two outlets opened in the scatterer will result in different volume velocities, as assumed to be 2A and 2B, respectively. In the general case, as shown in Fig. 2.2 (b), we can decompose the overall polarization excited by the external field into dipole contribution with amplitude |A+B| and monopole contribution with amplitude |A-B|, respectively. Let's consider a special case when A=B, as shown in Fig. 2.2 (c), i.e. symmetric volume velocities from both outlets. In this case, the amplitude of dipole contribution becomes |2A| while the amplitude of monopole is zero, indicating only dipole moment is excited by the background velocity field, and therefore the scatterer is non-bianisotropic. Interestingly, although the scatterer showed in Fig. 2.2 (c) is not geometrical symmetrical in the *y*-direction, the scatterer itself is non-bianisotropic, indicating that zero Willis coupling is independent of the asymmetry of the internal maze of the structure and is guaranteed to the first-order approximation as long as the channel width is constant. Figures 2.2 (d) provides another special case when the apertures are extremely asymmetric, resulting in B=0. In this case, the amplitude of both scattered monopole and dipole are |A|, indicating the external velocity produces not only a scattered dipole but also a monopole response, which is direct evidence of Willis coupling.

2.3.3. DESIGN OF DIFFERENT WILLIS SCATTERERS

In this section, we provide our design of Willis scatterer with different Willis responses, from zero, mild to the maximum.

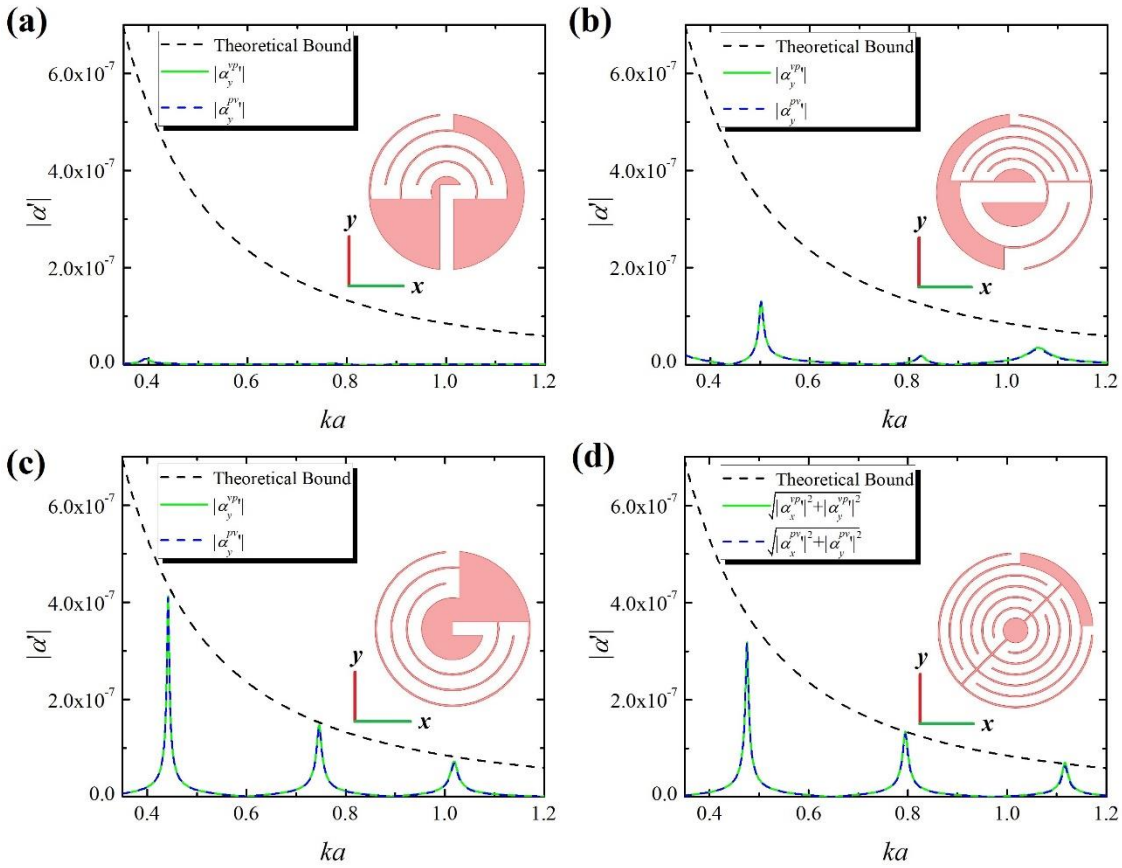

Figure 2.3. Comparison of the cross-coupling terms for different biansiotropic inclusions providing different levels of bianisotropic coupling. The radius of all inclusions is 5 cm. (a) Inclusion with constant channel width providing no bianisotropic coupling. (b) Inclusion with different channel width realizing moderate bianisotropic coupling. (c) Inclusion with only one outlet realizing maximum bianisotropy. (d) Inclusion with resonance in two directions.

Figures 2.3 (a), (b) and (c) show scatterers of different geometries with different levels of Willis coupling. All three scatterers are with a 5 cm radius and only resonate in the *y*-direction. The dashed black line indicates the bound of the maximum Willis response. Specifically, the scattered shown in Fig. 2.3 (a) is with a constant channel width, and therefore, the Willis response is very weak and almost zero, as seen in the figure. On the other hand, although the scatterer shown in Fig. 2.3 (b) is asymmetrical and also with outlets with different sizes, but is Willis response didn't reach it's maximum because its asymmetry is not strong. Finally, the particle in Fig. 2.3 (c) provides a strong Willis coupling, and at all three resonance frequencies, the response reaches the theoretical bound, since one of the apertures is closed. In Fig. 2(d), we show a bianisotropic scatterer with similar asymmetrical responses in both *x*- and *y*-directions. In this case, the general bound derived in Eq. (2.37) applied to the sum of two off-diagonal polarizability elements, where $\alpha_x^{vp\prime} = \alpha_y^{vp\prime}$.

In order to study the effect of loss on the influence of Willis response, we used the Thermoviscous Acoustics Module of COMSOL Multiphysics in order to take into account the real air parameters with viscosity loss and also thermal conductivity loss. Figure 2.4 compares the bianisotropic polarizabilities for lossy and lossless cases with the same geometry structures used in Fig. 2.3. These results indicate that although in the case of lossy particles, bianisotropic coupling polarizability decreases, the effect still remains very strong.

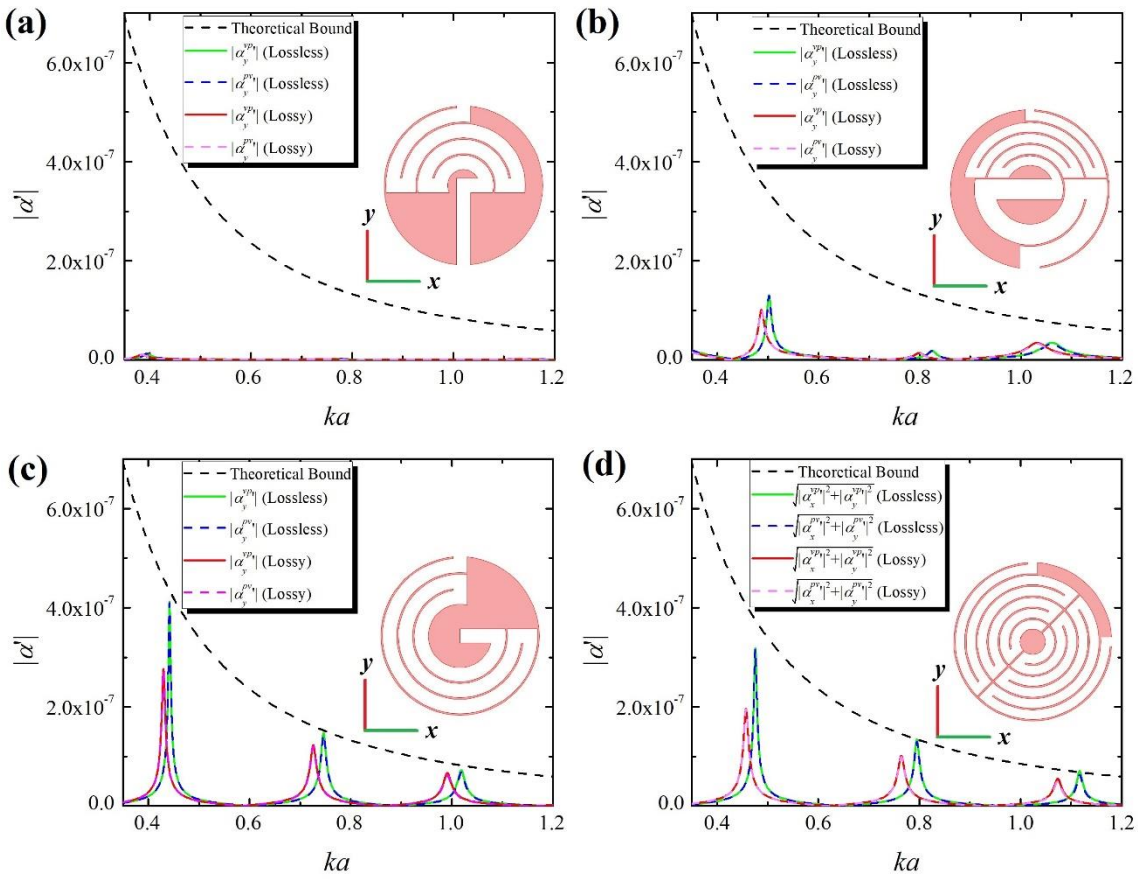

Figure 2.4. (a), (b), (c) and (d) Comparison of cross-coupling terms for lossy and lossless cases.

2.3.4 EXPERIMENTAL VERIFICATION OF MAXIMUM WILLIS COUPLING

In this section, we provide the experimental verification of maximum Willis coupling. The relevant results have been published in [58]. The experiment results were performed by Anton Melnikov and Yan Kei Chiang. My contributions consisted in performing Finite Element Methods calculations, optimize the design and support the numerical and analytical study.

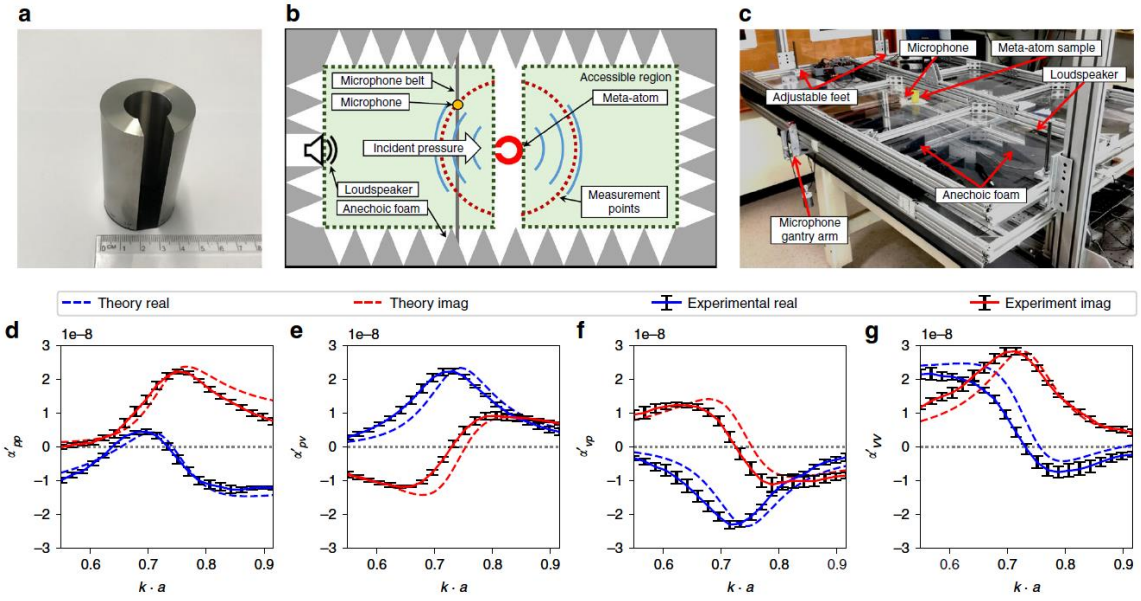

Figure 2.5. Experimental system and results. (a) Stainless steel sample: single aperture meta-atom with outside radius 2 cm and inside radius 1 cm. The opening mouth is 1.2 mm. (b), (c) Schematic and photograph of the experimental set-up. (d)-(g) Theoretically predicted and experimentally determined components of the normalized polarizability tensor.

In order to experimentally pushing the Willis coupling to the maximum and avoid the lossy effect as much as possible, we avoid the maze-like structure mention in the previous section but replace the resonance with Helmholtz Resonator. The sample is fabricated by stainless steel as shown in Fig. 2.5 (a). The experiment is performed inside a 2D waveguide with a height of 6.6 cm, and the set-up is shown in Fig. 2.5 (b) and (c). Figures 2.5 (d)-(g) show the theoretical and experimental results of the normalized values of the polarizability tensor. Reciprocity constraints on the polarizability that $\alpha^{vp\prime} = -\alpha^{pv\prime}$ has also been confirmed in Fig. 2.5 (e) and (f). The error bars indicate the standard

deviation of the experimentally extracted polarizability terms, obtained from the least-squares fit.

The magnitudes of polarizability components obtained in the experiment are shown in Fig. 2.6. All the values are normalized to the maximum bound of Willis coupling. Around $k \cdot a = 0.75$, the measured Willis coupling reaches its maximum, around 90% of the derived theoretical bound.

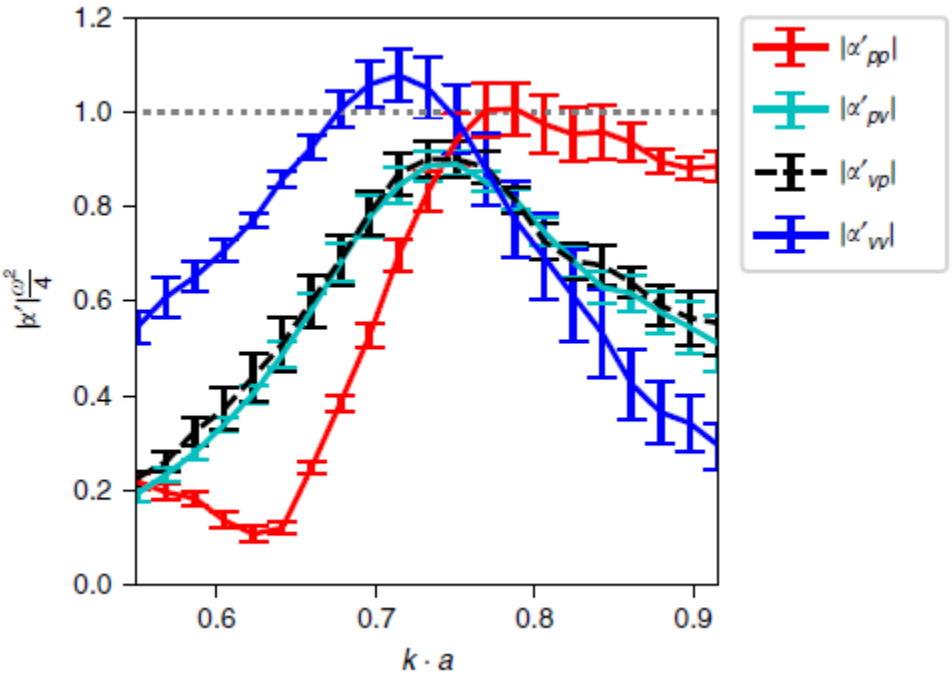

Figure 2.6. Experimental polarizability. Amplitudes of experimentally determined polarizability components showing shared magnitude closely to $k \cdot a = 0.75$.

2.4 Reciprocal Meta-grating

The systematic design of optimal Willis scatterers described in the previous sections enables translating many of the fascinating opportunities enabled by bianisotropy from electrodynamics to acoustics. In electromagnetics, bianisotropic inclusions have been utilized to the realization of the asymmetric absorbing metasurface, one-way transparent metasurfaces, and meta-gratings for perfect control of reflection [89]-[91]. Exploring the analogous effects in acoustics could translate these applications and manipulate sound in unprecedented ways. Recently research in electrodynamics reveals that the traditional gradient metasurfaces designed based on generalized laws of reflection and refraction [92] suffer from fundamental limitations on energy conversion efficiency. And the similar limitations have also been found in the acoustic gradient metasurfaces [93][94]. In electrodynamics, bianisotropic meta-gratings have been proposed and utilized to solve this problem. Specifically, through optimally arrange the period of the inclusions with proper bianisotropic effect, unitary efficiency of reflection could be achieved even when the reflection angle is very large. In this section, we will translate this idea into acoustics and design an acoustic meta-grating with the proposed Willis scatterers which can reroute the reflected waves into extreme angles with unitary efficiency.

The designed meta-grating composed with a periodic array of Willis scatterers with 4 cm in radius are shown in Fig. 2.7 (a). The Willis scatterers are similar to those

shown in Fig. 2.4 (c) and Fig. 2.5 (a), which only contains one outlet. The period of the meta-grating is 15 cm. A plate was placed below the bianisotropic inclusions.

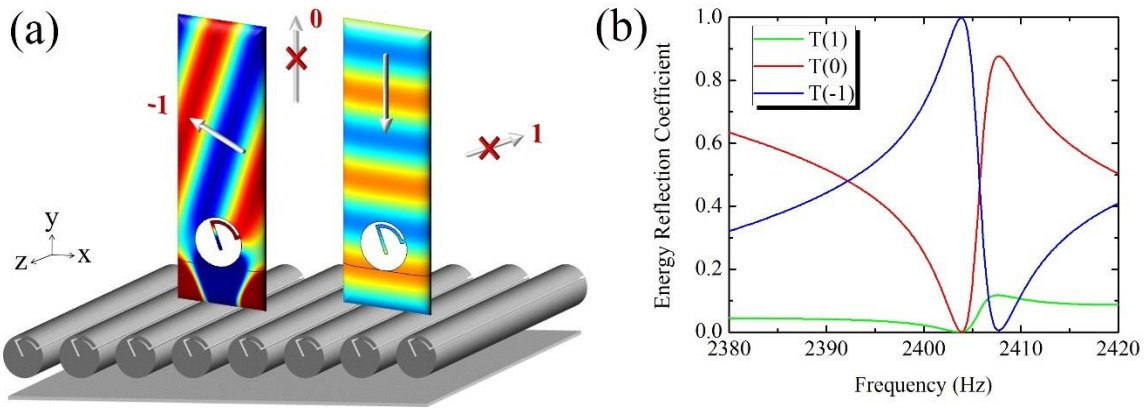

Figure 2.7. (a) Schematic of the designed acoustic meta-grating, and simulated distribution of incident and reflected pressure fields. Here the period of the grating is chosen to be 15 cm to ensure (-1), (0) and (1) modes are the only modes which can carry out energy, and all other modes are evanescent waves. The biansiotropy inclusion is 4 cm in radius. For a normally incident plane wave, by choosing proper inclusion, unitary reflections can be achieved as shown in the left panel. (b) Normalized reflection spectrum for different Floquet channels. When the operation frequency is near 2404 Hz, all incident energy is reflected into -1 Floquet channel and unitary reflection is achieved.

In our example, we would like to design a meta-grating that can redirect a normally incident wave to $\theta_{\text{ref}} = \theta_{(-1)} = -72^{\circ}$ with unitary efficiency. When a periodic array of bianisotropic scatterer over a hard plate is illuminated with a normally incident wave, the scattered power is carried out by different Floquet diffraction modes. Here, we choose the periodicity $b = \lambda / \sin\theta_{(1)}$ to ensure that the -1 Floquet channel is aligned with

the desired direction of reflection, i.e., $\theta_{(1)} = -\theta_{(-1)} = 72^{\circ}$. In such a situation, only -1, 0 and +1 Floquet channel can, in principle, carry power away from the meta-grating. All other channels are evanescent waves which cannot carry energy away. Through adjust the distance between the hard plate and optimize the Willis response of the scatterers, we are able to cancel the direct reflections in the 0 and +1 Floquet channel. As a result, all the incident wave is redirected to the only available reflection channel in -1 Floquet order. Figure 2.7 (b) presents the numerically studied reflection spectrum for each Floquet channel. When the operating frequency is around 2404 Hz, all incident energy is reflected into the -1 Floquet order, and anomalous reflection with unitary efficiency is achieved.

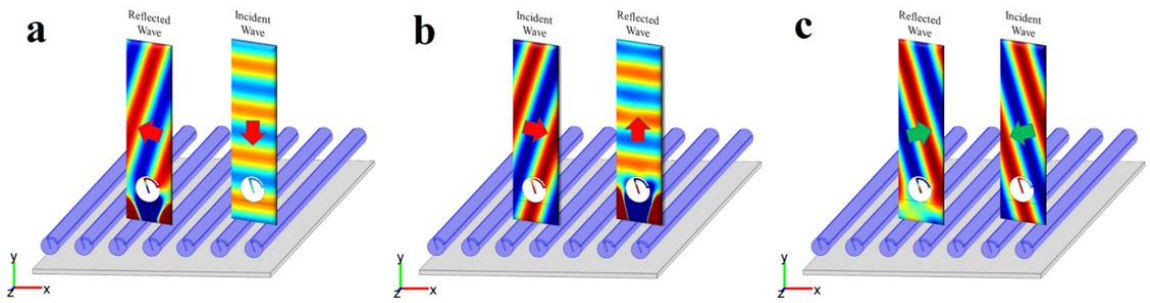

Figure 2.8. Scattering property of the bianisotropic meta-grating for waves coming from different directions.

Figure 2.8 presented the scattering property of the bianisotropic meta-grating for waves coming from different directions. In Fig. 2.8 (a), for waves coming from normal direction, the reflected wave is toward the left side. For waves incident from the left side, the reflected wave was in the normal direction, confirming the system's reciprocity. For

waves coming from the right direction, it will be reflected back also to the right direction. The scattering matrix can be expressed

$$S = \begin{pmatrix} 0 & 1 & 0 \\ 1 & 0 & 0 \\ 0 & 0 & 1 \end{pmatrix} \tag{2.54}$$

The scattering matrix satisfies the reciprocity condition $S = S^T$.

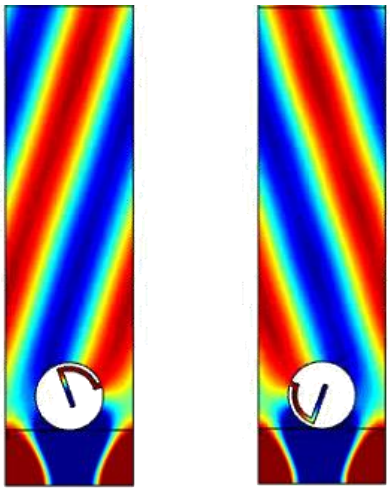

Figure 2.9. Meta-gratings designed for reflection towards different directions.

Figure 2.9 presents reflected field distribution of meta-gratings that could reroute incident waves into different directions when the incident beam is coming from the normal direction. The bianisotropic inclusion is identical in both of the cases. In order to change the reflected Floque channel from -1 to +1, we just need to rotate our inclusion

with a specific angle, and then all the incident energy can be rerouted to the opposite direction.

2.5 Design of Non-Reciprocal Willis Scatterer

The symmetry principle is one of the fundamental principles which has been greatly taken into consideration in devising new theories in science and solving problems in engineering [95]. This principle can be summarized as: the physical law of nature will not change if we change our observing view in certain ways [96]. A discrete symmetry is a kind of symmetry that describes non-continuous changes in a system, such as time-reversal and spatial inversion. Time reversal symmetry can be mathematically described as, by taking the transformation, $t \to -t$, physics laws still hold, such as Maxwell's Equations and sound wave equations. Spatial inversion symmetry can be interpreted similarly by taking the transformation, $\vec{r} \to -\vec{r}$. Breaking symmetry in physics systems will result in a variety of phenomena and enrich the diversity of our world, and hence have aroused great interests in the scientific community. For example, non-reciprocal phenomena are mainly attributed by breaking time-reversal symmetry, while breaking spatial inversion symmetry can often cause asymmetrical reflections [97].

In the previous section, we have discussed the relation between Willis response and the system's spatial inversion symmetry. By designing asymmetrical scatterers, we realize inclusions with different levels of Willis response. Time reversal asymmetry, as another aspect of discrete asymmetry, will reveal much richer physics and applications.

However, the properties of Willis coupling induced by breaking time-reversal symmetry has rarely been explored so far. In this section, we will explore the opportunity to induce Willis polarizability by breaking system time-reversal symmetry and the corresponding non-reciprocal properties of Willis scatterers. We generalize the maximum bound of the cross polarizability to the non-reciprocal case and show that the bound derived for the reciprocal inclusions can also be applied to the non-reciprocal one, as long as the inclusion is passive. We proposed the general mechanism to realize the maximum polarizability and introduce a systematical optimization strategy to reach the maximum cross-coupling even in the symmetrical inclusions with very weak bias. Finally, we apply these inclusions to design non-reciprocal unitary reflective meta-gratings.

2.5.1 BOUND OF NON-RECIPROCAL WILLIS SCATTERERS

The polarizability tensor for a subwavelength inclusion is provided in Eq. (2.20) and reciprocity requires that the normalized polarizability tensor satisfies $\ddot{\boldsymbol{\alpha}}^{vp'} = -\ddot{\boldsymbol{\alpha}}^{pv'T}$. For simplicity, we also consider the case in 2D. If we break reciprocity and make the inclusion non-reciprocal, then the only condition left over is energy conservation, as long as the inclusion is passive, which results in

$$\begin{cases} \sqrt{\left|\alpha_x^{vp\prime}\right|^2+\left|\alpha_y^{vp\prime}\right|^2} \le \sqrt{\dfrac{-\dfrac{8}{\omega^2}\mathrm{Im}\left(1/\alpha^{pp\prime}\right)-1}{\left|1/\alpha^{pp\prime}\right|^2}} \le \dfrac{4}{\omega^2} \\ \sqrt{\left|\alpha_x^{pv\prime}\right|^2+\left|\alpha_{yx}^{vv\prime}\right|^2} \le \sqrt{\dfrac{-\dfrac{8}{\omega^2}\mathrm{Im}\left(1/\alpha_{xx}^{vv\prime}\right)-1}{\left|1/\alpha_{xx}^{vv\prime}\right|^2}} \le \dfrac{4}{\omega^2} \\ \sqrt{\left|\alpha_y^{pv\prime}\right|^2+\left|\alpha_{xy}^{vv\prime}\right|^2} \le \sqrt{\dfrac{-\dfrac{8}{\omega^2}\mathrm{Im}\left(1/\alpha_{yy}^{vv\prime}\right)-1}{\left|1/\alpha_{yy}^{vv\prime}\right|^2}} \le \dfrac{4}{\omega^2} \end{cases} \tag{2.55}$$

Equation (2.55) is a general bound for either reciprocal and non-reciprocal inclusions, as long as the scatterer is passive. The results indicate that the previous maximum bound derived for reciprocal scatterers can also be applied to the passive non-reciprocal inclusions, i.e., the absolute value of the cross-coupling polarizabilities cannot go over $4\omega^{-2}$ even if we break reciprocity. If we further assume that the inclusion is only resonant in the *y*-direction, so that $\left|\alpha_y^{vp\prime}\right| \gg \left|\alpha_x^{vp\prime}\right|$, $\left|\alpha_{xy}^{vv\prime}\right| \approx \left|\alpha_{yx}^{vv\prime}\right| \approx 0$, Eq. (2.55) implies that when $\alpha^{pp\prime} = 4i\omega^{-2}$, pressure-induced dipole polarizability $\left|\alpha_y^{vp\prime}\right|$ reaches its maximum value $4\omega^{-2}$; and when $\alpha_{yy}^{vv\prime} = 4i\omega^{-2}$, velocity induced monopole polarizability $\left|\alpha_y^{pv\prime}\right|$ reaches its maximum value $4\omega^{-2}$, respectively. The designed particle is shown in Fig. 2.10 (a), which contains a circular cavity with 4 cm in radius on the top, with two holes, aligned in the *x*-direction, interacting with the outside field. Two identical cylindrical cavities are symmetrically placed on both sides of the circular cavity, just below the holes, and a third cylindrical cavity with different sizes is placed on the

backside, below the circular cavity, in the middle. And hence, the inclusion itself is symmetrical in the *x*-direction, and from the traditional perspective, this inclusion should have zero Willis coupling in the *x*-direction. However, if we apply rotation flow to the circular cavity, as indicated by the blue arrow, the situation would be different, as we know bias flow will break the system's reciprocity. We first perform the simulation through the commercialized Finite Element Method software COMSOL Multiphysics 5.4 by using Aeroacoustics Module, and assume the scatterer is passive and lossless. The simulated magnitudes of both cross-coupling polarizabilities $\left|\alpha_x^{pv\prime}\right|$ and $\left|\alpha_x^{vp\prime}\right|$ as a function of bias flow speed is presented in Fig. 2.10 (C), as indicated by the red and blue curves, respectively. The black curve is the theoretical bound of Willis coupling. At zero bias, the amplitudes of both cross-coupling polarizabilities are zero because the inclusion itself is symmetrical in the *x*-direction, or in other words, the inclusion satisfies spatial inversion symmetry in the *x*-direction. As the bias flow increasing, both of the cross-coupling polarizabilities increases at first, then reach their maximum $4\omega^{-2}$ very quickly at *v*=4 m/s, and after that, the cross-coupling polarizabilities start deceasing. Figures 2.10 (d) and 2.10 (e) present the dispersion relations of the two cross-coupling polarizabilities when the bias is 4 m/s. From Fig. 2.10 (e), we find the cross-coupling polarizabilities are identical with each other, satisfying $\alpha_x^{vp\prime} = \alpha_x^{pv\prime}$. Hence, through breaking the system's time-reversal symmetry, at a very weak bias flow and certain frequency, this non-reciprocal Willis inclusion shares the same maximum magnitude with the reciprocal Willis inclusion, and also with the same value.

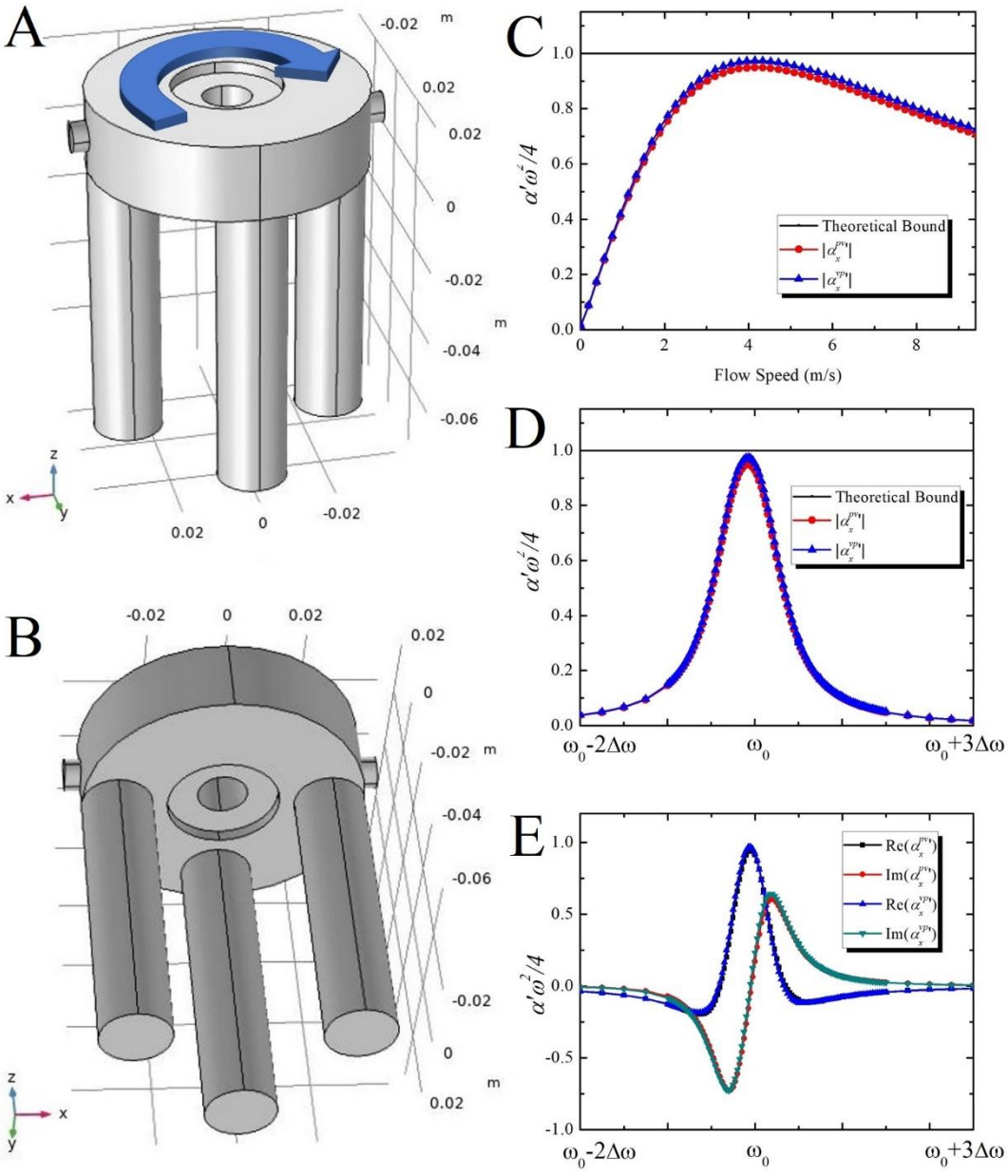

Figure 2.10. (a) and (b) Top and bottom view of the designed non-reciprocal scatterers. (c) Cross-coupling polarizabilities as a function of bias flow. (d) and (e) Dispersion relation of cross-coupling polarizabilities when the bias is 4 m/s.

2.5.2 CONSTRAINT ON THE PASSIVE AND LOSSLESS SCATTERER

It is very interesting to find that the bias flow can only change cross-coupling polarizabilities, but their amplitudes are still identical, the same as in the reciprocal case. To figure out the underlying mechanism, we recall that the inclusion itself under our study is passive and lossless, so that the cross-coupling polarizabilities can reach their maximum. The lossless condition also forces the off-diagonal terms in the energy conservation restrictions to be identical, and hence the inequality shown in Eq. (2.25) need to be equality

$$\omega^2\left(\ddot{\boldsymbol{\alpha}}'^{*T}\ddot{\boldsymbol{\alpha}}'\right)=4i\left(\ddot{\boldsymbol{\alpha}}'^{*T}-\ddot{\boldsymbol{\alpha}}'\right) \tag{2.56}$$

For the scatterer only resonant in the *y*-direction, the condition can be simplified as

$$\left(\omega^2\alpha^{pp'}-4i\right)\alpha_y^{pv'*}+\left(\omega^2\alpha_{yy}^{vv'}-4i\right)^*\alpha_y^{vp'}=0 \tag{2.57}$$

We can rewrite it as

$$-\frac{\alpha_y^{vp'}}{\alpha_y^{pv'*}}=\frac{\left(\alpha^{pp'}-\dfrac{4i}{\omega^2}\right)}{\left(\alpha_{yy}^{vv'}-\dfrac{4i}{\omega^2}\right)^*} \tag{2.58}$$

Also taking the conjugate of Eq. (2.58), we have

$$-\frac{\alpha_y^{vp'*}}{\alpha_y^{pv'}}=\frac{\left(\alpha^{pp'}-\dfrac{4i}{\omega^2}\right)^*}{\left(\alpha_{yy}^{vv'}-\dfrac{4i}{\omega^2}\right)} \tag{2.59}$$

Multiply Eq. (2.58) with (2.59), we get

$$\left|\frac{\alpha_y^{vp'}}{\alpha_y^{pv'*}}\right|^2=\frac{\left(\alpha^{pp'}-\frac{4i}{\omega^2}\right)\left(\alpha^{pp'*}+\frac{4i}{\omega^2}\right)}{\left(\alpha_{yy}^{vv'}-\frac{4i}{\omega^2}\right)\left(\alpha_{yy}^{vv'*}+\frac{4i}{\omega^2}\right)}=\frac{\left|\alpha^{pp'}\right|^2-\frac{8}{\omega^2}\mathrm{Im}\left(\alpha^{pp'}\right)+\frac{16}{\omega^4}}{\left|\alpha_{yy}^{vv'}\right|^2-\frac{8}{\omega^2}\mathrm{Im}\left(\alpha_{yy}^{vv'}\right)+\frac{16}{\omega^4}} \tag{2.60}$$

For lossless scatterers, Eqs. (2.55) can be rewritten as

$$\left|\alpha_x^{vp'}\right|^2=\frac{-\frac{8}{\omega^2}\mathrm{Im}\left(1/\alpha^{pp'}\right)-1}{\left|1/\alpha^{pp'}\right|^2}=\frac{8}{\omega^2}\mathrm{Im}\left(\alpha^{pp'}\right)-\left|\alpha^{pp'}\right|^2 \tag{2.61}$$

$$\left|\alpha_y^{pv'}\right|^2=\frac{-\frac{8}{\omega^2}\mathrm{Im}\left(1/\alpha_{yy}^{vv'}\right)-1}{\left|1/\alpha_{yy}^{vv'}\right|^2}=\frac{8}{\omega^2}\mathrm{Im}\left(\alpha_{yy}^{vv'}\right)-\left|\alpha_{yy}^{vv'}\right|^2 \tag{2.62}$$

Substitute Eqs. (2.61) and (2.62) into the right part of Eq. (2.60), we get

$$\frac{\left|\alpha_y^{vp'}\right|^2}{\left|\alpha_y^{pv'}\right|^2}=\frac{\left|\alpha^{pp'}\right|^2-\frac{8}{\omega^2}\mathrm{Im}\left(\alpha^{pp'}\right)+\frac{16}{\omega^4}}{\left|\alpha_{yy}^{vv'}\right|^2-\frac{8}{\omega^2}\mathrm{Im}\left(\alpha_{yy}^{vv'}\right)+\frac{16}{\omega^4}}=\frac{-\left|\alpha_y^{vp'}\right|^2+\frac{16}{\omega^4}}{-\left|\alpha_y^{pv'}\right|^2+\frac{16}{\omega^4}} \tag{2.63}$$

Simplify Eq. (2.63) and we can easily get the condition $\left|\alpha_y^{vp'}\right|^2=\left|\alpha_y^{pv'}\right|^2$, or

$$\left|\alpha_y^{vp'}\right|=\left|\alpha_y^{pv'}\right| \tag{2.64}$$

Now we have proved that when the scatterer is passive and lossless, the magnitude of two cross-coupling polarizabilities should be identical, no matter whether the scatterer itself is reciprocal or non-reciprocal. Specifically, when the system's time-reversal symmetry is broken but spatial inversion symmetry holds, the Willis polarizabilities are identical, while when the system's spatial inversion symmetry is broken but time-reversal symmetry holds, the Willis polarizabilities are with opposite

signs. When both time-reversal and spatial inversion symmetry are broken, the phases of both Willis polarizabilities are arbitrary, but their amplitudes are identical with each other.

2.5.3 EXPERIMENTAL REALIZATION OF NON-RECIPROCAL WILLIS SCATTERERS

To verify the effectiveness of our numerical results, we built our sample as shown in Figures 2.11 (a) and 2.11 (b). The sample was fabricated with brass material, and a shaft is connected to the motor which could constantly generate the rotational flow inside the circular cavity. In our experiment, the sample was placed in a two-dimensional waveguide, whose size was 1.83 meters long by 1.83 meters wide. The height of the two-dimensional waveguide was 2.5 cm. Sound-absorbing materials are placed on the boundary of the waveguide to ensure the free acoustic field environment. Eight microphones are placed 38.1 cm away from the center to measure the scattered fields, as indicated by Fig. 2.11 (c). The retrieved magnitude of $\left|\alpha_x^{pv'}\right|$ and $\left|\alpha_x^{vp'}\right|$ as a function of applied motor voltage are presented in Fig. 2.11 (d). When the applied voltage is around 16.5 V, the cross-coupling polarizabilities reach their maximum. As motor voltage continuous increases, the cross-coupling polarizability decreases, which consists of our numerical results. Figures 2. 11(e) and 2.11 (f) present the cross-coupling polarizabilities as a function of frequency with motor voltage 16.5 V. The profile is similar to our numerical results indicated in Fig. 2.10 (d) and 2.10 (e), and also prove that the two cross-coupling polarizabilities are identical with each other, which is different from the reciprocal sample shown in the previous section in which the Willis coupling

polarizabilities are with opposite signs.

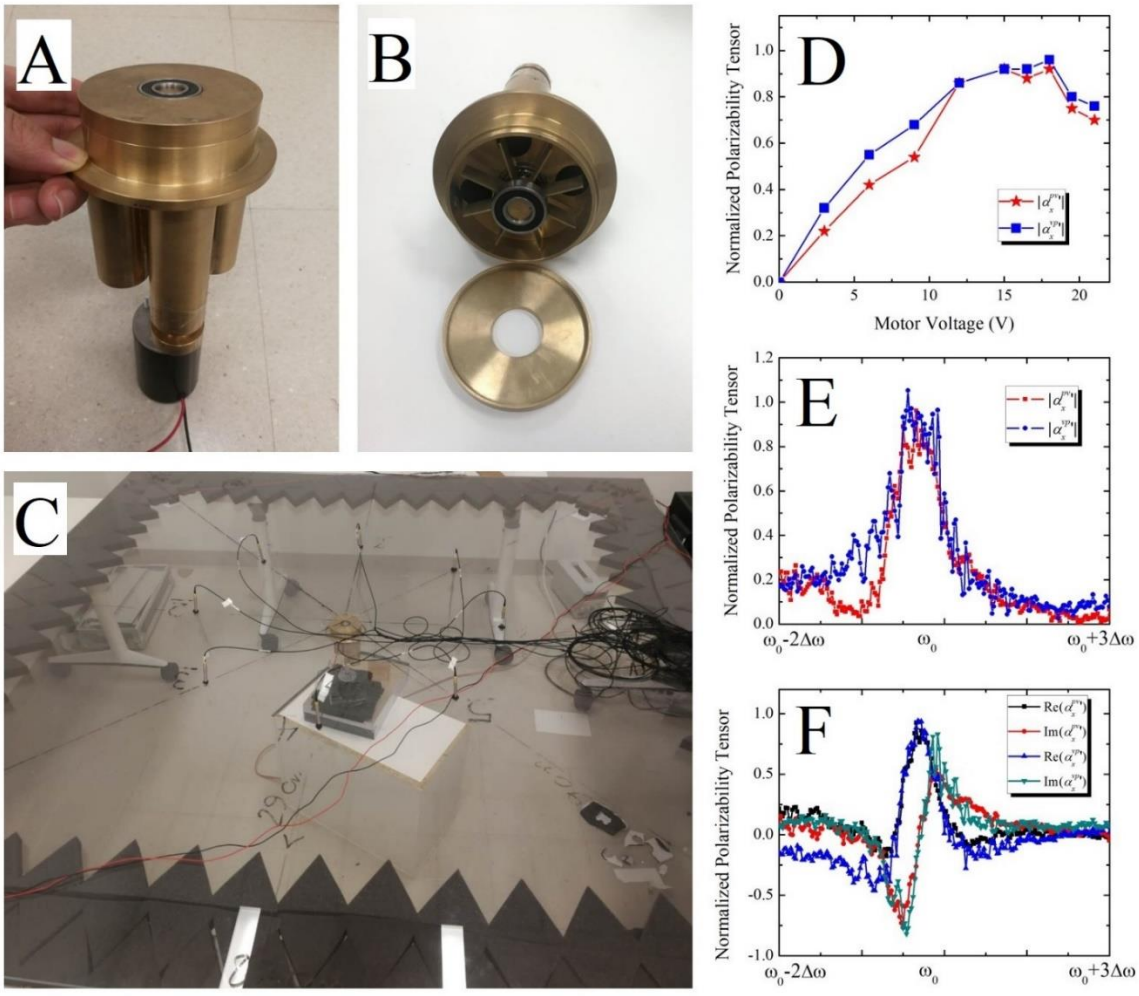

Figure 2.11. (a) and (b) Real fabricated sample. (c) Experimental set-up. (d) Measured cross-coupling polarizabilities as a function of motor voltage. (e) and (f) Experimental measured dispersion relation of cross-coupling polarizabilities when the motor voltage is 16.5 V.

2.5.4 PHYSICAL MECHANISM OF NON-RECIPROCAL WILLIS SCATTERERS

In order to get a deep insight into its physical mechanism, we plot the polarizabilities magnitude spectrum in Fig. 2.12 (a) when the bias flow is zero. In this case, due to the system is symmetrical, all the cross-coupling terms are zero, but only direct terms. Here, the peaks of $\left|\alpha^{pp'}\right|$ and $\left|\alpha_{vv}^{xx'}\right|$ are aligned together, indicating that the monopole resonance and dipole resonance happen at the same frequency. Figure 2.12 (b) presents the pressure field distribution inside the cavity when the inclusion was excited in the pressure field and velocity field, respectively. For the case without bias flow and induced in the pressure field, the field distribution in the inclusion is symmetrical, indicating the scattered field is monopole response. For the case without bias flow and induced in the velocity field, the field distribution in the inclusion is anti-symmetrical, indicating the scattered field is the dipole response. When applying bias flow in the circular cavity, the monopole mode and dipole mode are hybridized together, which resulted in the existence of Willis coupling. For the inclusion induced by pressure field for example, when bias flow is applied, the pressure inside the left cylindrical cavity is near zero. And hence only the cylindrical cavity and hole on the right are vibrating but the hole and cavity on the left are at rest. This mechanism of reaching maximum Willis coupling is similar to the realization of maximum reciprocal Willis inclusion, which only contains one outlet. For the inclusion induced by the velocity field however, when bias flow is applied, the pressure distribution reversed in the space, resulting in the pressure inside the right cylindrical cavity to be zero. In this scenario, only the hole and cylindrical cavity on the left side are vibrating but the hole in the right is at rest. This significantly

differs from the reciprocal Willis inclusion, because for the reciprocal inclusion with only one outlet, the vibrating outlet is always fixed at one side, no matter the inclusion is induced by the pressure field or the velocity field. And hence, the flipping vibrating holes inside the inclusion resulted in changing the sign of cross-coupling polarizabilities from reciprocal cases $\alpha_x^{vp\prime} = -\alpha_x^{pv\prime}$ to the non-reciprocal case $\alpha_x^{vp\prime} = \alpha_x^{pv\prime}$.

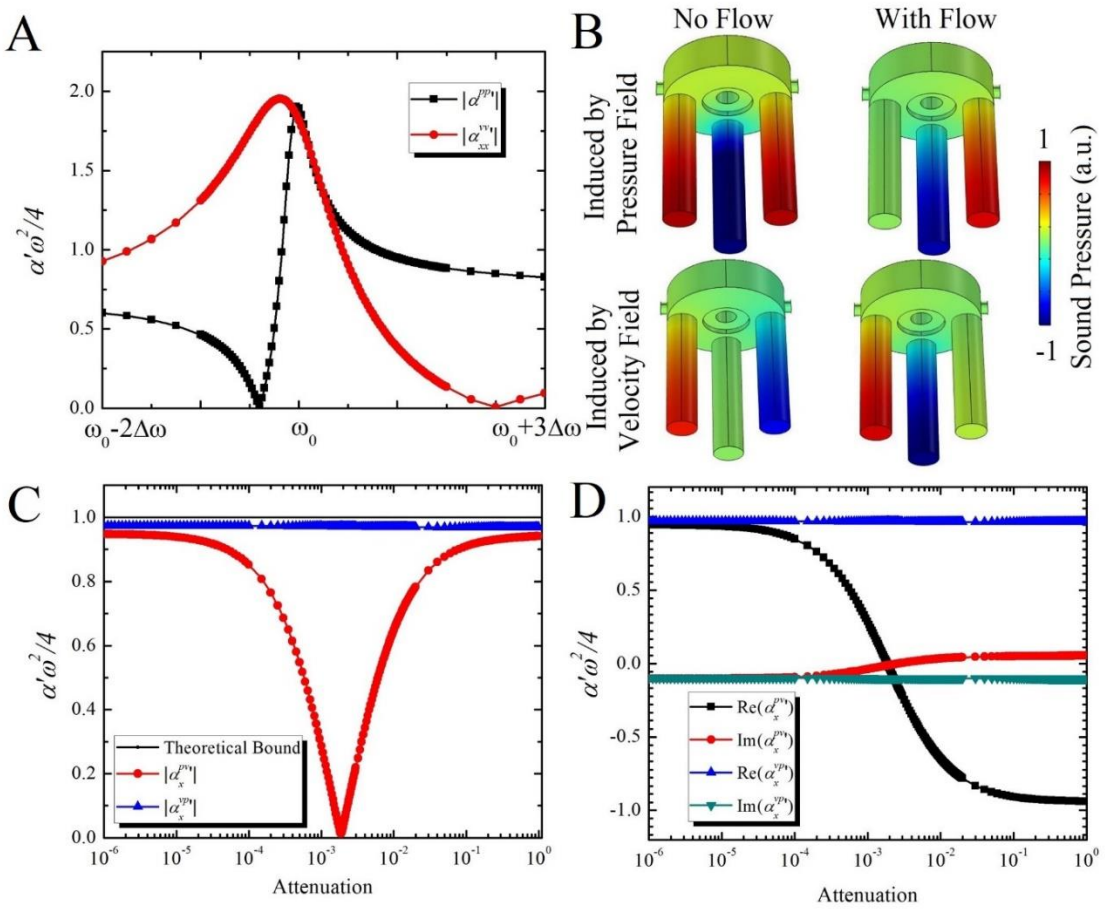

Figure 2.12. (a) Direct polarizability when the bias flow is zero. (b) Pressure distribution inside the inclusion when it is induced by pressure field and velocity field, respectively. (c) and (d) Cross-coupling polarizabilities change as a function of attenuation.

If we introduce lossy effects into the system, there will be even more interesting phenomena. We set the sound speed of the left cylindrical cavity as $c_0(1+i\alpha)$, but all other cavities keep to be lossless. Here α indicates the attenuation inside the cavity. Figures 2.12 (c) and 2.12 (d) present the cross-coupling polarizabilities as a function of attenuation α. We find that $\alpha_y^{vp'}$ is insensitive to the attenuation and constantly close to its maximum. $\alpha_y^{pv'}$, however, changes rapidly as the attenuation changes. When the attenuation reaches a specific value, $\alpha_y^{pv'}$ becomes zero while $\alpha_y^{vp'}$ is near its maximum value. We stress that this remarkable result can only happen in non-reciprocal scatterers, because in reciprocal scatterers, the magnitudes of both cross-coupling polarizabilities must be identical but with opposite signs, even when the lossy effect is introduced. As the attenuation continuous increase, $\alpha_y^{pv'}$ flip its sign and achieving $\alpha_x^{vp'} = -\alpha_x^{pv'}$ when the attenuation is very large. This is because very high attenuation will result in the impedance mismatch between the circular cavity and the cylindrical cavity. In this case, only the cylindrical cavity in the right side can vibrate, and hence breaking the system's spatial inversion symmetry.

2.6 Non-reciprocal Meta-grating

The discovery of meta-grating with bianisotropic inclusions discussed in Section 2.3 provides a new approach to realize passive unitary reflection, however, these meta-gratings foci on the reciprocal beam steering. Here, we apply the non-reciprocal Willis

scatterers proposed in the last section into the meta-grating design and achieve meta-grating with non-reciprocal unitary reflection.

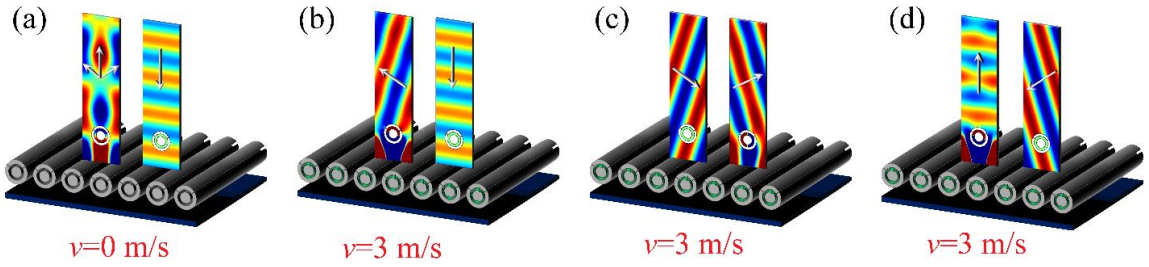

Figure 2.13. Schematic of the acoustic meta-grating and the pressure distribution of incident and reflected waves. (a). When there is no bias, for a normally incident plane wave, reflections can be found in all Floquet channels. (b) When the bias is 3 m/s, for a normally incident wave, unitary reflection is achieved by redirecting all energy into -1 channel. (c) For a -1 channel incoming wave, unitary reflection is achieved by redirecting all energy into +1 channel, instead of 0 channel, which confirms the non-reciprocity. (d) For a +1 channel incident wave, unitary reflection is achieved by redirecting all energy into 0 channel.

The inclusion is 4 cm in radius and is fully symmetrical in the left and right parts. The period of the inclusion is chosen to be 15 cm. For a normal incident wave, the refection contains all propagation channels including -1, 0 and +1. All other Floque modes are evanescent modes. As shown in Fig. 2.13 (a) when there is no bias applied in the inclusion, the reflected wave is fully symmetrical because the inclusion is symmetrical. When we apply weak bias inside the inclusion, i.e. 3.5 m/s, the system's symmetry is greatly broken and all normal incident energy is redirected into the -1 channel, as shown in Fig. 2.13 (b). For an incident wave coming from the left side, i.e. -1

channel, the reflected wave is transmitted into +1 channel instead of 0 channel, as shown in Fig. 2.13 (c), which confirms the non-reciprocal properties of our meta-grating. Figure 2.13 (d) presents the incident and reflected wave. When the incoming wave is from the right side, the reflected wave is in the normal direction, which further verified the non-reciprocal properties of our meta-grating.

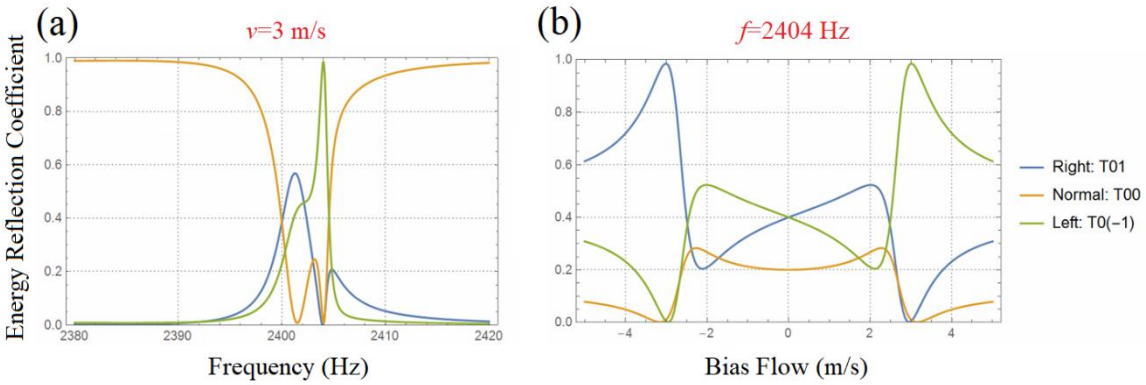

Figure 2.14. (a) Normalized reflection spectrum for different channels when bias flow is 3 m/s. When the operation frequency is near 2404 Hz, all normal incident energy is reflected into -1 Floquet channel. (b) Normalized reflection as a function of bias flow when the frequency is 2404 Hz.

Figure 2.14(a) presents the dispersion of the reflection coefficient for normal incidence when the bias is 3 m/s. At 2404 Hz, all incident energy can be fully reflected into channel -1. Figure 2.14 (b) presents the reflection coefficient as a function of bias flow. The coefficients for -1 and +1 channels are anti-symmetrical with each other for clockwise and anticlockwise bias flow.

CHAPTER 3: NONLOCAL RESPONSE IN BULK METAMATERIALS

In Chapter 2, we focused on the nonlocal response of a single inclusion and discussed both reciprocal and non-reciprocal properties. In this chapter, we focus on the nonlocal response in bulk metamaterials and their behavior on the macroscopic scale. The relation between non-reciprocity and the nonlocal response is also clarified.

3.1 Waves in Nonlocal Metamaterials

In order to study wave propagation in nonlocal metamaterials, we write the 1D mass conservation equation and momentum equation considering the Willis terms in the frequency domain

$$\partial u/\partial x = i\omega\left(\kappa_{eff}\, p + \xi_{eff}\, u\right) \tag{2.65}$$

$$\partial p/\partial x = i\omega\left(\rho_{eff} u + \varsigma_{eff}\, p\right) \tag{2.66}$$

Here κ_{eff} is the effective compressibility, ρ_{eff} is the effective density, ξ_{eff} and ς_{eff} are bianisotropy cross-coupling coefficients. Combing these two equations, we could derive the wave equation

$$\partial^2 p/\partial x^2 - i\omega\left(\varsigma_{eff} + \xi_{eff}\right)\frac{\partial}{\partial x}\, p + \omega^2\left(\rho_{eff}\kappa_{eff} - \xi_{eff}\varsigma_{eff}\right) p = 0 \tag{2.67}$$

Suppose the plane waveform e^{ikx}, Eq. (2.67) can be rewritten to

$$k^2 - \omega\left(\varsigma_{eff} + \xi_{eff}\right)k - \omega^2\left(\rho_{eff}\kappa_{eff} - \xi_{eff}\varsigma_{eff}\right) = 0 \tag{2.68}$$

And we can get the solution as

$$k_{\pm} = \pm \frac{\omega\sqrt{\left(\xi_{eff} - \varsigma_{eff}\right)^2 + 4\rho_{eff}\kappa_{eff}}}{2} + \frac{\omega\left(\xi_{eff} + \varsigma_{eff}\right)}{2} \tag{2.69}$$

Here, the first term with plus and minus sign indicates the reciprocal portion of the wavenumber, and the second term indicates the non-reciprocal portion of the wavenumber. When Willis coupling is zero, i.e. when both ξ_{eff} and ς_{eff} are zero, Eq. (2.69) can be simplified as

$$k_{\pm} = \pm\omega\sqrt{\rho_{eff}\kappa_{eff}} \tag{2.70}$$

From Eqs. (2.69) and (2.70), we conclude that non-reciprocity is related to Willis coupling. However, the existence of Willis coupling is not a sufficient condition to result in the non-reciprocity. For example, when both ξ_{eff} and ς_{eff} are nonzero but $\xi_{eff} + \varsigma_{eff} = 0$, the nonreciprocal portion, i.e. the second term, in Eq. (2.69) is zero, the wavenumber is still reciprocal, resulting in a reciprocal propagation of the sound wave. Only when both ξ_{eff} and ς_{eff} are nonzero, but their sum are also nonzero, then the system is non-reciprocal.

3.2 Non-Reciprocity

In the first section, we have discussed the relation between Willis coupling and non-reciprocity. A detailed introduction of non-reciprocity will be discussed in this section. Reciprocity is an important concept in wave physics, which requires that the response of a source keeps the same when the source and receiver are interchanged.

Breaking reciprocity could result in the different transmissions for opposite traveling directions, and is important for the protection of sensitive equipment from external interference and for full-duplex communications. In the field of electromagnetics, breaking reciprocity has been achieved with several approaches, including using external magnetic fields as bias [98]-[99], transistors [100]-[101], angular momentum [102]-[103], spatiotemporal modulation [104]-[105], and nonlinearities [106]-[107]. In acoustics, non-reciprocal devices have been mainly realized based on nonlinear mechanisms [108]-[109]. While it is well established that sound traveling parallel or anti-parallel to a moving medium is transmitted non-reciprocally [110], strong effects are typically achieved only when the velocity of the medium is large, or in highly resonant devices [111]-[112]. Based on this principle, momentum bias applied through moving media was recently used to realize linear acoustic non-reciprocal devices [113]. In the following, we explore moving metamaterials operated around their zero-index operation, showing how in this scenario mechanical motion opens highly unusual scenarios for sound propagation. We unveil the underlying physical mechanism in the presence of asymmetric Willis coupling, and use this feature to design a non-reciprocal lens which can realize focusing only on one side.

A moving medium exhibits different wave-vectors k_+ and k_- for opposite propagation directions, which is a signature of nonreciprocity. As such, the nonreciprocal coefficient

$$\eta = \left|\mathrm{Re}\left(k_+\right) + \mathrm{Re}\left(k_-\right)\right| \Big/ \left|\mathrm{Re}\left(k_+\right) - \mathrm{Re}\left(k_-\right)\right| \tag{2.71}$$

measures the degree of asymmetry in wave propagation for opposite directions. In absence of motion, k_+ and k_- are necessarily the same in magnitude and with opposite signs, hence $\eta = 0$, while η is nonzero when reciprocity is broken. In a moving medium, in the absence of frequency dispersion, we can write [114][115]

$$k_{\pm} = \pm k_R + k_{NR}, \text{ with } k_R = k_0 / \left(1 - M^2\right), \; k_{NR} = -Mk_0 / \left(1 - M^2\right), \tag{2.72}$$

where k_R, and k_{NR} are the reciprocal and non-reciprocal portions of the wavenumber, respectively, $M = U_0 / c_0$ is the Mach number, defined as the ratio of flow speed U_0 to the background sound speed c_0, and $k_0 = \omega / c_0$ is the wavenumber in free space. Replacing these quantities in Eq. (2.71) yields $\eta = \left| k_{NR} / k_R \right| = \left| M \right|$, implying that non-negligible non-reciprocity can be expected only for large, often impractical Mach numbers.

3.3 Non-Reciprocity in Zero-index Media

In order to break this trade-off and achieve large non-reciprocity with small flow speed, we explore the regime for which $k_R = 0$, i.e., zero-index propagation, so that the non-reciprocal portion of the wave-number k_{NR} dominates. In electromagnetics, epsilon-near-zero (ENZ) metamaterials [116] provide a reciprocal zero index of refraction, which has been shown to lead to extreme wave propagation properties [117][118]. Acoustic waves in a zero-index media may, therefore, provide a platform to boost nonreciprocal phenomena when modest medium speeds are considered. Density-

near-zero metamaterials [119][120], the analogue of ENZ materials for sound, have been realized in the past using waveguides loaded by membranes. However, this approach is not suitable for our purpose of realizing non-reciprocal wave transmission with the help of background flow, because conventional membranes would block the flow. We consider therefore extreme non-reciprocal responses by imparting airflow to waveguides loaded by a Helmholtz resonator array, inducing a near-zero refractive index at rest ($k_R \approx 0$), while $k_{NR} \neq 0$. In such a metamaterial, we expect that even a small mechanical motion yields a negative phase velocity (and refractive index) for propagation parallel to the fluid motion, and a positive one for propagation anti-parallel to it, hence $\eta = \left| k_{NR} / k_R \right| \to \infty \gg \left| M \right|$. In the following, we verify this response for plane-wave incidence, observing opposite refraction angles for excitation from opposite sides.

The geometry under analysis is shown in Fig. 3.1, and it consists of an array of parallel waveguides loaded with Helmholtz resonators. The green color indicates the region with airflow, and the geometrical parameters are provided in the caption. In order to impart airflow in each waveguide, a pipe is connected to both sides and loaded with a fan, (not shown in the figure), inducing a continuous airflow, as indicated by the arrows. These structures resemble Herschel-Quincke tubes [121]. The waveguides have a width S_w=3 mm, a distance d=8 mm between neighboring resonators, which have a neck length l=0.5 mm, a neck width a=1 mm, a cavity length b=7 mm and a cavity width h=3.5 mm. To ensure that the incident acoustic wave only travels through the waveguide, we load two Helmholtz resonators at each pipe opening (not shown), designed to filter out the

excitation frequencies. The structure is supplied with two matching layers at both sides (yellow color) in order to eliminate impedance mismatch, they do not support zero-index propagation, hence their width is compact.

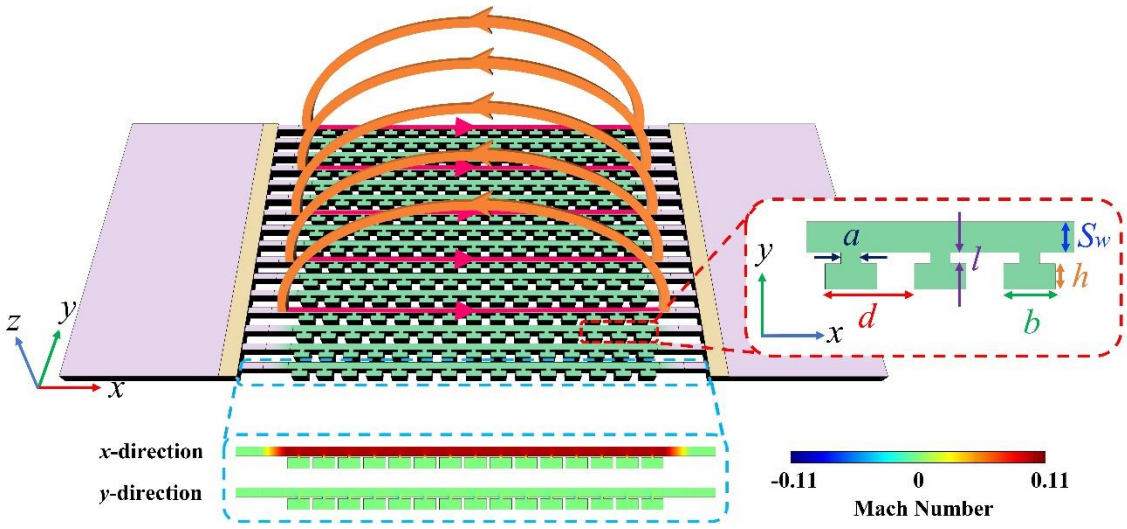

Figure 3.1. Geometry of the nonreciprocal metamaterial formed by an array of parallel waveguides loaded by Helmholtz resonators (green). A constant air flow inside the waveguides is generated by fans (red color and orange color indicate the flow inside the waveguide and the flow outside the *x*-*y* plane in the pipe, respectively). Two sets indicate the Mach number distribution in the waveguide between two matching layers and the enlarged structure of our microstructures, respectively.

The lower inset of Fig. 3.1 shows the calculated Mach number along each waveguide, zero outside the moving segment, and which linearly increases to an approximately constant value of 0.1 (i.e. 34.3 m/s) inside the waveguide through a finite transition layer. The small fluctuations of Mach number inside the waveguide are due to

the Helmholtz resonators. The focus of this section is to show how moderate constant flow can induce extreme non-reciprocal wave propagation and asymmetric Willis coupling. To keep simplicity but without losing generality, the background flow simulation has been performed with COMSOL Multiphysics, 2D Poisson's equation module. The module solves $\nabla \cdot \mathbf{U}_0 = f$, where f and $\mathbf{U}_0$ correspond to the source term and background flow speed. Source terms are placed at both sides of each waveguide to model the inlet and outlet connections to the pipe in the *z*-direction.

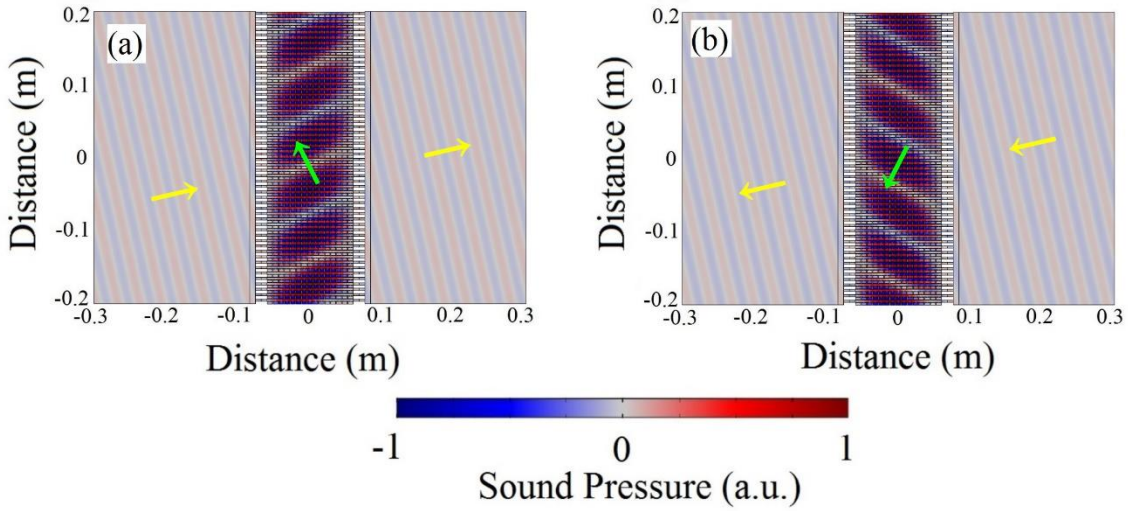

Figure 3.2. (a) Acoustic pressure distribution for an incident wave coming from the left. The yellow arrows indicate the wave vector in air and the green arrow indicates the wave vector in the metamaterial. (b) Acoustic pressure distribution for an incident wave coming from the right.

Consider now the excitation of this geometry with obliquely-incident plane waves from opposite sides, as shown in Fig. 3.2. The simulation is performed by COMSOL

Multiphysics with Aeroacoustics Module in 2D and the operation frequency is 11537 Hz. The actual background flow obtained from the simulations using the Poisson's equation Module is implemented into the Aeroacoustics Module to take into account the realistic medium flow in the waveguide. In our simulations, we use the continuity boundary conditions for acoustic pressure and particle velocity at the interface between the region with no motion and the matching layer, due to the material mismatch at these interfaces. At the interface between the region with no motion and the transition layer inside the waveguides, as well as at the one between the transition layer and the main body of the waveguide, we instead apply continuity boundary conditions for acoustic pressure and air mass flow [122]. The parameters of the two matching layers shown in Fig. 3.1 in the main paper are obtained from optimization, tailored to ensure the absence of reflection at the two interfaces for the considered geometry. They are ρ =1.4 kg/m^3 and c_0 = 369 m/s, with thickness 8 mm.

Figure 3.2 (a) presents the acoustic pressure field distribution for excitation from the left side. Due to momentum conservation, the tangential component of the wave-vector and transverse phase velocity is conserved, while the normal component changes direction across the interface, resulting in negative refraction. Quite interestingly, the situation is opposite for excitation from the right side: Figure 3.2 (b) presents the acoustic fields for an incident wave coming from the right side at the same incident angle. In this case, the direction of the normal component of the wave-vector does not flip as the wave enters the metamaterial, indicating positive refraction. This drastically different refraction response from opposite sides for modest values of M is a signature of extreme

nonreciprocity, arising from the slowly moving medium combined with the near-zero-index response in the metamaterial. Although the negative/positive phase index of the material is non-reciprocal, the energy velocity always flows away from the source, as expected from causality.

A better understanding of the phenomenon can be gained by extracting the effective constitutive parameters of the metamaterial. In a one-dimensional acoustic waveguide, the momentum equation, mass conservation equation and state equation are:

$$\rho_0\left(-i\omega+U_0\frac{\partial}{\partial x}\right)u=-\frac{\partial p}{\partial x} \tag{2.73}$$

$$\left(-i\omega+U_0\frac{\partial}{\partial x}\right)\rho'+\rho_0\frac{\partial u}{\partial x}+\frac{\rho_0 u_2}{S_w}=0 \tag{2.74}$$

$$p=c_0^2\rho'=\frac{\rho'}{\kappa_0\rho_0} \tag{2.75}$$

The relation between density, static density and the change of density caused by acoustic waves is $\rho=\rho_0+\rho'$, and the particle velocity satisfies $U=u+U_0$, where U_0 is the velocity of constant flow, u is the velocity caused by the sound wave. The term $\frac{\rho_0 u_2}{S_w}$ in Eq. (2.74) indicates the contribution of the Helmholtz resonators due to the mass conservation equation. Here, S_w is the cross-section of the waveguide and u_2 indicates the velocity contribution from the Helmholtz resonators

$$u_2=Y\sum_{n=-\infty}^{\infty}\left[H\left(x+\frac{a}{2}-nd\right)-H\left(x-\frac{a}{2}-nd\right)\right]p \tag{2.76}$$

where H is the Heaviside function, $Y = \dfrac{i\omega}{aM_a\left(\omega^2 - \omega_0^2\right)}$ is the acoustic admittance of the Helmholtz resonators, a is the width of the neck of the Helmholtz resonators, and ω_0 and M_a are the Helmholtz resonator's angular resonance frequency and acoustical mass, respectively. Since a is much smaller than the wavelength, we can use the approximation $H\left(x+\dfrac{a}{2}-nd\right)-H\left(x-\dfrac{a}{2}-nd\right)\approx a\delta(x-nd)$ and rewrite Eq. (2.76) as

$$u_2 = Ya\sum_{n=-\infty}^{\infty}\delta\left(x-nd\right)p \tag{2.77}$$

By combining Eqs. (2.73), (2.74) and (2.77), and solving for $\dfrac{\partial u}{\partial x}$ and $\dfrac{\partial p}{\partial x}$, we find:

$$\frac{\partial u}{\partial x} = i\omega\left[\left(\frac{\kappa_0 - \dfrac{Ya}{i\omega S_w}\displaystyle\sum_{n=-\infty}^{\infty}\delta\left(x-nd\right)}{1-M^2}\right)p - \frac{M}{\left(1-M^2\right)c_0}u\right] \tag{2.78}$$

$$\frac{\partial p}{\partial x} = i\omega\left[\frac{\rho_0}{1-M^2}u + \frac{M}{1-M^2}\left(\frac{\rho_0 c_0 Ya}{i\omega S_w}\sum_{n=-\infty}^{\infty}\delta\left(x-nd\right)-\frac{1}{c_0}\right)p\right] \tag{2.79}$$

Here we have renormalized the constant flow speed U_0 by Mach number, which is defined as the ratio of flow speed to the background sound speed, $M = U_0 / c_0$. In the subwavelength limit, we apply spatial averaging, which yields

$$\frac{\partial u}{\partial x} = i\omega\left[\left(\frac{\kappa_0 - \dfrac{1}{S_w dM_a\left(\omega^2-\omega_0^2\right)}}{1-M^2}\right)p - \frac{M}{\left(1-M^2\right)c_0}u\right] \tag{2.80}$$

$$\frac{\partial p}{\partial x} = i\omega\left[\frac{\rho_0}{1-M^2}u + \frac{M}{1-M^2}\left(\frac{\rho_0 c_0}{S_w d M_a\left(\omega^2-\omega_0^2\right)} - \frac{1}{c_0}\right)p\right] \tag{2.81}$$

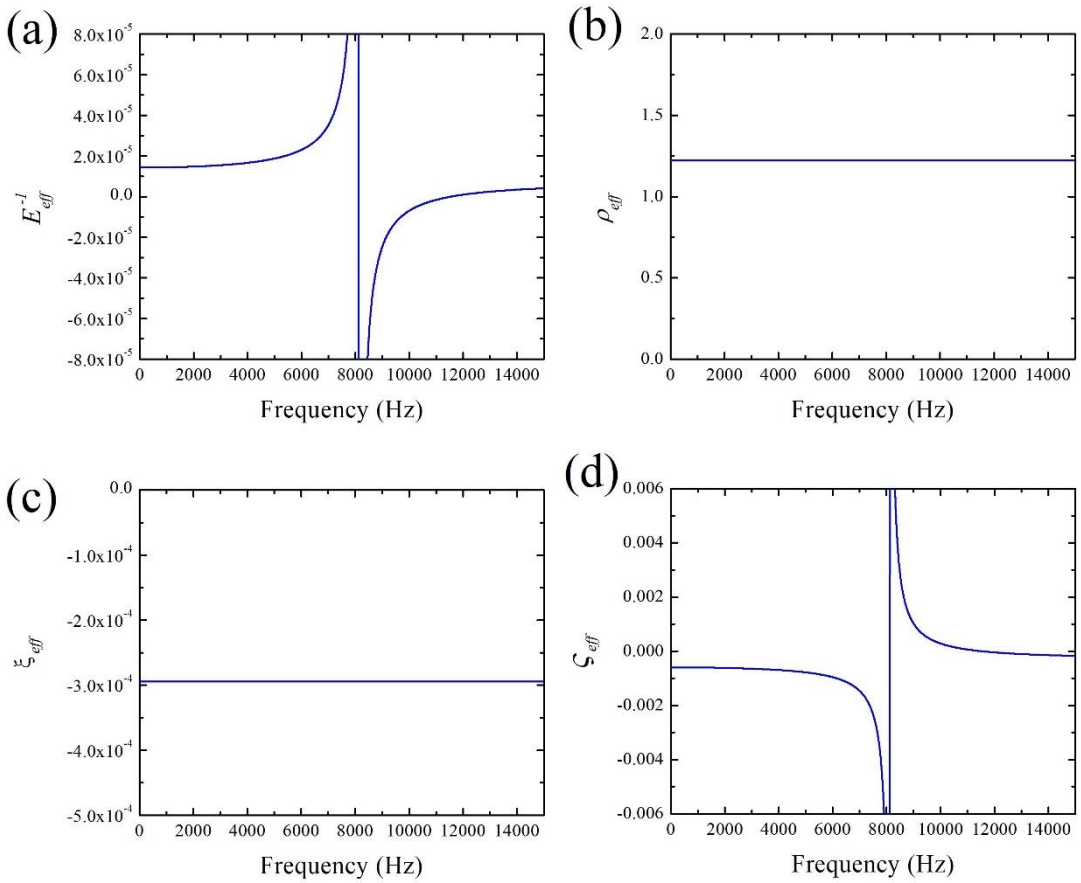

Figure 3.3. Dispersion relation of (a) effective bulk modulus, (b) effective density, (c) cross coupling term ξ_{eff} and (d) cross coupling term ς_{eff}.

We can then define $\kappa_{eff} = \left(1-M^2\right)^{-1}\left(\kappa_0 - F^{-1}\right)$ to be the effective bulk modulus, $\rho_{eff} = \rho_0\left(1-M^2\right)^{-1}$ to be the effective density, $\xi_{eff} = -M\left(1-M^2\right)^{-1}c_0^{-1}$ and

$\varsigma_{eff} = M\left(1-M^2\right)^{-1}\left(\rho_0 c_0 F^{-1} - c_0^{-1}\right)$ to be the Willis cross-coupling coefficients, and $F = S_w d M_a \left(\omega^2 - \omega_0^2\right)$ to be a factor that depends on the geometry of the structure. We stress the critical contribution of moving medium to the Willis cross-coupling terms. In the limit of *M*=0, these Willis cross-coupling coefficients also tend to zero. Eqs. (2.80) and (2.81) are the same as Eqs. (2.65) and (2.66) at the beginning of this Chapter. The calculated dispersion of the effective parameters of the metamaterial versus frequency is shown in Fig. 3.3. We stress that this effective medium model applies over a broad range of frequencies, not limited to the zero-index operation of the material, and it breaks down only when the wavelength in the material becomes comparable to the loading period.

The material flow introduces a strong asymmetry in sound propagation, inducing what is known as *bianisotropy*, a response that is highly anisotropic in nature, as it holds only for propagation along *x*, and at the same time couples together pressure and velocity through the Willis coupling terms ξ_{eff} and ς_{eff} [123][124]. The introduction of bianisotropy provides us an extra degree of freedom to control the sound propagation properties, especially relevant in the zero-index propagation regime. For a stationary waveguide loaded with Helmholtz resonators [44], which corresponds to our scenario in the limit of $M = 0$, only the compressibility $\kappa_{eff} = E_{eff}^{-1}$ is affected by the loads, yielding near-zero κ_{eff}, corresponding to a zero index of refraction, when $\kappa_0 = F^{-1}$. The effective density is not affected at all by the resonators. When a modest fluid motion is considered, however, the effective density and bulk modulus are weakly modified

through the factor $\left(1-M^2\right)^{-1}$, but most importantly they are coupled together through the bianisotropy coefficients ξ_{eff} and ς_{eff}. Different from conventional Willis coupling [76]-[81], these coefficients do not obey reciprocity, $\xi_{eff} \neq -\varsigma_{eff}$, and are odd with respect to M, i.e., they flip sign for opposite propagation directions, a clear sign of non-reciprocity. As we show in Fig. 3.3, around the resonance of Helmholtz Resonator, ς_{eff} goes through a resonance and flips sign, similar to κ_{eff}, producing extremely asymmetric Willis coupling coefficients and non-reciprocal response. As a note, applying space-time modulation will result in the emergence of the Willis coefficient [125]. In that work, the material properties are modulated in space and time in a wave-like fashion, i.e., $\kappa = \kappa(x - c_m t)$. In other words, the materials are considered in a moving frame. If we move our Helmholtz resonators with the bias flow in our sample, we will get similar result as what shown in [125]. However, by doing so, the non-reciprocal portion of the wavenumber will become zero when the reciprocal portion is zero. In our realization, the Helmholtz resonators are at rest, which largely couples them with the moving flow, resulting in the resonance profile of ς_{eff} and nonzero non-reciprocal wavenumber for zero reciprocal wavenumber.

By combining Eqs. (2.80) and (2.81), we derive the dispersion relation

$$k_{\pm} = \pm \frac{\omega\sqrt{\left(\xi_{eff} - \varsigma_{eff}\right)^2 + 4\rho_{eff}E_{eff}^{-1}}}{2} + \frac{\omega\left(\xi_{eff} + \varsigma_{eff}\right)}{2} \tag{2.82}$$

yielding

$$k_R = \frac{\omega\sqrt{\left(\xi_{eff} - \varsigma_{eff}\right)^2 + 4\rho_{eff}E_{eff}^{-1}}}{2} = \frac{k_0 c_0}{1-M^2}\sqrt{M^2\left(\frac{\rho_0 c_0 F^{-1}}{2}\right)^2 + \rho_0\left(E_0^{-1} - F^{-1}\right)} \tag{2.83}$$

$$k_{NR} = \frac{\omega\left(\xi_{eff} + \varsigma_{eff}\right)}{2} = -k_0\frac{M}{1-M^2}\left(1 - \frac{\rho_0 c_0^2 F^{-1}}{2}\right) \tag{2.84}$$

Notice the strong difference between these expressions and Eq. (2.72), which is consistent with Eq. (2.82) in the limit $F^{-1}=0$, i.e., without Helmholtz resonators. With the help of strong sound-matter interactions enabled by the metamaterial, we are able to realize zero-index k_R and at the same time, a non-negligible k_{NR}. At $\omega = \sqrt{\omega_0^2 + \left(1+\sqrt{1-M^2}\right)E_0 \Big/ \left(2S_w dM_a\right)}$, $k_R = 0$, and $\eta \to \infty$, largely enhancing the non-reciprocal response, due to asymmetric Willis coupling induced by the mechanical motion. In this regime, the wavenumber reads

$$k_{\pm} = k_{NR} = -k_0\frac{M}{\left(1+\sqrt{1-M^2}\right)\sqrt{1-M^2}} \tag{2.85}$$

enabling opposite refractive index for opposite directions of propagation. Interestingly, the wavenumber in the metamaterial has the same real value for both propagation directions, i.e., no matter whether the incident wave is coming from left or right, the wavevector has the same direction and value, anti-parallel to the fluid motion, consistent with our numerical simulations in Fig. 3.2. We stress that for $k_R = 0$ the effective bulk modulus is negative, $E_{eff}^{-1} = -\left(\xi_{eff} - \varsigma_{eff}\right)^2 \Big/ \left(4\rho_{eff}\right)$, and the effective density positive,

$\rho_{eff} = \rho_0 / \left(1 - M^2\right)$, yet the acoustic wave travels in the metamaterial without decay because of the strong Willis coupling response.

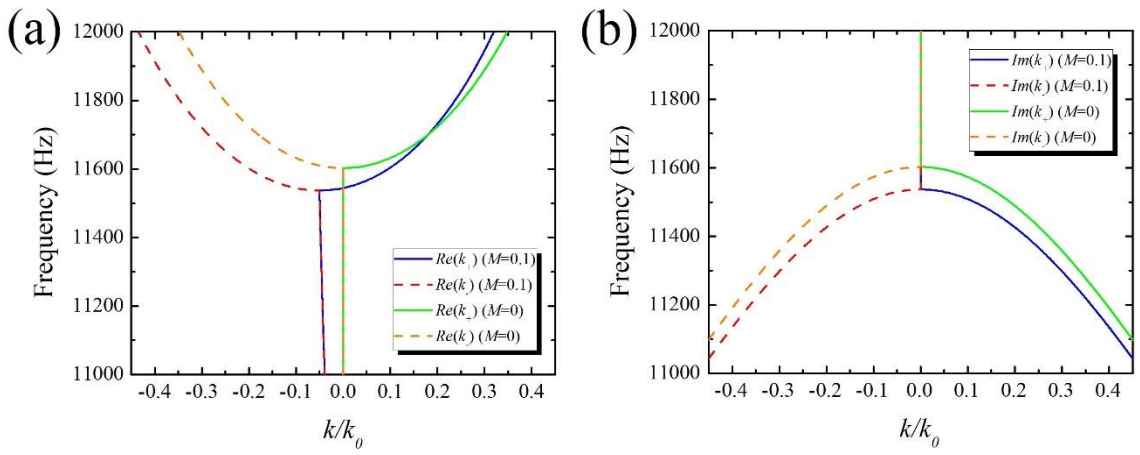

Figure 3.4. Dispersion diagram for the geometry of Fig. 3.1 calculated from Eq. (2.82). (a) Real part. (b) Imaginary part.

Figure 3.4 shows the wavenumber dispersion in Eq. (2.82). In absence of airflow (M = 0), the dispersion has a cut-off at the zero-index condition $\kappa_0 = F^{-1}$, and it is strictly even with respect to k, as expected from reciprocity. When a moderate air-flow is turned on (M = 0.1), the dispersion diagram is asymmetric, as expected for a nonreciprocal medium, and the cutoff frequency shifts down to $\omega = \sqrt{\omega_0^2 + \left(1 + \sqrt{1 - M^2}\right) E_0 \Big/ \left(2 S_w d M_a\right)}$. Around this frequency, waves propagating in opposite directions have a nonzero (negative) wavenumber, independent of the propagation direction, and the non-reciprocity coefficient η is very large. While in this

Section zero-index is achieved at the waveguide cut-off, a similar operation may be envisioned in other zero-index metamaterials, such as around Dirac points [126][127].

3.4 Non-Reciprocal Lens

The non-reciprocal Willis coupling induced through mechanical motion in Eq. (2.82) can also be used to create a lens that focuses a source placed at one side, but with diverging properties when a source is placed on the other side. The focusing operation is achieved by imparting a phase shift across the structure that transforms a diverging circular wavefront to a converging one, which is achieved tailoring the airflow velocity across different channels to accumulate the required phase at each aperture.

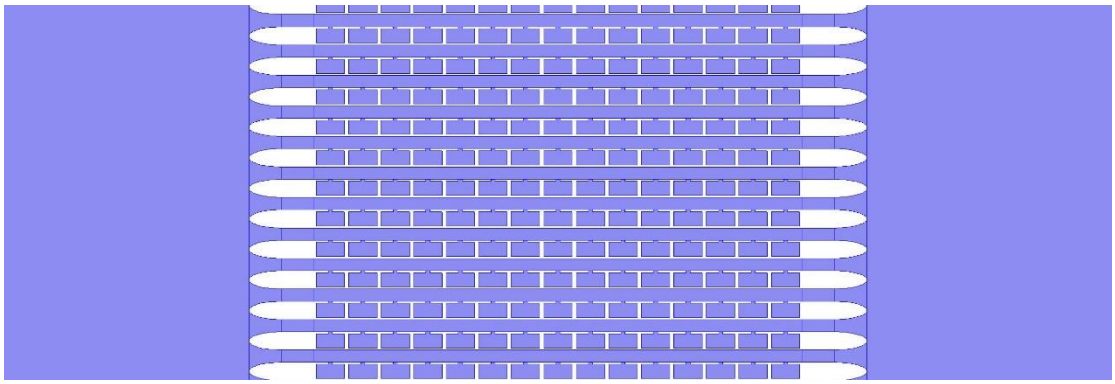

Figure 3.5. Geometry of the nonreciprocal lens.

In our realization of the nonreciprocal lens, we have to apply different flow speeds in different channels. For this reason, the local impedance changes from channel to channel, and the realization of the matching layer is not straightforward. In this

scenario, we removed the matching layer and introduced acoustic horns to minimize the reflection due to the change of waveguide cross-sections, independent of local changes in impedance due to the varying medium flow, as shown in Fig. 3.5. By numerical simulations, we obtain the relative phase shift as a function of Mach number, as shown in Fig. 3.6. The red line indicates the relative phase shift when the incident wave is coming from left and the blue line indicates the relative phase shift when the incident wave is coming from the right.

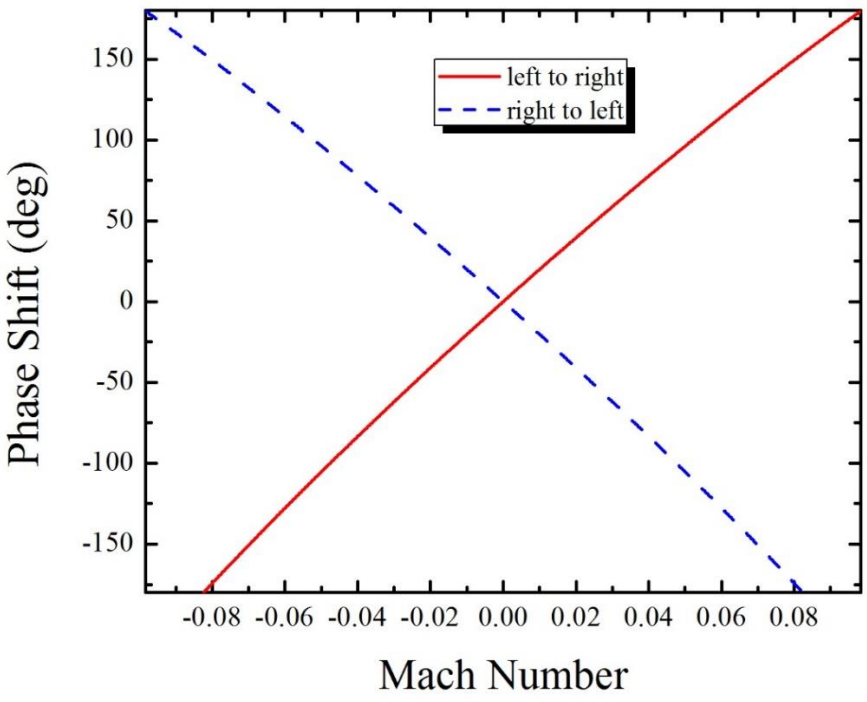

Figure 3.6. Relative phase shift as a function of Mach Number. The red line indicates the relative phase shift when the incident wave coming from left and the blue line indicates the relative phase shift when the incident wave coming from the right.

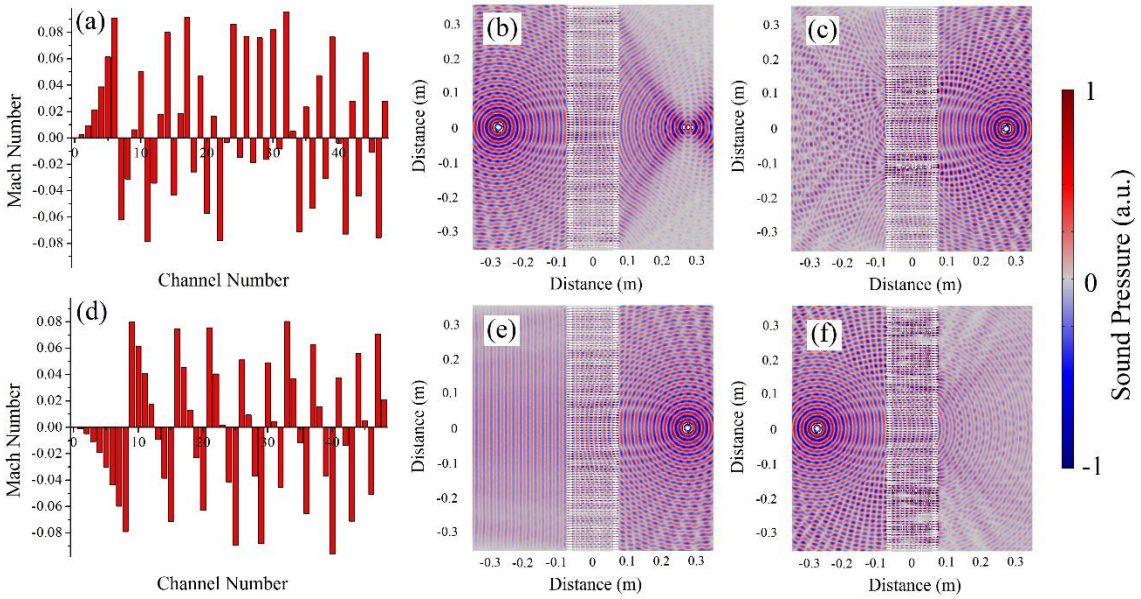

Figure 3.7. (a) Modulation of the Mach number in each channel to synthesize a focusing lens. (b) Acoustic pressure distribution when the source is located on the left side of the lens. A focused image is obtained on the right. (c) Acoustic pressure distribution when the source is located on the right of the lens. (d) Modulation of the Mach number to synthesize a point-source to plane wave converter. (e) Acoustic pressure distribution when the source is located on the right. A plane wave is induced on the left side. (f) Acoustic pressure distribution when the source is located on the left side.

For the non-reciprocal lens, we want to obtain an image when the source is located on the left side of the lens. Suppose that the distance between the source and the lens is *D*. Then, the relative phase distribution at the left interface of the lens is $-k\left(\sqrt{D^2+y^2}-D\right)$. For a focused image, the relative phase distribution at the right interface of the lens should be $k\left(\sqrt{D^2+y^2}-D\right)$. Therefore the relative phase shift for a

wave passing the lens should be $2k\left(\sqrt{D^2+y^2}-D\right)$. According to the red line shown in Fig. 3.6, we can get the wanted Mach Number in each channel as shown in Fig. 3.7.

In Fig. 3.7 (a), where we plot the relation between Mach number, maintained below 0.09 in each channel, and the channel number *n*, with $n = 0$ being the channel on the same axis as the source ($y = 0$). The airflow in each channel is symmetric with respect to the *y*-axis (i.e., for channels *N* and *–N* the airflow is the same), so we only show the imparted Mach number for positive *n*. Figure 4(b) shows the calculated acoustic pressure distribution when the sound source is located on the left of the lens: after traveling through the planar metamaterial, a focused image is constructed at the right side of the lens. Figure 4(c) presents instead the pressure distribution when the sound source is located at the right side of the lens: here we only get a divergent wave, demonstrating strong nonreciprocity with modest required flow velocities. The operation frequency here has been raised to 16 kHz to enhance the transmission for each different channel with different background flow. Operating away from the resonance frequency ensures that detuning each channel to achieve the desired phase pattern at the lens output does not affect the transmission amplitude through each channel, and that the response in time is very fast.

The time evolution of our non-reciprocal lens has been presented in Fig. 3.8 at different time instant, i.e. 0.1 ms, 1 ms, 2 ms, and 3 ms, respectively, indicating that our lens can achieve focus within several periods, i.e. less than 3 ms.

By adjusting the airflow in each channel, we can get different functionalities. In Figs. 3.7 (d)-(f) we show a design that converts a point source to a plane wave only when the source is located on the right side of the metamaterial. Again, the relation between channel number and Mach number is presented in Fig. 3.7 (d), while Figs. 3.7 (e)-(f) show the acoustic pressure profile when the source is located at the two sides of the structure, highlighting again the strongly non-reciprocal response.

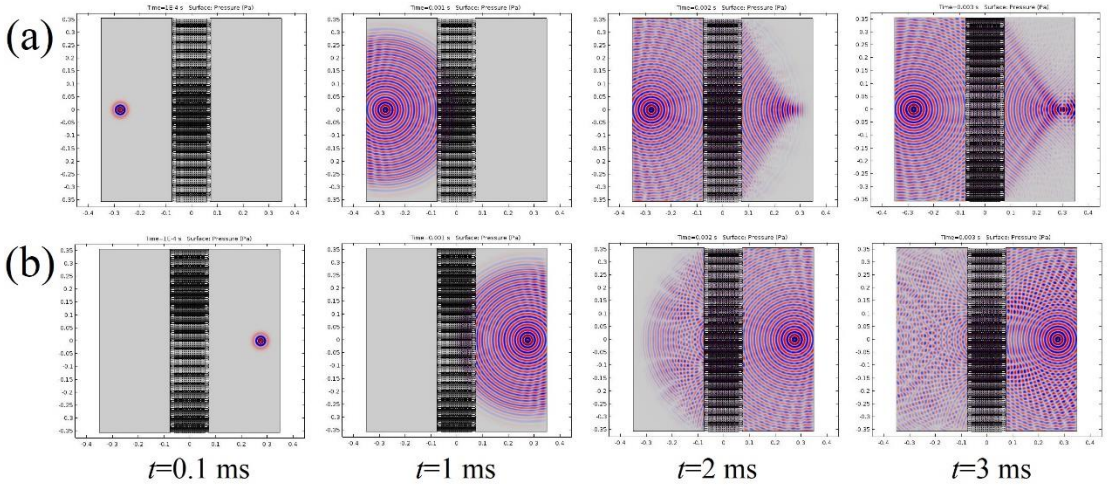

Figure 3.8. Time evolution of our non-reciprocal lens.

For the non-reciprocal point-source to plane wave converter, we want to obtain a plane wave when the source is located on the right side of the lens. Here, we also suppose that the distance between the source and the converter is *D*. The relative phase distribution at the right interface of the converter is $-k\left(\sqrt{D^2+y^2}-D\right)$. For a plane wave, the relative phase distribution at the left interface of the converter should be zero

(phases should keep the same along with the left interface). Therefore, the relative phase shift for the wave passing the converter should be $k\left(\sqrt{D^2+y^2}-D\right)$. According to the blue line shown in Fig. 3.6, we can get the wanted Mach number in each channel as shown in Fig. 3.7 (d).

3.5 Synthetic Phonon Cyclotron and Topological Effect

The research of interactions between matters and fields are one of the most important topics in physics due to its great potential applications and profound physical meanings. A century ago, physicists found both the electric field and magnetic field can interact with charged particles by applying an extra force, named electric field force and Lorentz force, respectively. The studies of these interactions resulted in fruitful applications in the 20^{th} century such as particle accelerator, electron microscopes, cathode-ray tubes and so on. While both electric force and magnetic force can derivate inside traveling charged particles' routes, their physical mechanism are quite different. The motion process of a charged particle in electric field is always associated with energy conversation between electric potential energy and kinetic energy. But in the magnetic field, there is no energy conversion in the process and kinetic energy is conserved.

These exciting application results stimulated scientists' interests to consider wave matter interactions in a broader range of particles, such as photons and phonons. Different from charged particles like electrons and protons, photons and phonons are neutral particles that normally do not directly interact with a static electric field and magnetic field. The appearance of metamaterials provides a new degree of freedom in

photon and phonon flow manipulation and huge amount of exciting progress have been reported recently, including transformation optics/acoustic for cloaking [32]-[33], omnidirectional absorber [128]-[131] and gradient lens [132]-[133]. All these mentioned manipulation strategies are realized through specific gradient index design which constructs an effective potential gradient for photons/phonons, an analogous approach in manipulating charged particles with electric potential. Thus, the deflection of incident optical/acoustic waves is associated with momentum change (i.e. wave-vector change).

Compared with the electric field, the interaction of the magnetic field with charged particles can result in more interesting phenomena, such as topological condensed matter [134]-[135], integer [136]-[137] and fraction quantum Hall effect [138]-[139], etc. In optics, some of the progress have been made recently in manipulating photons in a manner similar to the manipulation of charged particles using a magnetic field [140]-[143]. But in acoustics, this analogue is still lack of study. Although acoustic analogue of quantum spin Hall effect and topological insulator have also been proposed in recent years [144]-[147], these achievements, however, do not correspond directly to a magnetic field applied to charged particles. Acoustic waves, another type of classical wave, more general and ubiquitous in nature, are applied to varieties of situations. It is of fundamental interest to ask whether an analogous effective magnetic field can be created for phonons. Moreover, this study, if realized, will have potential implications in acoustic beam bending [148], acoustical tweezer design [149] and ultrasound imaging and therapy [150].

In this Section, we propose an effective magnetic field to manipulate phonons and show such an effective magnetic field can realize a synthetic phonon cyclotron which leads to the circular motion of sound beams by applying an effective Lorentz force to the traveling phonons. Although there is no naturally analogous magnetic fields for phonons due to its electric neutrality, the Aharonov-Bohm effect [151] points out an effective way in forming an effective magnetic field by creating a gauge field for phonons. We mimic the magnetic field effect by specifically modulating the non-reciprocal phase of our lattices, which neither need acoustical resonance nor nonlinear effect. The lattice configuration is based on acoustic coiling structures. But very different from previous reported acoustic coiling metamaterials works which investigated their reciprocal properties [152]-[153], here the work investigates the non-reciprocal properties of the coiling structure.

To address our idea, we first consider a two-port waveguide, as shown in Fig. 3.9 (a). Generally, for an incoming wave travel from point *a(x,y)* to point *b(x,y)*, the phase change can be accounted as two parts. One is the reciprocal phase Φ_r and the other is the non-reciprocal phase Φ_{nr}, respectively. Thus, the phase shift of the wave travels from point *a(x,y)* to point *b(x,y)* can be expressed as $e^{i(\Phi_r+\Phi_{nr})}$, as indicated by the red arrow in Fig. 3.9 (a). If we reverse the wave traveling direction, the reciprocal phase will reverse its sign while the non-reciprocal phase will keep its sign. Thus, the phase shift of the wave travel from point *b(x,y)* to point *a(x,y)* should be instead expressed as $e^{-i(\Phi_r-\Phi_{nr})}$, as indicated by the green arrow. If the non-reciprocal phase is negligible, i.e.

$\Phi_{nr} = 0$, the phase shifts are with the same value but opposite signs [154]. If the reciprocal phase is near zero, i.e. zero-index metamaterials [155], the phase shifts are with same value. But generally, due to the existence of both reciprocal phase and non-reciprocal phase, the phase shift for waves respectively coming from point *a(x,y)* and point *b(x,y)* are different. However, all the acoustical coiling metamaterials reported so far only consider the reciprocal phase shift, the non-reciprocal phase properties of coiling metamaterials lack of study.

Here, we introduce the non-reciprocal phase by implementing a background mean flow. The lattice under our study is the square lattice. Figure 3.9 (b) presents the simplified model under our study. The pink dots represent the nodes of our lattice while the black lines denote the transmission paths. Each node is connected by four paths. The real coiling structure is shown in Fig. 3.9 (c). The red part indicates one unit of the lattice with lattice constant $a = 12\sqrt{2}$ cm.

The coiling structure is shown in Fig. 3.10 (a), which corresponds to the simplified model in Fig. 3.9 (b). To apply background flow to the waveguide, a pipe is connected in the third dimension to the waveguide, as shown in Fig. 3.10 (b). A fan is used here to generate constant background flow as shown by the green arrows. Two Helmholtz Resonators are used here to prevent acoustic waves in our desired frequencies traveling through the pipe. Figure 3.10 (c) presents the relation between the non-reciprocal phase shift and the flow Mach number when the frequency is around 3460 Hz. The Mach number here is defined as background flow speed divided by the speed of sound. In our simulation, the background media is air with sound speed $c = 343$ m/s and

density $\rho = 1.2$ kg/m^3. From Fig. 3.10 (c), it is obvious that with very low background flow speed (Mach number less than 0.03), we can get non-reciprocal phase modulation from -π to π.

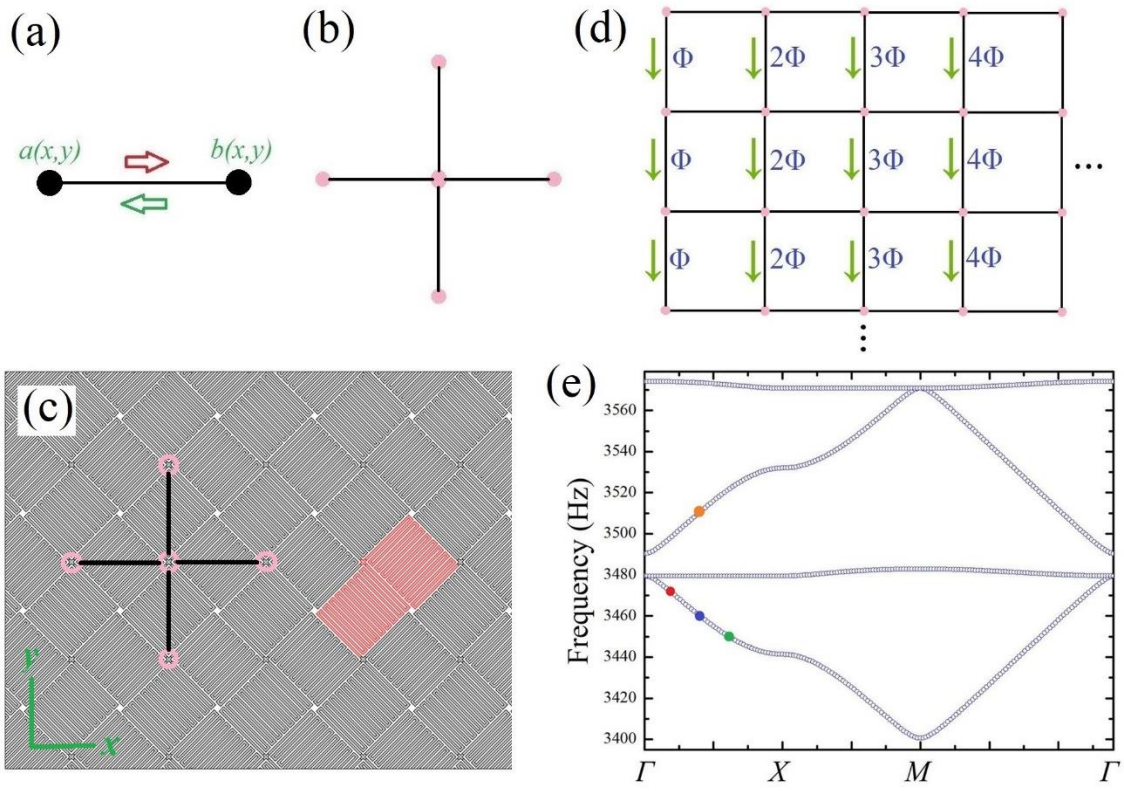

Figure 3.9. System configuration. (a) A wave path connected with two nodes. For waves coming from different directions, the phase shift may be different due to the contribution of non-reciprocal phase shift. (b) Simplified mode under consideration. Each node is connected with four waveguides. (c) The actual structure of our configuration. (d) Non-reciprocal phase modulations applied to our structure. The modulations are only applied to the vertical waveguides and be proportional to the column number. (e) Band diagram of the structure with only reciprocal phase shift being considered.

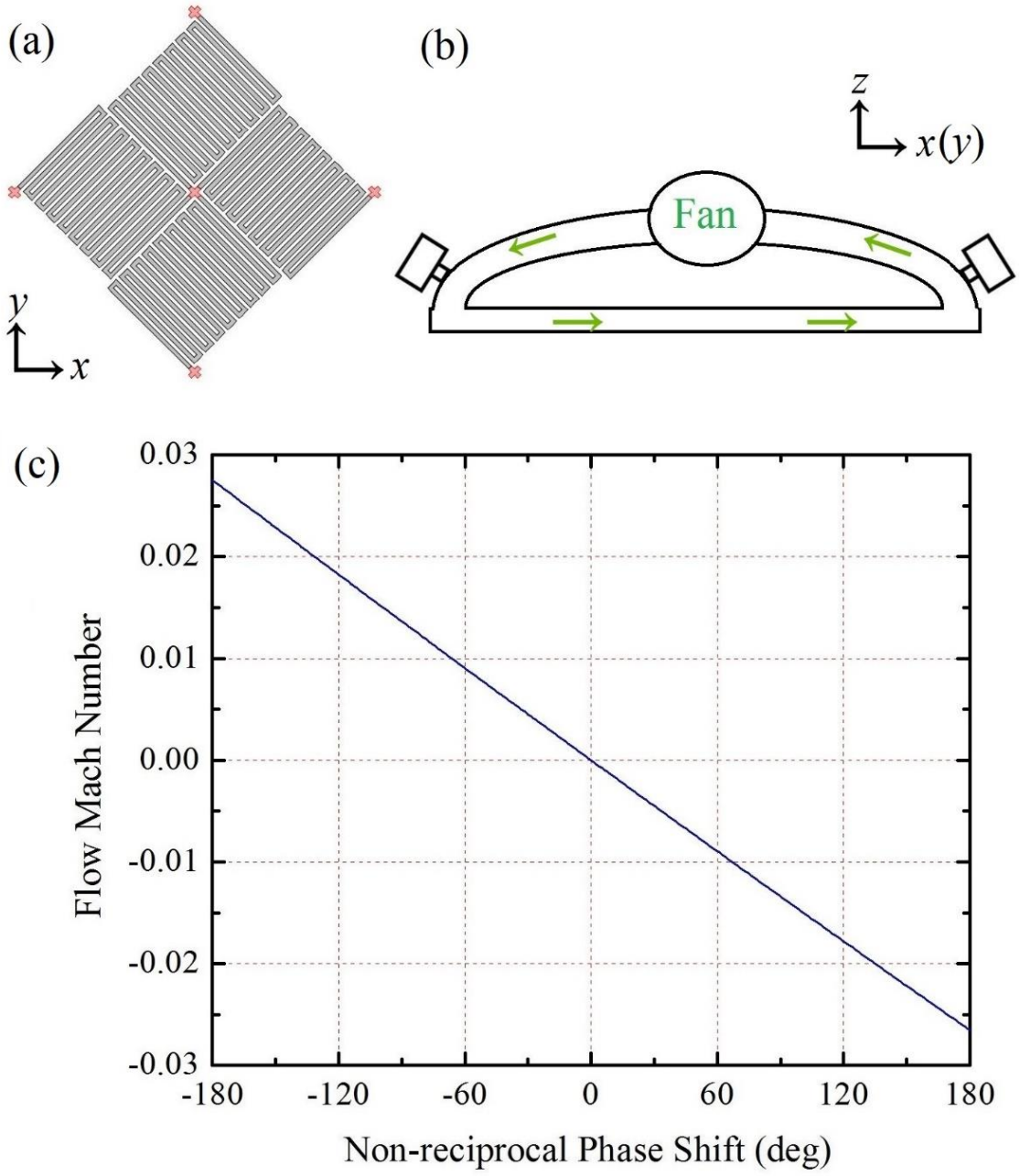

Figure 3.10. Actual configure to realize non-reciprocal phase shift. (a) a four ports network. (b) The configuration to realize the non-reciprocal phase shift by using an extra fan and pipe in the third dimension. (c) The relation between the non-reciprocal phase shift and the background flow speed.

The modulation approach of the non-reciprocal phase shifts Φ_{nr} is shown in Fig. 3.9 (d) with the simplified lattice network topology. The modulation is only applied to the vertical acoustic paths. For each vertical transmission paths within the same column, the non-reciprocal phase shifts are the same. And from left to right, as the column number increase, the modulated non-reciprocal phase shifts for each path increase gradually as $\Phi_{nr} = \Phi$, 2Φ, 3Φ, … In the horizontal transmission paths, however, no background flow is applied, and only reciprocal phase shifts should be considered. In this configuration, the effective magnetic field satisfies:

$$\iint \vec{B}_{eff} \cdot d\vec{S} = \iint \nabla \times \vec{A}_{eff} \cdot d\vec{S} = \oint \vec{A}_{eff} \cdot d\vec{l} = -\Phi \tag{2.86}$$

Here $\vec{A}_{eff}$ is the effective gauge potential for phonons due to the existence of non-reciprocal phase modulations. $\vec{B}_{eff}$ is the effective magnetic field, and we get $\vec{B}_{eff} = -\hat{z}\,\Phi/a^2$. The negative sign indicates that the effective magnetic field is in the *-z-* direction. The properties of the reciprocal phase part are shown in Fig. 3.9 (e), which presents the band diagram of the lattice.

In electrodynamics, for a traveling charged particle with velocity $\vec{v}$, electric quantity *q*, and mass *m*, in the static magnetic field $\vec{B}$, the applied Lorentz force is given by $\vec{F} = q\vec{v} \times \vec{B}$. If we neglect other forces, the particle will move in a circle with radius *R*. Combine the Lorentz force with centripetal force $F = mv^2/R$, we can get the radius of the particle:

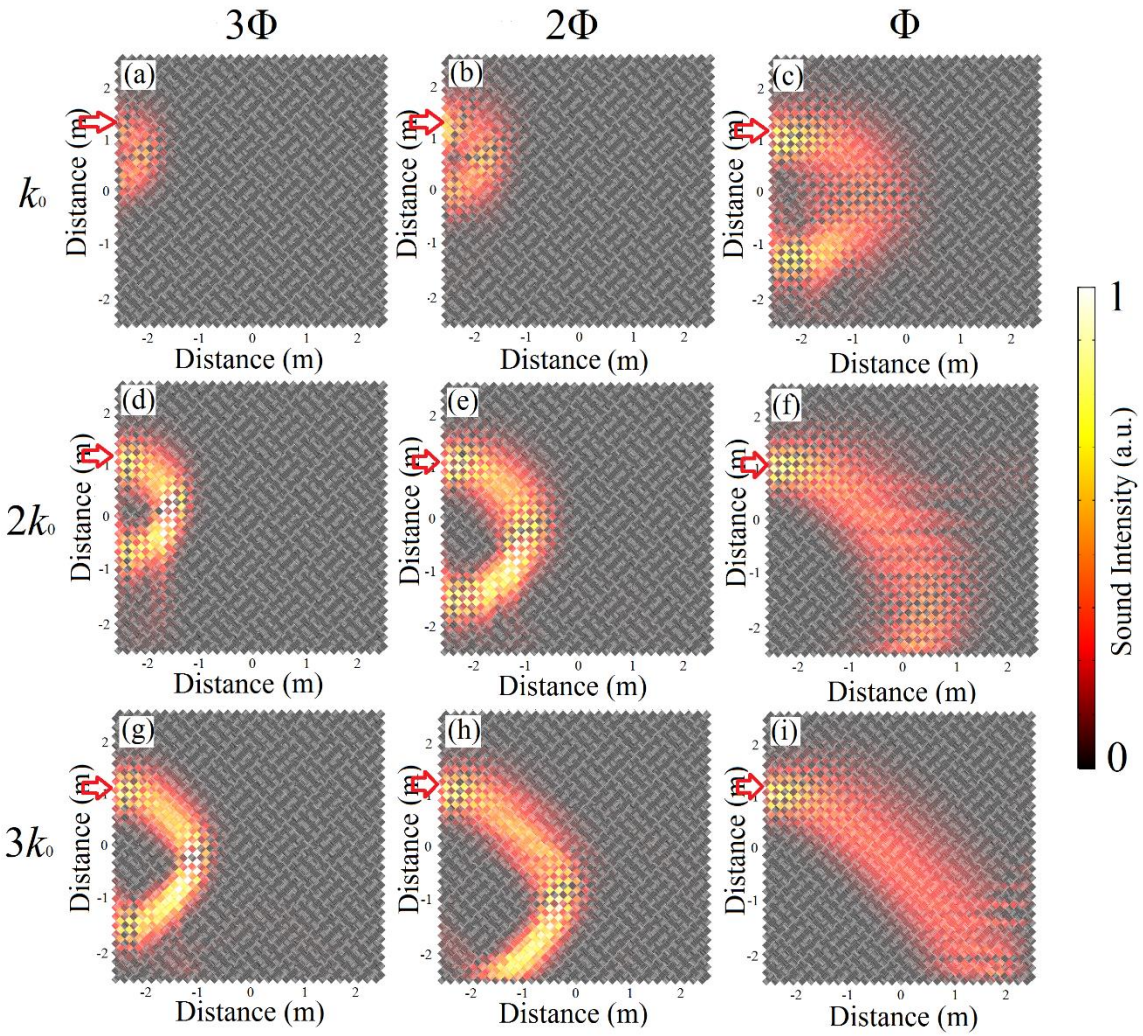

Figure 3.11. Intensity distribution under different modulation and incident momentum. (a), (b) and (c) are with the same momentum k_0, but different non-reciprocal phase shift modulation 3Φ, 2Φ and Φ, respectively. (d), (e) and (f) are with the same momentum $2k_0$, but different non-reciprocal phase shift modulation 3Φ, 2Φ and Φ, respectively. (g), (h) and (i) are with the same momentum $3k_0$, but different non-reciprocal phase shift modulation 3Φ, 2Φ and Φ, respectively. Here $k_0 = 0.21\frac{\pi}{a}$ and Φ=5 deg.

$$R = \frac{mv}{qB} = \frac{k}{qB} \tag{2.87}$$

Here k is the momentum of the particle. Equation (2.87) indicates that the radius of the moving particle in the magnetic field is proportional to its momentum k and inversely proportional to the magnetic field B. Let's see what happens to the phonon flows traveling in our effective magnetic field.

Figure 3.11 presents the sound intensity distribution for acoustic waves traveling in our lattice. The red arrows represent the incident point of the sound. Figures 3.11 (a), (b) and (c) works at the same wavenumber k_0 which corresponds to the red dot in Fig. 3.9 (e), but with different non-reciprocal phase modulation, 3Φ, 2Φ, and Φ, respectively. Figures 3.11 (d), (e) and (f) works at $2k_0$ which corresponds to the blue dot in Fig. 3.9 (e), but with non-reciprocal phase modulation as 3Φ, 2Φ, and Φ, respectively. Figures 3.11 (g), (h) and (i) work at $3k_0$ which corresponds to the green dot in Fig. 3.9 (e), but with non-reciprocal phase modulation as 3Φ, 2Φ, and Φ, respectively. Here $k_0 = 0.21\pi/a$, Φ=5 deg or 0.087 rad. In Fig. 3.11, we can conclude that for a fixed wavenumber k_0 ($2k_0$ or $3k_0$), the radius is inversely proportional to the non-reciprocal shift modulation, which means the radius is inversely proportional to the effective magnetic field. This corresponds to electrodynamics theory in Eq. (2.87). It is also obvious that for a fixed effective magnetic field Φ (2Φ or 3Φ), the radius is proportional to the wavenumber k, which can also be interpreted as wave's momentum. These results also correspond to Eq. (2.87).

One of the important properties for Lorentz force is that, for a charged particle traveling in a homogeneous magnetic field, the chirality of Lorentz force is preserved, no matter where the incident point is. This property is also verified in our system (i.e. if the

phonon flow turn right at one incident point, then the flow will always turn right for any incident points). Figure 3.12 (a) and (b) present the intensity distribution for the acoustic waves travel in the lattice. Both of them are with the same wavenumber $2k_0$, same operation frequency and same negative index as shown by the blue dot in Fig. 3.9 (e) in the main paper. Also, they are with the same non-reciprocal phase modulation Φ=15 deg. The only difference is the incident point. For Fig. 3.12 (a), the incident point is at y=1 m, the acoustic wave turns to the right, and the outgoing point is at y=-0.5 m. When we set the outgoing point in Fig. 3.12 (a) as the incident point in Fig. 3.12 (b) at y=-0.5 m. We find that the sound wave does turn right and leaves at y=-2 m, which corresponds to the characteristics of Lorentz force. We want to emphasize that it is the non-reciprocal phase modulation that breaks the reciprocity of the sound wave so that the sound wave in Fig. 3.12 (b) doesn't travel back along the path in Fig. 3.12 (a).

The direction of momentum, magnetic field and the Lorentz force accord with the right-handed rule. Since the effective magnetic field is in -*z*-direction, one may think that the sound wave should always turn left in our lattice. It may seem strange in Fig. 3.11 that the sound waves turn in the right direction. Take a look at Fig. 3.9 (e) again, we find the three dots (red, blue and green dots) are all located at the curve with a negative slope. Thus, the wave index shown in Fig. 3.11 is negative, which corresponds to negatively charged particles in electrodynamics. For negatively charged particles, the direction of the Lorentz force is opposite to the force applied to the positively charged particle. We thus infer the direction of effective Lorentz force for opposite index acoustic waves should also be in the opposite directions.

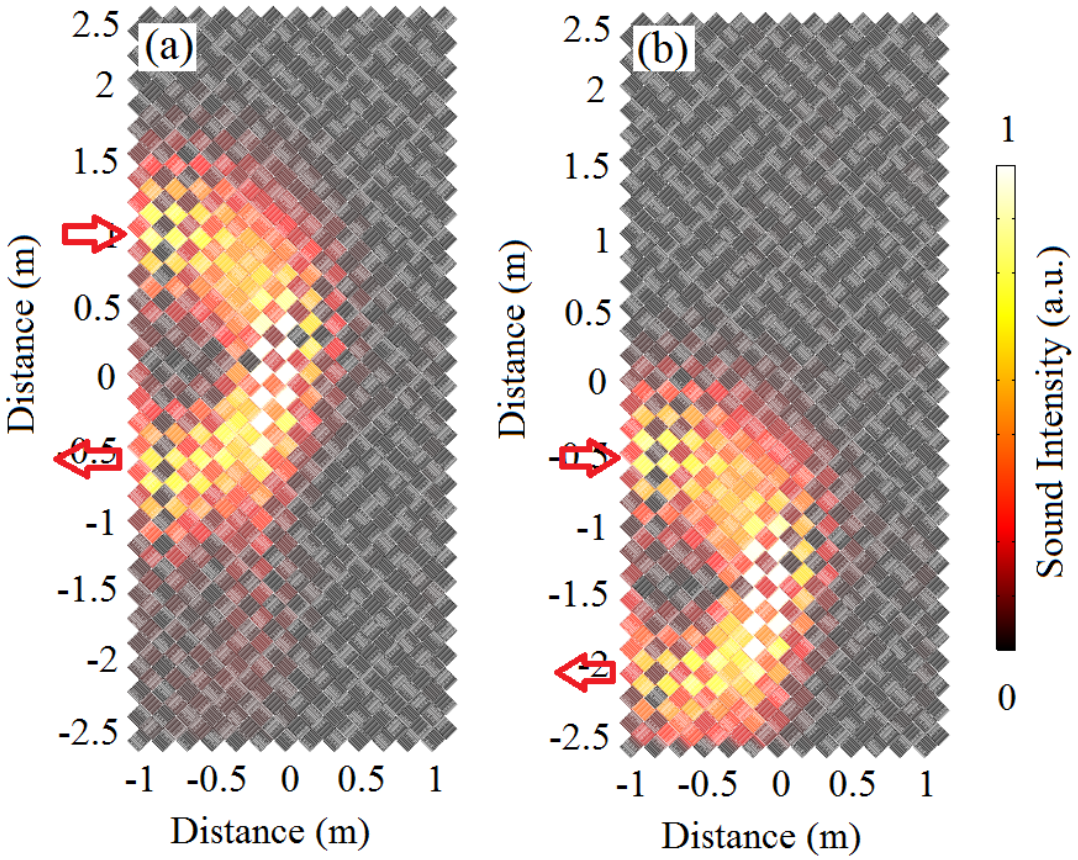

Figure 3.12. Intensity distribution for waves coming from a different location. (a) Intensity profile for wave coming from y=1 m. (b) Intensity profile for wave coming from y=-0.5 m.

To further check the correctness of our assertion, we also present the propagation properties for positive index wave. Figure 3.13 (a) and (b) present the intensity distribution for negative index and positive index incident waves, respectively. The Block wave indexes correspond to the blue dot and the orange dot in Fig. 3.9 (e), respectively. Please note that they are working at different frequencies. Their wavenumbers are with the same value but opposite signs. Fig. 3.13 (a) is with a negative slope (blue dot), and Fig. 3.13 (b) is with a positive slope (orange dot). The non-reciprocal phase shift here is

set to be 15 deg. The red arrows in Fig. 3.13 indicates the incident point of sound waves. For the negative index wave shown in Fig. 3.13 (a), the sound wave turns in the right direction but for positive index incident wave (Fig. 3.13 (b)), the sound wave turns to the left direction. This confirms our assertion that the sign of wave index corresponds to the electric polarity of the charged particles.

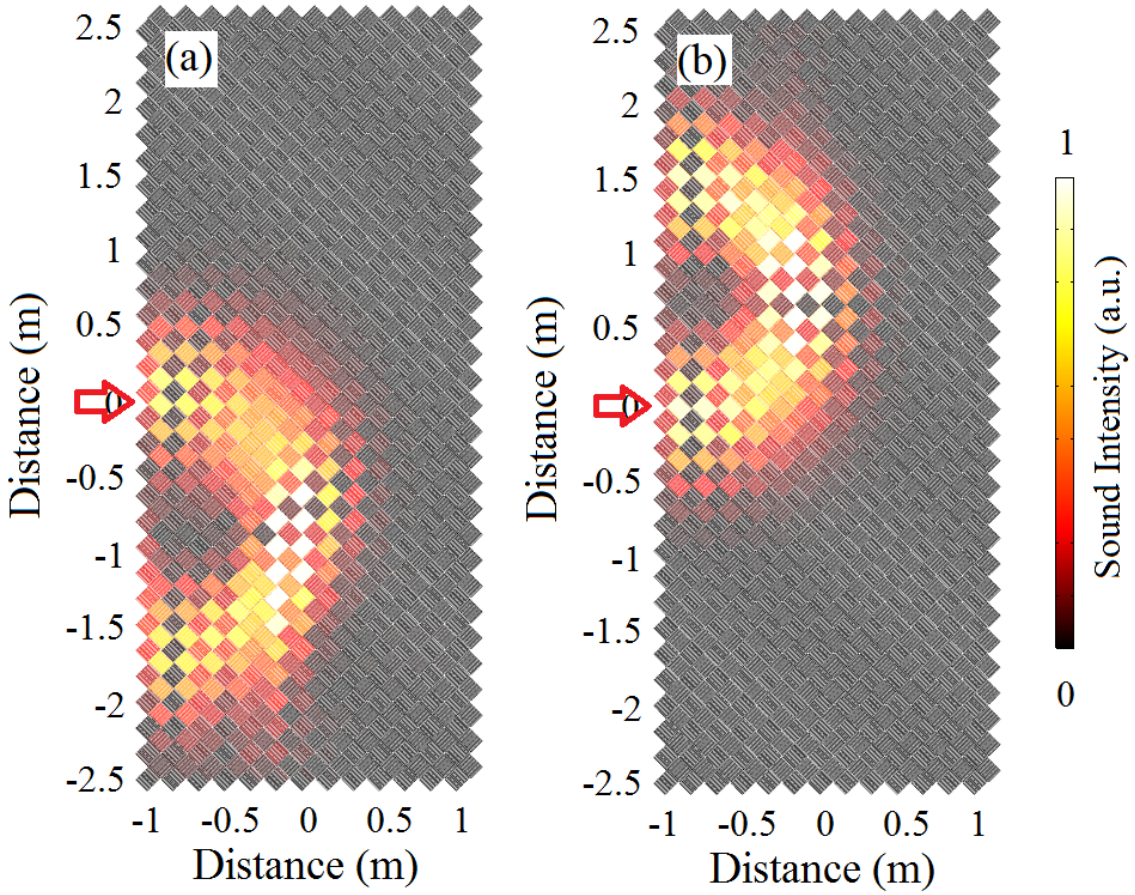

Figure 3.13. Intensity profile for metamaterials with different indexed. (a) Intensity profile for metamaterial with a negative index which corresponds to the negatively charged particles. (b) Intensity profile for metamaterial with a positive index which corresponds to the positively charged particles.

Actually, the radius for acoustic waves with non-reciprocal phase modulation can be calculated as:

$$R = \frac{ka^2}{\Phi} \tag{2.88}$$

If we interpret *k* as momentum, Φ/a^2 as effective magnetic field and electric quantity *q*=1, then Eq. (2.88) is exactly the same as Eq. (2.87). And effective Lorentz force is successfully realized for phonons which is regarded as neutral particles.

In quantum mechanics, quantum Hall effect can be observed in two-dimensional electron system with low temperatures and strong magnetic fields. This unique characteristic can result topological edge state. In the final part of this section, we will show how the effective magnetic field can realize topological acoustic state and disorder robustness one-way edge modes for acoustic waves.

With the same lattice, we modulate the non-reciprocal phase as $\Phi = \frac{2\pi}{3}$. i.e. 0 deg, 120 deg, 240 deg, 360 deg, 480 deg, 600 deg... (Or equivalent to 0 deg, 120 deg, -120 deg, 0 deg, 120 deg, -120 deg…) Thus, the lattice constant in this modulation is $3a = 36\sqrt{2}$ cm. Figure 3.14 (a) presents the lattice and the red color indicates one period of the lattice. Figures 3.14 (b) and (c) present the band structures of the lattice without flow (without non-reciprocal phase shift) and with flow (with non-reciprocal phase shift), respectively. Compared with Fig. 3.14 (b), we find that the bandgap in Fig. 3.14 (c) is fully open for the case with non-reciprocal phase modulation.

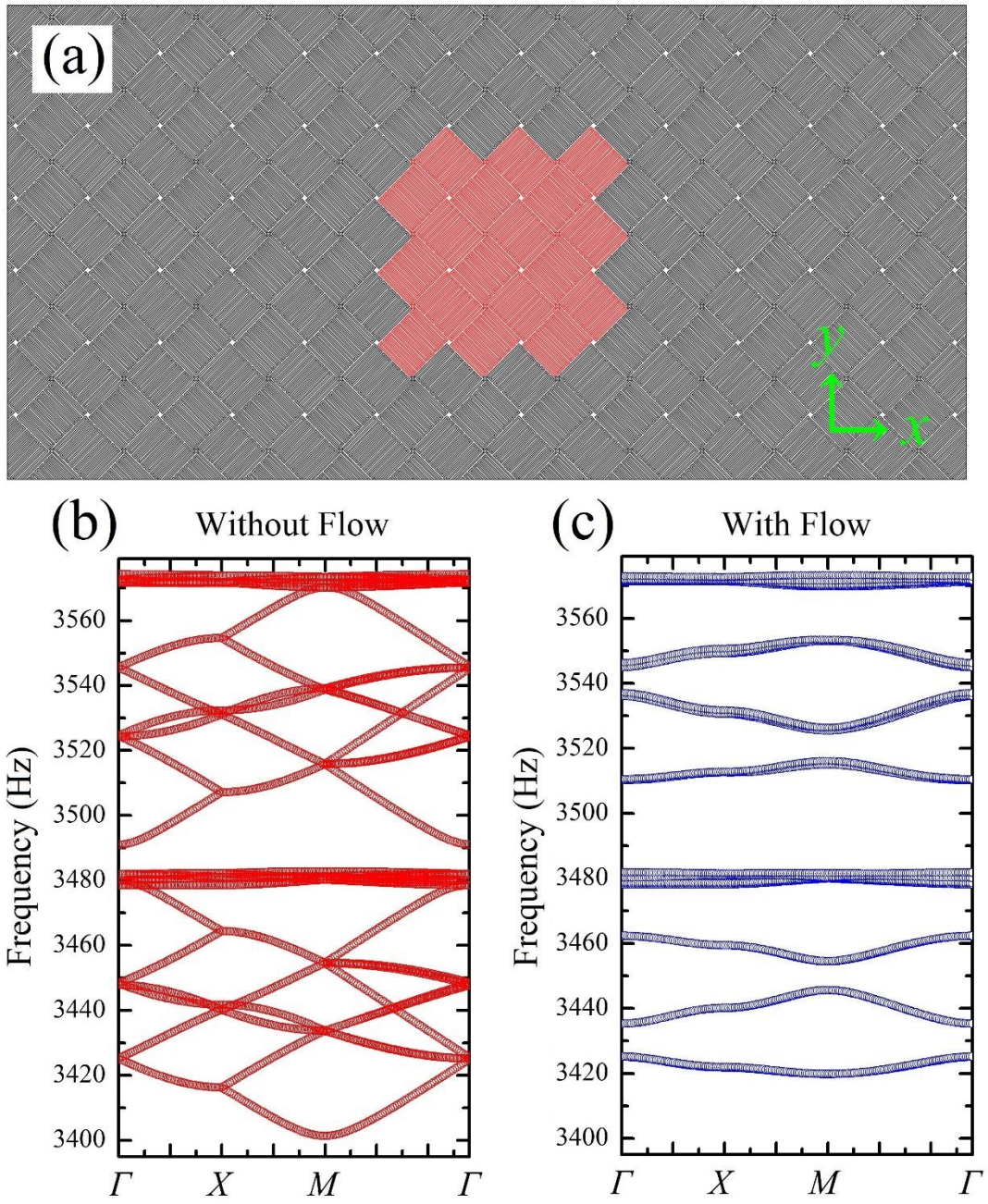

Figure 3.14. Band diagram for non-reciprocal phase modulation under 0 deg, 120 deg, 240 deg. The period here is 3*a*. (a) Actual structure under study. The red color indicates one unit of our structure. (b) and (c) Band diagram for structure without flow and with flow, respectively.

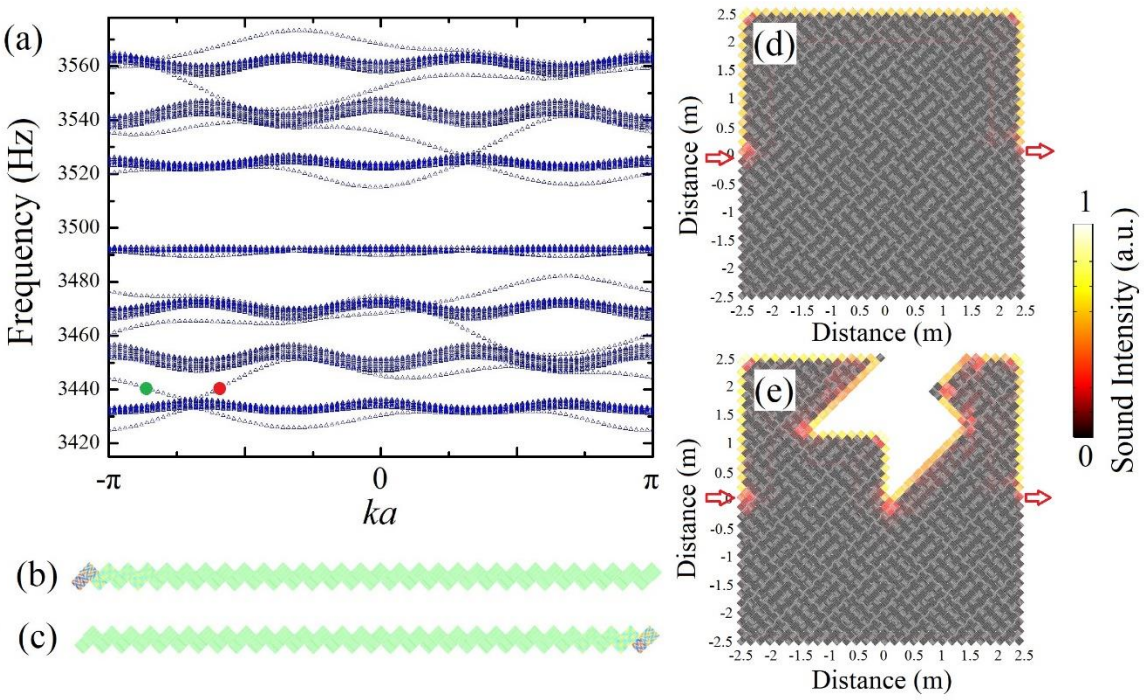

Figure 3.15. Edge modes and topological effects. (a) Band diagram for a stripe geometry with width $30a = 360\sqrt{2}$ cm. (b) The pressure profile corresponds to the red dot in (a). (c) The pressure profile corresponds to the blue dot in (a). (d). Intensity distribution for the lattice without defects and disorders. (e). Intensity distribution for the lattice with defects and disorders.

Now we consider a stripe geometry with width $30a = 360\sqrt{2}$ cm, as shown in Fig. 3.15 (b) and (c). The structure is considered to be finite in *x*-direction while being infinite in the *y*-direction. On both sides, the boundary condition is treated as a hard wall. Figure 3.15 (a) presents the band structure for the stripe. In this frequency range, there are four edge modes located near 3440 Hz, 3460 Hz, 3530 Hz, and 3550 Hz, respectively. Take the edge modes near 3440 for example. Figures 3.15 (b) and (c) present the acoustic

pressure profiles of edge modes correspond to the red and green dots in Fig. 3.15 (a), respectively, which confirm the one-way characteristics of the topological state.

To confirm the robustness of one-way edge modes supported in our structure, we present a full structure simulation of our lattice. Figure 3.15 (d) and (e) show the intensity profiles of the structure without defects and with defects for the acoustic wave incident from left and travel to the right, as indicated by the arrows. Surface edge modes without a backscattering wave confirms the topological robustness of the lattice.

CHAPTER 4: NONLOCAL RESPONSE IN METASURFACES

Nonlocal response in a single inclusion and in bulk metamaterials has been discussed in detail in the previous Chapters. In this Chapter, we will focus on the nonlocal response over metasurfaces.

4.1 Limitations of 1D Local Metasurfaces

Single-layered low-profile artificial surfaces have attracted significant attention recently, due to their capability of manipulating the impinging wave, over a compact design and moderate fabrication complexity compared with bulky metamaterial devices. These metasurfaces have shown interesting prospects for applications in communications, imaging, medical devices, both for electromagnetic and acoustic waves [156]-[160]. Early examples of metasurfaces were mainly based on accurately controlling the local reflection and/or transmission properties of each unit cell, so that the impinging wave can acquire an additional tangential momentum necessary to redirect the incoming energy towards the desired direction, dubbed phase-gradient metasurfaces for electromagnetics [161]-[164] and acoustics [165]-[167]. More recent studies have highlighted inherent efficiency limitations in these designs, since phase-gradient metasurfaces neglect impedance matching constraints and are therefore not able to redirect all incident energy into the desired direction, with a portion of the impinging wave going into unwanted parasitic diffraction orders [168]-[170]. The efficiency decreases rapidly as the steering angle deviates from specular reflection, and hence a clear trade-off exists between efficiency and extreme wavefront transformations in conventional gradient metasurfaces.

More recently, Huygens metasurfaces have been introduced, in which a careful design of the local impedance along the surface and the addition of bianisotropic phenomena have ensured unitary efficiency for arbitrary wave steering, both for electromagnetic [171]-[173] and acoustic [174][175] waves. However, unitary efficiency for reflective metasurfaces still requires the use of active materials, which makes the realization challenging [168]. These findings raise the important question of whether it is possible to realize ideal anomalous wave steering with passive metasurfaces.

In [168]-[170] it was noticed that a single ultrathin surface can generally achieve unitary steering efficiency only provided that, while it is globally lossless, it has an impedance profile with local regions of gain and loss. It was further suggested that one way to create this impedance profile is to induce nonlocality, which may drive energy from one point to another of the surface and address power conservation within a passive design. Simple forms of nonlocality, based on auxiliary evanescent waves [176] and leaky modes [177], have been proposed to address these needs, showing realistic pathways towards efficiencies close to unitary. However, in these cases the metasurface design process is not straightforward and typically a structure optimization is necessary to push the efficiency close to unitary. Bi-anisotropic meta-gratings have also been proposed for electromagnetics [178]-[180] and acoustics [57], which introduce an effective form of nonlocality in each unit cell exploiting resonant scattering and asymmetries. While unitary efficiency can be achieved with these passive structures within a simple implementation, still optimization to suppress the undesired scattering

orders is required in practical designs, and beam steering to arbitrary angles may require complicated unit cell designs.

While acoustic unitary transmission metasurfaces have been recently proposed both in theory [170] and experiments [181] using bi-anisotropic unit cells, acoustic reflection metasurfaces with large efficiency have been reported in a small number of instances, because of the mentioned challenges [182]. Ref. [170] reported 95% reflection efficiency through numerical optimization of the metasurface structure, while Ref. [182] realized 97% reflection relying on a nonplanar surface. In this paper, we explore suitably engineered nonlocality in acoustic unit cells to design unitary reflection acoustic metasurfaces with planar profile. Tailored nonlocal unit cells can accurately control the tunneling of energy between neighboring units, offering a simple design pathway towards efficient reflective acoustic metasurfaces without design limitations and trade-offs. Our analysis proves that the efficiency of our designed metasurfaces can reach unitary levels based on a straightforward design and an easy-to-understand physical mechanism, highlighting the powerful opportunities enabled by engineered nonlocality in metasurface designs for wavefront transformations.

Consider an acoustic plane wave $p_i = p_{i0} e^{ik \sin\theta_i x} e^{-ik\cos\theta_i y}$ traveling in the *x*-*y* plane with incidence angle θ_i, where p_{i0} is the complex amplitude and *k* is the free-space wave number. Here and in the following, the time convention $e^{-i\omega t}$ is omitted for simplicity. We aim to design a planar metasurface lying on the *x*-*z* plane, steering the impinging wavefront in reflection towards the angle θ_r, with pressure $p_r = p_{r0} e^{ik \sin\theta_r x} e^{ik\cos\theta_r y}$, as

shown in Fig. 4.1 (a). For unitary reflection, energy conservation requires $p_{r0} = p_{i0}\sqrt{\cos\theta_i/\cos\theta_r}$. In a conventional gradient metasurface design, each unit cell is composed of locally vibrating elements. The right panel in Fig. 4.1 (a) presents the equivalent circuit model for this geometry, with a single unit cell drawn in the blue dashed frame. The current source represents the net volume velocity flowing into the unit cell due to the contribution of incident and reflected waves. The impedance element $Z = -iX_2$ represents the response of the local element, which is tuned transversely element by element to provide the required phase gradients to steer the wave. This circuit model describes all designs for metasurfaces based on local approaches, no matter whether the realization is based on folded units or Helmholtz resonators. The common drawback of these elements is obvious: each unit cell is separate from each other, which makes transverse energy tunneling between neighboring cells impossible. For passive and lossless elements, X_2 must be real. However, in order to get unitary reflection, the impedance needs to locally satisfy

$$\frac{-iX_2}{\rho_0 c_0} = \frac{\left(\cos\theta_i - \cos\theta_r\right)\cos\left(k\left(\sin\theta_r - \sin\theta_i\right)x\right) + i\left(\cos\theta_i + \cos\theta_r\right)\sin\left(k\left(\sin\theta_r - \sin\theta_i\right)x\right)}{\sqrt{\cos\theta_i\cos\theta_r}\left(\cos\theta_i + \cos\theta_r\right) - 2\cos\theta_i\cos\theta_r\cos\left(k\left(\sin\theta_r - \sin\theta_i\right)x\right)} \tag{3.1}$$

Figure 4.1 (b) presents the impedance distribution for a unitary local metasurface according to Eq. (3.1). Here the incident angle is $\theta_i = 0^\circ$ and the reflection angle is $\theta_r = 75.5^\circ$, and $D = 2\pi/\left(\sin\theta_r - \sin\theta_i\right)$ is the period. From Eq. (3.1) and Fig. 4.1 (b), it is clear that for anomalous reflection ($\theta_i \neq \theta_r$), the required impedance to provide unitary

reflection is necessarily active and/or lossy, (i.e., X_2 needs to generally be a complex number) [168]. Figure 4.1 (c) provides the distribution of Poynting vector in the *y*-direction (I_y) along the metasurface. In part of the unit cell area, the Poynting vector is negative, indicating that the energy is being absorbed by the surface, while in other areas the Poynting vector is positive, indicating that energy is being emitted. Eq. (3.1) essentially forbids unitary reflection with passive and lossless local metasurfaces.

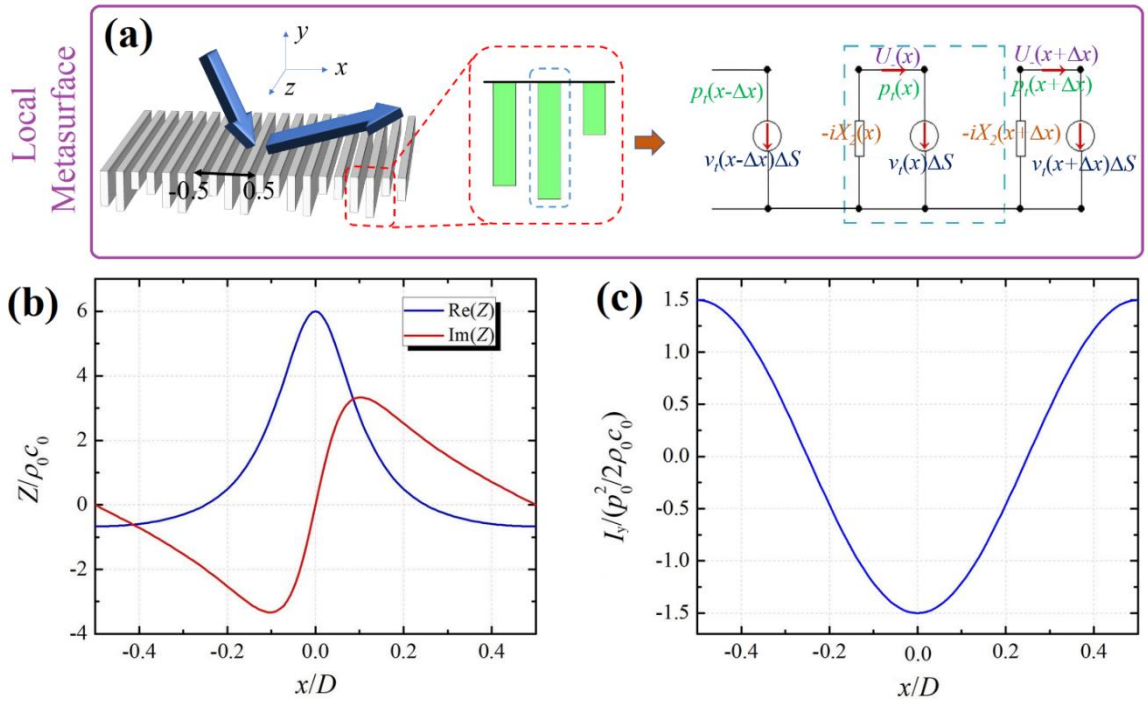

Figure 4.1. (a) Schematic geometry and equivalent circuit model for a local metasurface. The blue dashed frame indicates one unit cell. The current source indicates the net volume velocity flowing into the metasurface, and the lumped impedance element models the local unit cell response. (b) Local impedance profile with the use active and/or lossy units. The required impedance is active in some areas of the unit cell and lossy in others. (c) Distribution of Poynting vector in the *y*-direction along the unit cell.

4.2 1D Nonlocal Metasurface

In order to realize unitary reflection avoiding the use of active and/or lossy unit cells, we propose the use of engineered nonlocality in the unit cells, which therefore support transverse tunneling of energy from some regions of the surface to others, mimicking effective active and lossy unit cells, as shown in Fig. 4.2 (a). In acoustics, we can implement this idea by opening a physical path between neighboring unit cells, supporting flows of pressure or velocity. In the equivalent circuit, this extra path can be modeled as an extra series impedance element $-iX_1$ connecting transversely neighboring unit cells, as shown in the right panel of Fig. 4.2 (a). Our goal is to use only passive elements with engineered nonlocality to realize unitary reflection by energy tunneling, therefore X_1 and X_2 must be real.

According to Fig. 4.2 (a), the mass conversation law and impedance relation for $-iX_1$ and $-iX_2$ can be expressed as

$$v_{-}(x)w\Delta z + v_n(x)\Delta x\Delta z = v_{+}(x)w\Delta z \tag{3.2}$$

$$p_t(x) = p_t(x+\Delta x) - iX_1(x)v_{+}(x)w\Delta z \tag{3.3}$$

$$\frac{p_t(x)}{-iX_2(x)} = v_{+}(x-\Delta x)w\Delta z - v_{-}(x)w\Delta z \tag{3.4}$$

Substituting Eq. (3.2) into Eq. (3.4), we get

$$\frac{p_t(x)}{i\Delta x\Delta z X_2(x)} + v_n(x) = w\frac{\partial v_{+}(x)}{\partial x} \tag{3.5}$$

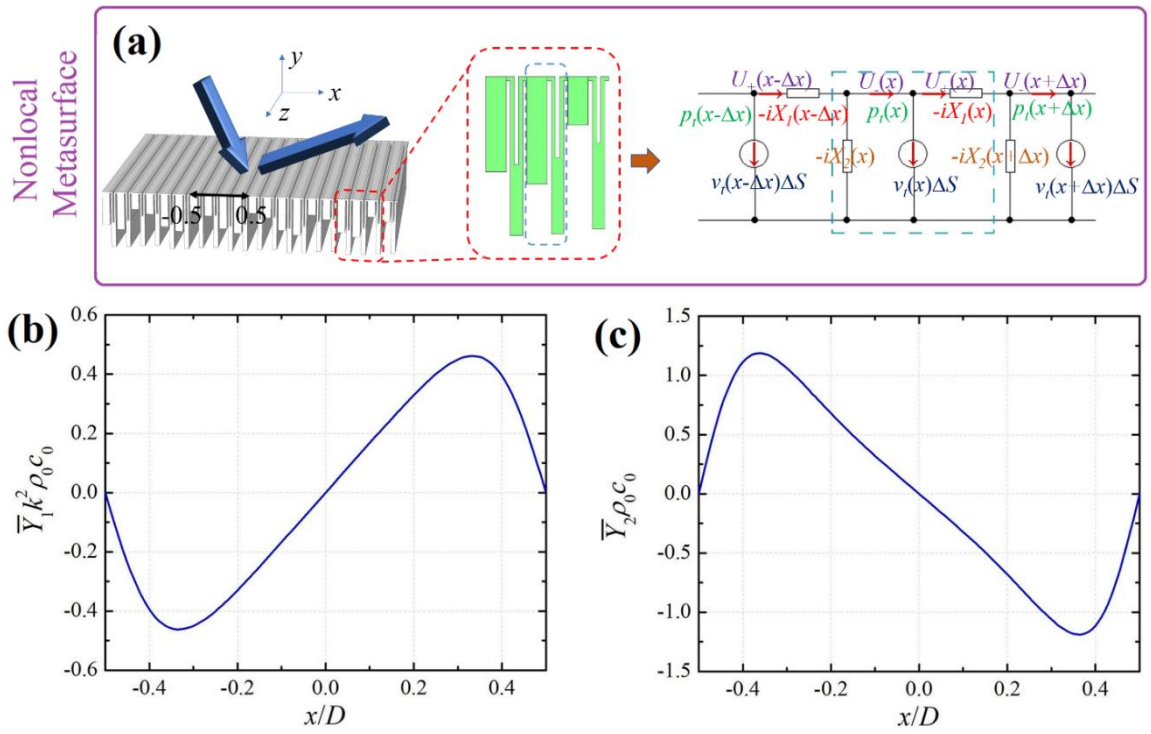

Figure 4.2. (a) Schematic geometry and its equivalent circuit model for the proposed nonlocal metasurface. The equivalent circuit model introduces an extra transverse path connecting neighboring elements, and thus makes the impedance nonlocal. Energy tunnels through this path, so that unitary efficiency can be achieved with passive lossless elements. (b) Distribution of the effective series admittance $\overline{Y}_1$ to realize unitary reflection. (c) Distribution of the effective shunt admittance $\overline{Y}_2$.

Set $\overline{Y}_2(x) = \dfrac{1}{\Delta x \Delta z X_2(x)}$, Eq. (3.5) is changed to

$$-ip_t(x)\overline{Y}_2(x) + v_n(x) = w\frac{\partial v_+(x)}{\partial x} \tag{3.6}$$

From Eq. (3.3), we get

$$\frac{\partial p_t(x)}{\partial x} = i\frac{X_1(x)\Delta z}{\Delta x} v_+(x) w \tag{3.7}$$

Set $\bar{Y}_1(x) = \dfrac{\Delta x}{X_1(x)\Delta z}$, Eq. (3.7) becomes

$$-i\bar{Y}_1(x)\frac{\partial p_t(x)}{\partial x} = v_+(x) w \tag{3.8}$$

And after taking the derivative in *x*, we get

$$w\frac{\partial v_+(x)}{\partial x} = -i\frac{\partial \bar{Y}_1(x)}{\partial x}\frac{\partial p_t(x)}{\partial x} - i\bar{Y}_1(x)\frac{\partial^2 p_t(x)}{\partial^2 x} \tag{3.9}$$

Replacing Eq. (3.9) into Eq. (3.6):

$$p_t(x)\bar{Y}_2(x) = \frac{\partial p_t(x)}{\partial x}\frac{\partial \bar{Y}_1(x)}{\partial x} + \frac{\partial^2 p_t(x)}{\partial^2 x}\bar{Y}_1(x) - iv_n(x) \tag{3.10}$$

Note that $\dfrac{\partial p_t(x)}{\partial x} = i\omega\rho_0 v_x(x)$. Then we are able to get the pressure expression along the metasurface from Eq. (3.10):

$$p_t(x) = -\frac{i}{\bar{Y}_2(x)} v_n(x) + \frac{i\omega\rho_0}{\bar{Y}_2(x)}\frac{\partial\left[\bar{Y}_1(x) v_x(x)\right]}{\partial x} \tag{3.11}$$

Here, $\bar{Y}_1 = \dfrac{\Delta x}{X_1 \Delta z}$ and $\bar{Y}_2 = \dfrac{1}{\Delta x \Delta z X_2}$ are effective admittance elements, which are real because X_1 and X_2 are real in the lossless limit. In the local scenario, $X_1 \to \infty$ ($Y_1 \to 0$), the pressure along the surface is only proportion to the normal velocity ($p_t = -iv_n / \bar{Y}_2$), thus the metasurface converges to the conventional local surface shown in Fig. 4.1 (a). The ratio of local pressure and velocity, i.e., the surface impedance, can thus

be calculated as $Z = -i/\bar{Y}_2$. When nonlocality is considered, however, the surface pressure is no longer a monotropic function of the normal velocity v_n, but also a function of tangential velocity v_x, as shown in Eq. (3.11). Hence, we can calculate the Poynting vector along *y* as

$$I_y = \frac{1}{2}\mathrm{Re}\left(p_t v_n^*\right) = -\frac{|v_n|^2}{2}\mathrm{Re}\left(\frac{i}{\bar{Y}_2}\right) + \frac{1}{2}\mathrm{Re}\left(\frac{i\omega\rho_0}{\bar{Y}_2}\frac{\partial\left(\bar{Y}_1 v_x\right)}{\partial x}v_n^*\right) \tag{3.12}$$

The first term in this expression stems from the local interactions, while the second term is due to the transverse energy tunneling between unit cells. For local metasurfaces ($Y_1 \to 0$), passive and lossless units (Y_2 is real), $I_y = 0$ is always satisfied. However, for nonlocal passive and lossless metasurface (both Y_1 and Y_2 real), even though the first term of Eq. (3.12) is zero, the second term is nonzero, indicating an effective 'absorption' or 'radiation' of energy locally along the metasurface, based on nonlocal effects.

4.3 Beam Steering

For beam steering, given incident and reflection angles, we can evaluate the required total pressure field p_t, tangential velocity v_x and normal velocity field v_n on the metasurface. By further requiring a lossless response, we could find the expression for the effective admittances $\bar{Y}_1$ and $\bar{Y}_2$ to realize unitary reflection with a passive nonlocal metasurface in the following approach.

Substituting the expressions of total pressure field along the metasurface $p_t = p_0 e^{ik\sin\theta_i x} + p_0\sqrt{\cos\theta_i/\cos\theta_r}\,e^{ik\sin\theta_r x}$, total tangential velocity $v_x(x) = \frac{1}{i\omega\rho_0}\frac{\partial p_t(x)}{\partial x}$ and the total normal velocity field along the metasurface $v_n = \left(p_0\cos\theta_i/\rho_0 c_0\right)e^{ik\sin\theta_i x} - \left(p_0\cos\theta_r/\rho_0 c_0\right)\sqrt{\cos\theta_i/\cos\theta_r}\,e^{ik\sin\theta_r x}$ into Eq. (3.11), we get

$$\left(1+\sqrt{\frac{\cos\theta_i}{\cos\theta_r}}e^{ik(\sin\theta_r-\sin\theta_i)x}\right)\bar{Y}_2 + k^2\left(\sin^2\theta_i + \sin^2\theta_r\sqrt{\frac{\cos\theta_i}{\cos\theta_r}}e^{ik(\sin\theta_r-\sin\theta_i)x}\right)\bar{Y}_1$$

$$= ik\left(\sin\theta_i + \sin\theta_r\sqrt{\frac{\cos\theta_i}{\cos\theta_r}}e^{ik(\sin\theta_r-\sin\theta_i)x}\right)\frac{\partial\bar{Y}_1}{\partial x} + i\frac{\cos\theta_r}{\rho_0 c_0}\sqrt{\frac{\cos\theta_i}{\cos\theta_r}}e^{ik(\sin\theta_r-\sin\theta_i)x} - i\frac{\cos\theta_i}{\rho_0 c_0}$$

(3.13)

Note that $\bar{Y}_1$ and $\bar{Y}_2$ are real, due to the use of passive lossless units, hence we can separate Eq. (3.13) into real part and imaginary part, respectively:

$$\left(1+\sqrt{\frac{\cos\theta_i}{\cos\theta_r}}\cos\left[k(\sin\theta_r-\sin\theta_i)x\right]\right)\bar{Y}_2 + k^2\left(\sin^2\theta_i + \sin^2\theta_r\sqrt{\frac{\cos\theta_i}{\cos\theta_r}}\cos\left[k(\sin\theta_r-\sin\theta_i)x\right]\right)\bar{Y}_1$$

$$= -k\sin\theta_r\sqrt{\frac{\cos\theta_i}{\cos\theta_r}}\sin\left[k(\sin\theta_r-\sin\theta_i)x\right]\frac{\partial\bar{Y}_1}{\partial x} - \frac{\cos\theta_r}{\rho_0 c_0}\sqrt{\frac{\cos\theta_i}{\cos\theta_r}}\sin\left[k(\sin\theta_r-\sin\theta_i)x\right]$$

(3.14)

$$\sqrt{\frac{\cos\theta_i}{\cos\theta_r}}\sin\left[k(\sin\theta_r-\sin\theta_i)x\right]\bar{Y}_2 + k^2\sin^2\theta_r\sqrt{\frac{\cos\theta_i}{\cos\theta_r}}\sin\left[k(\sin\theta_r-\sin\theta_i)x\right]\bar{Y}_1 =$$

$$k\left(\sin\theta_i + \sin\theta_r\sqrt{\frac{\cos\theta_i}{\cos\theta_r}}\cos\left[k(\sin\theta_r-\sin\theta_i)x\right]\right)\frac{\partial\bar{Y}_1}{\partial x} + \frac{\cos\theta_r}{\rho_0 c_0}\sqrt{\frac{\cos\theta_i}{\cos\theta_r}}\cos\left[k(\sin\theta_r-\sin\theta_i)x\right] - \frac{\cos\theta_i}{\rho_0 c_0}$$

(3.15)

By solving these two differential equations, we are able to uniquely determine the profile of $\bar{Y}_1$ and $\bar{Y}_2$ for arbitrary incident and reflection angles as

$$\bar{Y}_1 k^2 \rho_0 c_0 = -\frac{\sin[k(\sin\theta_i - \sin\theta_r)x]}{\left(\cos\theta_i + \cos\theta_r\right)\cos[k(\sin\theta_i - \sin\theta_r)x] + \dfrac{\cos\left(\theta_i + \theta_r\right)+1}{\sqrt{\cos\theta_i \cos\theta_r}}} \tag{3.16}$$

$$\bar{Y}_2 \rho_0 c_0 = \frac{\sqrt{\cos\theta_i \cos\theta_r}\,\sin\left[k(\sin\theta_i - \sin\theta_r)x\right]}{\left(1+\sqrt{\dfrac{\cos\theta_i}{\cos\theta_r}}\cos\left[k(\sin\theta_i - \sin\theta_r)x\right]\right)}$$

$$+\frac{\sin[k(\sin\theta_i - \sin\theta_r)x]\left(\sin^2\theta_i + \sin^2\theta_r\sqrt{\dfrac{\cos\theta_i}{\cos\theta_r}}\cos\left[k(\sin\theta_i - \sin\theta_r)x\right]\right)}{\left(1+\sqrt{\dfrac{\cos\theta_i}{\cos\theta_r}}\cos\left[k(\sin\theta_i - \sin\theta_r)x\right]\right)\left[\left(\cos\theta_i + \cos\theta_r\right)\cos[k(\sin\theta_i - \sin\theta_r)x] + \dfrac{\cos\left(\theta_i + \theta_r\right)+1}{\sqrt{\cos\theta_i \cos\theta_r}}\right]}$$

$$-\frac{\sin\theta_r\sqrt{\dfrac{\cos\theta_i}{\cos\theta_r}}\sin\left[k(\sin\theta_i - \sin\theta_r)x\right](\sin\theta_i - \sin\theta_r)\left[\cos\theta_i + \cos\theta_r + \dfrac{\cos\left(\theta_i + \theta_r\right)+1}{\sqrt{\cos\theta_i \cos\theta_r}}\cos[k(\sin\theta_i - \sin\theta_r)x]\right]}{\left(1+\sqrt{\dfrac{\cos\theta_i}{\cos\theta_r}}\cos\left[k(\sin\theta_i - \sin\theta_r)x\right]\right)\left[\left(\cos\theta_i + \cos\theta_r\right)\cos[k(\sin\theta_i - \sin\theta_r)x] + \dfrac{\cos\left(\theta_i + \theta_r\right)+1}{\sqrt{\cos\theta_i \cos\theta_r}}\right]^2} \tag{3.17}$$

Besides beam steering, this design approach can be generalized to arbitrary wave transformations, by plugging in the equations the incident and desired reflected field distributions. By engineering the local and nonlocal impedance along the surface it is possible to transform with unitary efficiency and large flexibility the impinging sound wave in arbitrary scenarios.

As an example, we assume that the incident angle is normal to the metasurface $\theta_i = 0^\circ$ and the desired reflection angle is $\theta_r = 75.5^\circ$ ($\cos\theta_r = \frac{1}{4}$, $\sin\theta_r = \frac{\sqrt{15}}{4}$). The effective admittance can be expressed as

$$\bar{Y}_1 = \frac{4\sin\left(\sin\theta_r kx\right)}{5k^2\rho_0 c_0\left[2+\cos\left(\sin\theta_r kx\right)\right]} \tag{3.18}$$

$$\bar{Y}_2 = -\frac{\left[7+2\cos\left(\sin\theta_r kx\right)\right]\sin\left(\sin\theta_r kx\right)}{2\rho_0 c_0\left[2+\cos\left(\sin\theta_r kx\right)\right]^2} \tag{3.19}$$

Figures 4.2 (b) and (c) show the profile of the required $\bar{Y}_1$ and $\bar{Y}_2$ to achieve unitary efficiency. In the left half period, the effective admittances are respectively negative and positive, and in the right half period, they reverse signs. By replacing Eq. (3.18) and (3.19) into Eq. (3.12), we find the Poynting vector profile, which coincides with the one shown in Fig. 4.1 (c), confirming the ideal response of the surface, and its effective absorption and re-radiation across each unit cell, which is enabled in a locally lossless metasurface based on nonlocal phenomena.

In order to explore a practical realization of these concepts, we need to discretize the profile of the required admittances, and determine an acoustic micro-structure that synthesizes the nonlocal response. While the profile of $\bar{Y}_2$ has different signs in different locations, the corresponding micro-structure can be designed with folded structures or Helmholtz resonators, consistent with previous approaches to local metasurfaces. Here we choose impedance tubes with different lengths, as shown in the inset of Fig. 4.2 (a).

The design of the admittance $\bar{Y}_1$ is trickier, especially when the profile is negative in some portion of each unit cell. While membranes are the most common tool to provide compact capacitive responses for sound, the required pretension process of each membrane makes the realization of arrays of them for metasurfaces difficult to reproduce and scale up. For this reason, we aim at using impedance tubes, which ensure stability and accuracy of implementation. However, as shown in the equivalent circuit of Fig. 4.2 (a), the volume velocity at both sides of $\bar{Y}_1$ should be identical, but the pressure across it should not be zero. Thus, a single tube cannot realize our goal. In our realization, we use two narrow tubes connecting a wide tube to realize the required additional tunneling path, as shown in the inset of Fig. 4.2 (a). By accurate design, the middle tube can store some of the volume velocity, which ensures that the volume velocity at both sides of $\bar{Y}_1$ is identical. This tube design can therefore synthesize either a capacitive or inductive response by changing the tube length

The design structure of the nonlocal metasurface is shown in Fig. 4.3 (c). In each unit cell, we have one left impedance tube and one right cascading tube. The left impedance tube corresponds to the traditional metasurface design and the cascading tube connecting the neighboring elements is the extra path that allows transverse energy tunneling.

For the traditional impedance with length l_0, its corresponding impedance expression is

$$\bar{Y}_2 \rho_0 c_0 = -\tan k l_0 \tag{3.20}$$

Therefore, for a given admittance $\bar{Y}_2$, the desired length l_0 can be chosen as

$$l_0 = \frac{\pi - \arctan\left(\bar{Y}_2 \rho_0 c_0\right)}{k} \tag{3.21}$$

The cascading tube contains two small tubes with identical width w and length h and one large tube with width αw and length d. Here α is the proportionality coefficient. Suppose the pressure field and velocity field in the left small tube to be $p_L = Ae^{iky} + Be^{-iky}$ and $v_L = \left(Ae^{iky} - Be^{-iky}\right)/\rho_0 c_0$, respectively. And the pressure field and velocity field in the right small tube to be: $p_R = Ce^{iky}$ and $v_R = Ce^{iky}/\rho_0 c_0$, respectively. If we set the location of connection point of the small and large tubes to be y=0, we can also get the pressure and velocity field for the large tube: $p_{Large} = Ee^{iky} + Ee^{-2ikd}e^{-iky}$ and $v_{Large} = \left(Ee^{iky} - Ee^{-2ikd}e^{-iky}\right)/\rho_0 c_0$. At the connection point y=0, the pressure should be continuous:

$$A + B = C = E + Ee^{-2ikd} \tag{3.22}$$

At the same point, the mass conservation law requires

$$w\frac{A-B}{\rho_0 c_0} + w\frac{C}{\rho_0 c_0} = \alpha w\frac{E - Ee^{-2ikd}}{\rho_0 c_0} \tag{3.23}$$

In addition, the input and outgoing velocities at the left and right small tube need to be identical:

$$\frac{Ae^{ikh} - Be^{-ikh}}{\rho_0 c_0} = -\frac{Ce^{ikh}}{\rho_0 c_0} \tag{3.24}$$

The impedance relation for $\bar{Y}_1$ requires

$$Ae^{ikh} + Be^{-ikh} = Ce^{ikh} - i\frac{w\Delta x}{\bar{Y}_1}\left(\frac{Ae^{iky} - Be^{-iky}}{\rho_0 c_0}\right) \tag{3.25}$$

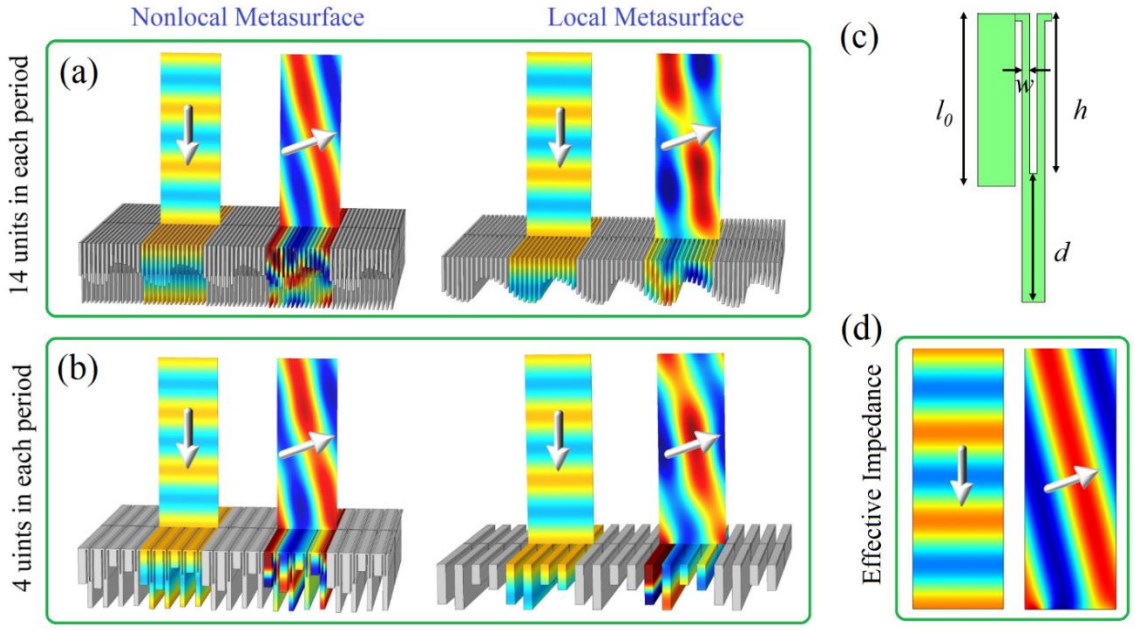

Figure 4.3. (a) Discretized reflection metasurface with realistic implementation using 14 units in each period. The left panel presents the incident and reflection field for a nonlocal metasurface with connecting paths. The right panel presents the corresponding field for a local metasurface without transverse connections. For the nonlocal metasurface with 14 units in each period, the efficiency reaches 99.6%. (b) Reflection metasurface with 4 elements in each unit cell. The left and right panels present the incident wave and the reflection field for nonlocal and for local metasurface, respectively. For the nonlocal metasurface with 4 units in each period, the efficiency reaches 96.4%. (c) Schematic geometry of each unit. (d) Incident and reflected wave calculated through effective impedance theory.

Combining Eqs. (3.22)-(3.25), we can get the required length of h and d for any admittance $\bar{Y}_1$ as

$$d = \frac{\pi + \arctan\left(\dfrac{2\alpha w \Delta x \rho_0 c_0 \bar{Y}_1}{\left(w\Delta x\right)^2 - \left(\alpha \rho_0 c_0 \bar{Y}_1\right)^2} \right)}{2k} \tag{3.26}$$

$$h = \frac{\pi + \arctan\left(\dfrac{4 w \Delta x \rho_0 c_0 \bar{Y}_1}{\left(2\rho_0 c_0 \bar{Y}_1\right)^2 - \left(w\Delta x\right)^2} \right)}{2k} \tag{3.27}$$

We first discretize the required admittance profile into fourteen segments for each period. For a normally incident plane wave with desired 75.5 deg reflection angle, an efficiency of 99.6% is obtained, as shown in the left panel in Fig. 4.3 (a). The numerical simulation is calculated by the commercial finite element method software COMSOL Multiphysics. The reflection pressure field is twice stronger than the incident field, confirming unitary anomalous reflection of our metasurface. As a comparison, we remove the tunneling path, suppressing the engineered nonlocal response, and the reflection efficiency drastically decreases, while strong parasitic waves arise, as seen in the right panel in Fig. 4.3 (a). This comparison confirms the effectiveness of our nonlocal metasurface design. Fig. 4.3 (c) presents the schematic geometry of each unit. Here w=0.5 mm and α=3. Other design parameters can be found in Table I. We also provided the incident and reflected wave calculated by effective impedance theory shown in Fig. 4.3 (d) for comparison.

Fig. 4.3 (b) presents the same design with only four discrete segments in each period, i.e., a sparse discretization of the required nonlocal impedance profile. Here w=1.75 mm and α=3. Other design parameters can be found in Table II. The reflection

field for the nonlocal metasurface and for the associated local profile are shown in the left and right panels, respectively. In this case, the nonlocal efficiency is still very large, 96.4%, while the local metasurface has a much poorer performance, proving the robustness of nonlocal metasurfaces to coarse discretization.

(mm)	1	2	3	4	5	6	7
l_0	36.8	40.9	43.8	45.8	46.8	46.9	43.2
d	32.7	33.6	33.7	33.8	33.8	33.8	33.6
h	35.2	33.9	33.6	33.5	33.5	33.5	33.9
	8	9	10	11	12	13	14
l_0	25.6	21.9	22.0	23.0	25.0	27.9	32.0
d	34.5	34.2	34.2	34.2	34.3	34.4	35.3
h	32.6	32.9	33.0	32.9	32.8	32.6	31.3

Table 4.1. Detailed design parameters of each unit shown in Fig. 4.3 (a).

We have also explored the effect of realistic loss for the design shown in Fig. 4.3 (b) by taking the viscous effects into consideration. The simulation including realistic viscous and thermal loss is performed through COMSOL Multiphysics Thermoviscous Acoustics Model. In our simulation, we choose air as the background medium and set thermal conductivity $k = 0.025768\, W/(m \cdot K)$, dynamic viscosity $\mu_B = 1.814 \times 10^{-5}\, Pa \cdot s$, bulk viscosity $\mu_B = 1.0884 \times 10^{-5}\, Pa \cdot s$. The boundary condition

is set to be no slip for the mechanical condition and isothermal for the thermal condition. The results are shown in Fig. 4.4. While the efficiency of beam steering is slightly deteriorated because of the small width of the considered channels, we envision a trade-off between channel width to impart the nonlocal effect (and hence metasurface thickness), and overall efficiency of wavefront transformation.

(mm)	1	2	3	4
l_0	40.5	45.8	20.5	25.8
d	30.1	32.9	36.6	39.0
h	37.6	34.7	28.2	25.1

Table 4.2. Detailed design parameters of each unit shown in Fig. 4.3 (b).

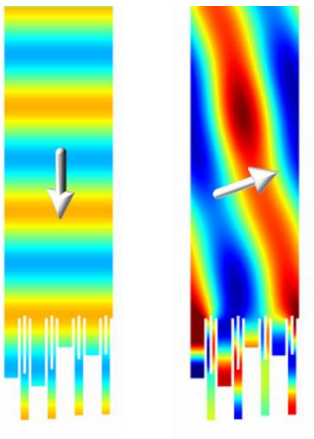

Figure 4.4. Simulation result for the design shown in Fig. 4.3 (b) by taking viscous effects and thermal loss into consideration.

4.4 Acoustic Anisotropic Metasurfaces

The recent progress in metamaterials research has enabled many exciting opportunities for wave manipulation and its applications, resulting in the discovery of novel devices, such as cloaks [32]-[33], hyperlenses [183]-[184], and hyperbolic metamaterials [185]-[191], among several others. These concepts were firstly proposed in electromagnetics, and later extended to acoustics [16],[48]-[49],[192] due to the analogies between the two wave phenomena. In the design and realization of these metamaterial devices, a key requirement is the implementation of extremely anisotropic material properties. Due to the vector nature of electromagnetic waves, both permittivity and permeability can be anisotropic. However, the longitudinal nature of sound waves in fluid, and the associated symmetry constraints make the opportunities more limited in acoustics. Although anisotropy is not a common property of fluids, the realization of anisotropic mass density has been explored in recent years [54][55][192], and its implementation has been applied to the design of various acoustic metamaterials, especially in the framework of transformation acoustics [48][49][193][194]. Although anisotropic stiffness is possible [195][196], there is no implementation of anisotropic bulk modulus for fluid acoustics. The reason for this missed opportunity lies in the symmetries obeyed by the equations governing sound propagation in fluids: the momentum equation $\nabla p + \rho_{eff}\, \partial \vec{v} / \partial t = 0$ and the mass conservation equation $\partial p / \partial t + B_{eff} \nabla \cdot \vec{v} = 0$. Here p, $\vec{v}$, ρ_{eff} and B_{eff} represent the acoustic pressure, particle velocity, effective density, and bulk modulus, respectively. Since both ∇p and

$\partial\vec{v}/\partial t$ are vectors, a tensorial effective density in the momentum equation can be expected, yielding $\nabla p + \bar{\bar{\rho}}_{eff} \cdot \partial\vec{v}/\partial t = 0$, which simply implies that the three components of the equation are generally coupled together, and the response changes for different velocity directions. The mass conservation equation, however, is scalar, hence the effective bulk modulus cannot take a tensorial form. The fact that only the mass density can be anisotropic in acoustic metamaterials has not prevented the application of various electromagnetic metamaterial concepts to acoustics. However, when exploring sound interactions with metasurfaces, this missing element imposes severe restrictions.

Metasurfaces are the planarized version of metamaterials, yielding unique opportunities for wave manipulation along a surface. Translating bulk metamaterial concepts to metasurfaces allows minimizing the effect of loss, and enables easier access to field enhancement [92]. Hyperbolic metasurfaces in photonics have recently become an important class of such devices, enabling the unusual propagation properties of hyperbolic metamaterials, such as the unbounded local density of states and sub-diffraction imaging and canalization, over a planarized surface [197]-[199]. Like in the case of hyperbolic metamaterials, hyperbolic metasurfaces require an extreme anisotropic response for the two field polarizations along the surface, namely a surface impedance tensor with oppositely signed entries in the diagonal elements [197].

While bulk hyperbolic metamaterials have been realized in acoustics relying on mass anisotropy [192], so far there has been no concept nor implementation of acoustic hyperbolic metasurfaces. The reason lies in the symmetry constraints stemming from the

longitudinal nature of sound waves outlined above: the acoustic metasurface properties are described by the impedance relation $p = Z_s v_n$, where Z_s and v_n indicate surface impedance and particle velocity normal to the surface, respectively. The scalar nature of acoustic pressure and normal velocity restricts the acoustic surface impedance to be inherently scalar and isotropic, and hence prevents the realization of hyperbolic metasurfaces for sound, which would inherently require extreme anisotropy in the surface plane. While the discovery of metamaterials and metasurfaces have extensively enriched the portfolio of material and impedance properties for acoustic waves, such as negative bulk modulus and density-near-zero propagation, the nature of acoustic wave propagation appears to forbid the realization of anisotropic bulk modulus and surface impedances, challenging the implementation of hyperbolic propagation over a surface.

The introduction of nonlocal responses over an acoustic metasurface allows relaxing the mentioned symmetry constraints, and enables the implementation of acoustic anisotropic metasurfaces, opening a path towards extreme anisotropic responses in the surface impedance. In particular, we consider strong coupling and energy tunneling between neighboring unit cells over a surface, which introduces a new relation governing acoustic wave propagation over a surface. Different levels of anisotropy can be achieved in this regime by simply modulating coupling and energy tunneling in different directions, including extreme values that open to the possibility of hyperbolic sound transport over a surface. These same features also allow surface wave propagation with negative energy velocity. Different from previously reported bianisotropic metasurfaces using Willis resonant coupling, here anisotropy is induced through nonlocality, enabling

a direct extension of electromagnetic anisotropy to acoustics.

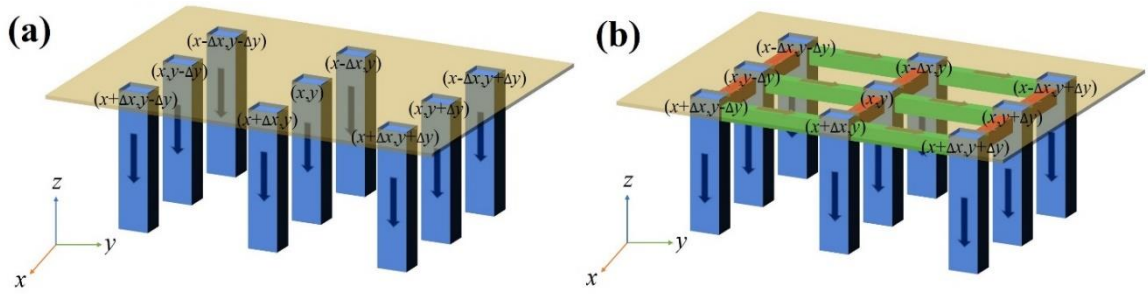

Figure 4.5. (a) Traditional design of acoustic local metasurface, whose units vibrate locally and separate from each other. (b) Anisotropic metasurface with coupling effects between units in different directions.

Figure 4.5 (a) sketches the usual definition of acoustic surface impedance, in which acoustic microstructures vibrate locally and separately from each other. These microstructures, which may be formed by Helmholtz resonators, acoustic maze-like structures or impedance tubes, have been extensively applied to the design of acoustic metasurfaces, achieving several functionalities, such as anomalous reflection, focusing, beamforming, enhanced absorption and more. All these microstructures, no matter how complex, can be mathematically described by their local impedance, defined through the impedance relation $p = Zv_n$. This relation only considers the local response of these microstructures and discards coupling between unit cells. Strictly speaking, this formula is only valid when the microstructures are deeply subwavelength, and with ideal rigid boundaries. However, it works well also in modeling realistic scenarios, and the reported theoretical and experimental results in various metasurface geometries using this

approach match each other very well, even for underwater metasurfaces in which the structure cannot be treated as rigid due to the high impedance of water [200]. This is mainly because the coupling between neighboring cells is typically negligible. An interesting way to overcome the scalar nature of the surface impedance and break symmetry consists in enabling and controlling the strong coupling between neighboring cells.

Figure 4.5 (b) depicts the proposed nonlocal metasurface, in which extra paths are opened to connect adjacent microstructures so that acoustic energy can tunnel from one unit cell to the next, transverse to the surface. As shown in Fig. 4.5 (b), at point (x, y) the conservation of mass requires

$$v_n(x,y)\Delta x\Delta y + U_x(x-\Delta x, y) + U_y(x, y-\Delta y) = U_s(x,y) + U_x(x,y) + U_y(x,y) \tag{3.28}$$

Here $v_n \Delta x \Delta y$ represents the volume velocity filled from the top of the metasurface, and Δx and Δy are the period of the units in *x*- and *y*-directions, respectively. U_s represents the volume velocity flow into the local unit. U_x and U_y represent the volume velocity contribution from coupling effect in *x*- and *y*-directions, respectively. For example, $U_x(x-\Delta x, y)$ represent the volume velocity coming from point $(x-\Delta x, y)$ and flow into (x, y). In the subwavelength scale, we are able to rewrite Eq. (3.28) into differential equation

$$v_n(x,y)\Delta x\Delta y = U_s(x,y) + \frac{\partial U_x(x,y)}{\partial x}\Delta x + \frac{\partial U_y(x,y)}{\partial y}\Delta y \tag{3.29}$$

Suppose the acoustic impedances of local unit, coupling paths in *x*- and *y*-directions can be expressed as Z_a, Z_x and Z_y, respectively. They should satisfy

$$p(x,y) = Z_a(x,y)U_s(x,y) \tag{3.30}$$

$$p(x,y) - p(x+\Delta x,y) = -\frac{\partial p(x,y)}{\partial x}\Delta x = U_x(x,y)Z_x(x,y) \tag{3.31}$$

$$p(x,y) - p(x,y+\Delta y) = -\frac{\partial p(x,y)}{\partial y}\Delta y = U_y(x,y)Z_y(x,y) \tag{3.32}$$

Substitute the expression of U_s, U_x and U_y from Eqs. (3.30), (3.31) and (3.32) into Eq. (3.29), we can get

$$v_n(x,y) = \frac{1}{\Delta x\Delta y}\frac{1}{Z_a(x,y)}p(x,y) - \frac{\partial}{\partial x}\left[\frac{\Delta x}{\Delta y}\frac{1}{Z_x(x,y)}\frac{\partial p(x,y)}{\partial x}\right] - \frac{\partial}{\partial y}\left[\frac{\Delta y}{\Delta x}\frac{1}{Z_y(x,y)}\frac{\partial p(x,y)}{\partial y}\right] \tag{3.33}$$

If we set $\frac{1}{Z_s(x,y)} = \frac{1}{\Delta x\Delta y}\frac{1}{Z_a(x,y)}$, $Y_x = \frac{\Delta x}{\Delta y}\frac{i\omega\rho_0}{Z_x(x,y)}$ and $Y_y = \frac{\Delta y}{\Delta x}\frac{i\omega\rho_0}{Z_y(x,y)}$, we are able to simplify Eq. (3.33) as

$$p = Z_s v_n + Z_s\frac{\partial(Y_x v_x)}{\partial x} + Z_s\frac{\partial(Y_y v_y)}{\partial y} \tag{3.34}$$

By tailoring the coupling coefficients, we can mold strong transverse responses in the metasurface, which have been neglected in previous metasurface implementations for sound, opening the path towards nonlocal and anisotropic responses over an acoustic surface.

4.5 Negative-index Airborne Surface Acoustic Waves

Equation (3.34) opens a new degree of freedom to tailor acoustic metasurfaces. In the following, we limit ourselves to homogeneous scenarios, i.e., $\partial Y_x/\partial x = 0$ and $\partial Y_y/\partial y = 0$. In this case, Eq. (3.34) can be simplified as

$$p = Z_s v_n + Z_s Y_x \frac{\partial v_x}{\partial x} + Z_s Y_y \frac{\partial v_y}{\partial y} \tag{3.35}$$

Consider an airborne acoustic surface wave traveling along the metasurface in the *x*-direction, with pressure $p = p_0 e^{-\gamma z} e^{ik_x x}$ and normal velocity $v_n = -v_z = \gamma p_0 e^{-\gamma z} e^{ik_x x} / \left(i\omega\rho_0\right)$. For a traditional impedance surface, i.e., $Y_x = 0$, the impedance satisfies $Z_s = p/v_n = i\omega\rho_0/\gamma$. Only when $\gamma > 0$, the surface acoustic wave can be excited, thus the impedance must be capacitive, i.e., $Z_s/i = \omega\rho_0/\gamma > 0$, to support surface wave propagation. However, if we consider nonlocal coupling, i.e. $Y_x \neq 0$, according to Eq. (3.35), we find the new dispersion relation $Z_s/i = \omega\rho_0 / \left(\gamma - Y_x k_x^2\right)$. For $Y_x > \gamma/k_x^2$, then $Z_s/i < 0$, indicating that an inductive surface can now support surface acoustic waves based on nonlocal interactions.

Figure 4.6 (a) presents three unit cells of the proposed nonlocal anisotropic metasurface, in which a coupling path is opened only in one direction. The left part, indicated by the blue color in each unit, is a local impedance tube, widely used in conventional acoustic metasurface designs. Here, we intentionally design the impedance tube to support an inductive response at the frequency of interest, by controlling its length. The right part, indicated by green color in each unit, is an additional path

connecting adjacent local impedance tubes, which enables energy tunneling from one tube to the next, yielding strong nonlocality. Figure 4.6 (b) presents the acoustic pressure distribution for a line source excitation along the *y*-direction, which launches a wave traveling along *x* (the direction of the coupling paths, $Y_x \neq 0$, $Y_y = 0$). As predicted by our theory, a surface acoustic wave travels along the metasurface in the *x*-direction, despite the inductive nature of the surface elements. To make sure that the surface wave is indeed supported by the metasurface nonlocality, we remove the coupling paths and analyze the corresponding pressure distribution [Figure 4.6 (d)]. The result clearly shows that no surface wave can be excited over a local inductive metasurface, verifying that the surface acoustic wave excitation in Fig. 4.6 (b) is due to the metasurface nonlocality. In order to verify the anisotropic properties of the metasurface, we rotate each unit cell by 90 degrees, so that the coupling paths are oriented along *y* (i.e., $Y_x = 0$, $Y_y \neq 0$). Now the coupling paths have no effect on waves propagating along *x,* and hence surface acoustic waves are not expected for this excitation, as verified in Fig. 4.6 (e).

The grey arrows in each panel of Fig. 4.6 indicate the phase velocity direction. In Fig. 4.6 (b), we find that the phase velocity points towards the source, suggesting propagation with a negative phase index. Negative index propagation is common in bulk metamaterials, supporting an energy flow away from the source, while the phase velocity points towards it. However, negative index propagation over metasurfaces is more challenging: Fig. 4.6 (c) presents the *x*-component of the Poynting vector along the surface for the design shown in Fig. 4.6 (b), indicating that, interestingly, the surface

wave energy flow above the metasurface also points towards the source. Intuitively, this phenomenon appears to violate causality and energy conservation. To gain physical understanding into this phenomenon, we analytically calculate the power flow of the surface wave in the *x*-direction above the metasurface

$$P_{surf} = \frac{1}{2}\int_0^{\infty} \mathrm{Re}\left(p v_x^{*} \Delta y \right) dz \tag{3.36}$$

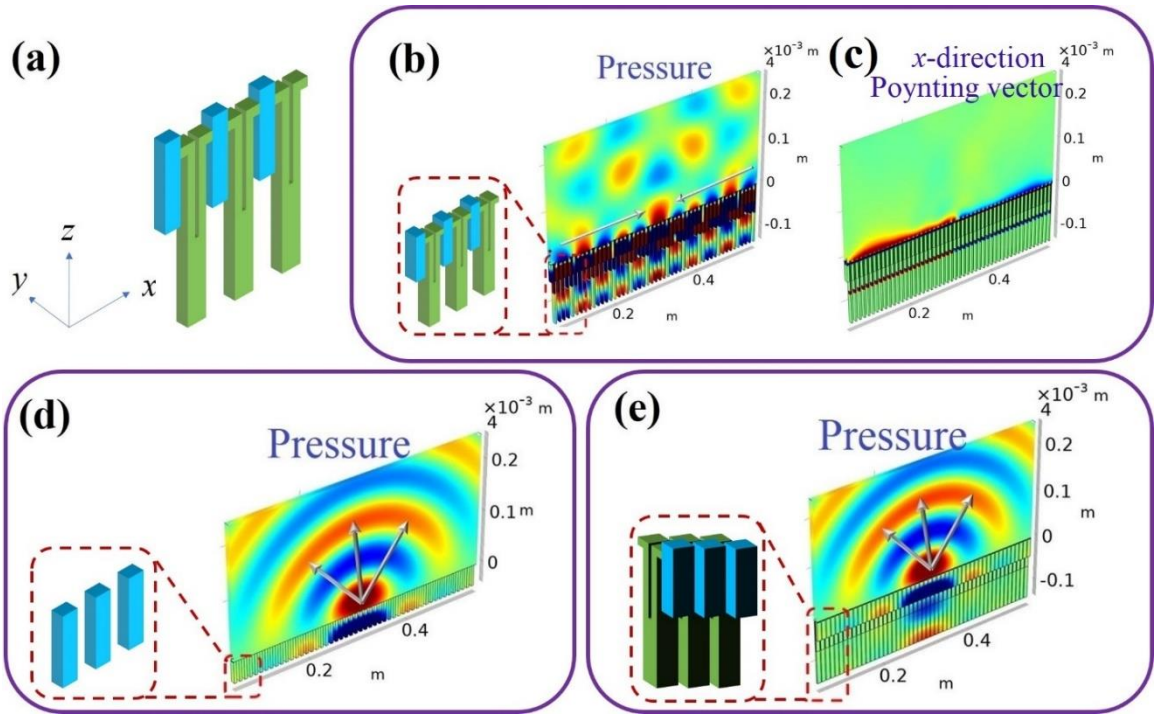

Figure 4.6. (a) Three unit cells of the nonlocal anisotropic metasurface. (b) Pressure distribution for a *y*-directional line source exciting acoustic waves traveling along the *x*-direction, with *x*-direction coupling paths. (c) *x*-direction Poynting vector distribution. On the surface, the energy flows towards the source. (d) Pressure distribution for a *y*-directional line source exciting above an inductive metasurface with only local impedance tubes. No surface wave can be excited. (e) Pressure distribution for a *y*-directional line source exciting acoustic waves traveling along *x* with *y*-direction coupling paths.

Supposing the pressure distribution over the metasurface to be $p = p_0 e^{-\gamma z} e^{ik_x x}$ and substitute it into Eq. (3.36), we get

$$P_{surf} = \frac{1}{2}\int_0^{\infty} \mathrm{Re}\left(p v_x^* \Delta y \right) dz = \frac{|p_0|^2 k_x}{4\gamma\omega\rho_0}\Delta y \tag{3.37}$$

Equation (3.37) indicates that P_{surf} and k_x have the same sign, i.e., the direction of power flow and phase velocity should be the same, confirming that a negative phase velocity corresponds to a negative energy velocity flowing of the surface wave towards the source, as shown in Fig. 4.6 (b) and 4.6 (c). This paradox can be resolved by considering nonlocality: since the metasurface is nonlocal, additional power can flow through the coupling paths, which contributes to the total energy flow. The power flow through tunneling is

$$P_{tunnel} = \frac{1}{2}\mathrm{Re}\left(p U_x^* \right) \tag{3.38}$$

Inside the metasurface, the pressure should be equal to the pressure at z=0 due to continuity satisfying $p = p_0 e^{ik_x x}$. Substitute it into Eq. (3.38) and notice the expression of U_x from Eq. (3.31), we have

$$P_{tunnel} = \frac{1}{2}\mathrm{Re}\left(p^* U_x \right) = -\frac{|p_0|^2 k_x Y_x}{2\omega\rho_0}\Delta y \tag{3.39}$$

From Eq. (3.37) and (3.39), we get the total power flow, which is the sum of the power traveling above the metasurface and the tunneling power

$$P_{tot} = P_{surf} + P_{tunnel} = \frac{|p_0|^2 k_x}{4\omega\rho_0} \Delta y \frac{1-2\gamma Y_x}{\gamma} \tag{3.40}$$

Eq. (3.40) represents the power flow expression when considering nonlocality. From Eq. (3.40), we find that, when the term $(1-2\gamma Y_x)$ is positive, (i.e. $Y_x < 1/(2\gamma)$), P_{tot} and k_x have the same sign, indicating positive index propagation. When the term $(1-2\gamma Y_x)$ is negative, (i.e., $Y_x > 1/(2\gamma)$), however, P_{tot} and k_x have opposite signs. Since P_{tot} indicates the total power radiated from the source, which is positive, k_x is actually expected to be negative, requiring backward surface wave propagation and yielding a negative index propagation driven by nonlocality. According to Eq. (3.37), the power flow of the surface wave above the metasurface P_{surf} is also negative. This phenomenon is enabled by the strong energy flow, with opposite sign, sustained in the coupling channels responsible for the strong nonlocality. Figure 4.6 corresponds to the situation in which the surface wave is backward.

4.6 Hyperbolic Sound Propagation Over a Surface

The anisotropic surface wave shown in Fig. 4.6 (b) and 4.6 (d) enables extreme wave propagation features. By introducing an additional tube to the geometry shown in Fig. 4.6 (a), as indicated by the red color, we open coupling paths in both *x*- and *y*-directions. The resulting metasurface geometry, shown in Fig. 4.7 (a), is excited by a point source located in the middle of the sample. A strong surface wave is excited and

localized on the metasurface, yielding a hyperbolic profile of the surface wavefronts, with energy localized along with specific directions, shown in Fig. 4.7 (b). The wave, with propagation properties consistent with hyperbolic surface wave propagation in nanophotonics, is confined on the surface, and rapidly decays as we move out of the plane. In order to verify the propagation properties of the surface wave $p = p_0 e^{-\gamma z} e^{i(k_x x + k_y y)}$, we replace this expression into Eq. (3.35), and obtain

$$Y_x k_x^2 + Y_y k_y^2 = \frac{\omega \rho_0}{i Z_s} + \sqrt{k_x^2 + k_y^2 - k_0^2} \tag{3.41}$$

The asymptotes for $k_x \to \infty$ and $k_y \to \infty$ are $k_y = \sqrt{-Y_x / Y_y}\, k_x$. Thus, in order to achieve hyperbolic surface wave propagation the signs of Y_x and Y_y must be opposite, yielding in principle an unbounded local density of states over the entire frequency range over these two parameters can be maintained oppositely signed.

By modulating the cross-sectional area of the coupling tube (red color) in the *y*-direction, we can modulate the value of Y_y, and hence impart different hyperbolic profiles to the dispersion diagram. Figure 4.7 (c) presents the pressure profile for a unit with a smaller cross-sectional area, and hence smaller Y_y compared with Fig. 4.7 (b). Figures 4.8 (a) and (b) present the isofrequency contours of the metasurface shown in Fig. 4.7 (b) and (c), respectively, which confirm a hyperbolic profile with varying asymptotes. In these plots, the inner region corresponds to higher frequencies, while the outer region corresponds to low frequencies. Hence, the group velocity $\vec{v}_g = \nabla_{\vec{k}} \omega$ in the *x*-direction is opposite to the phase velocity, as indicated by the red arrows.

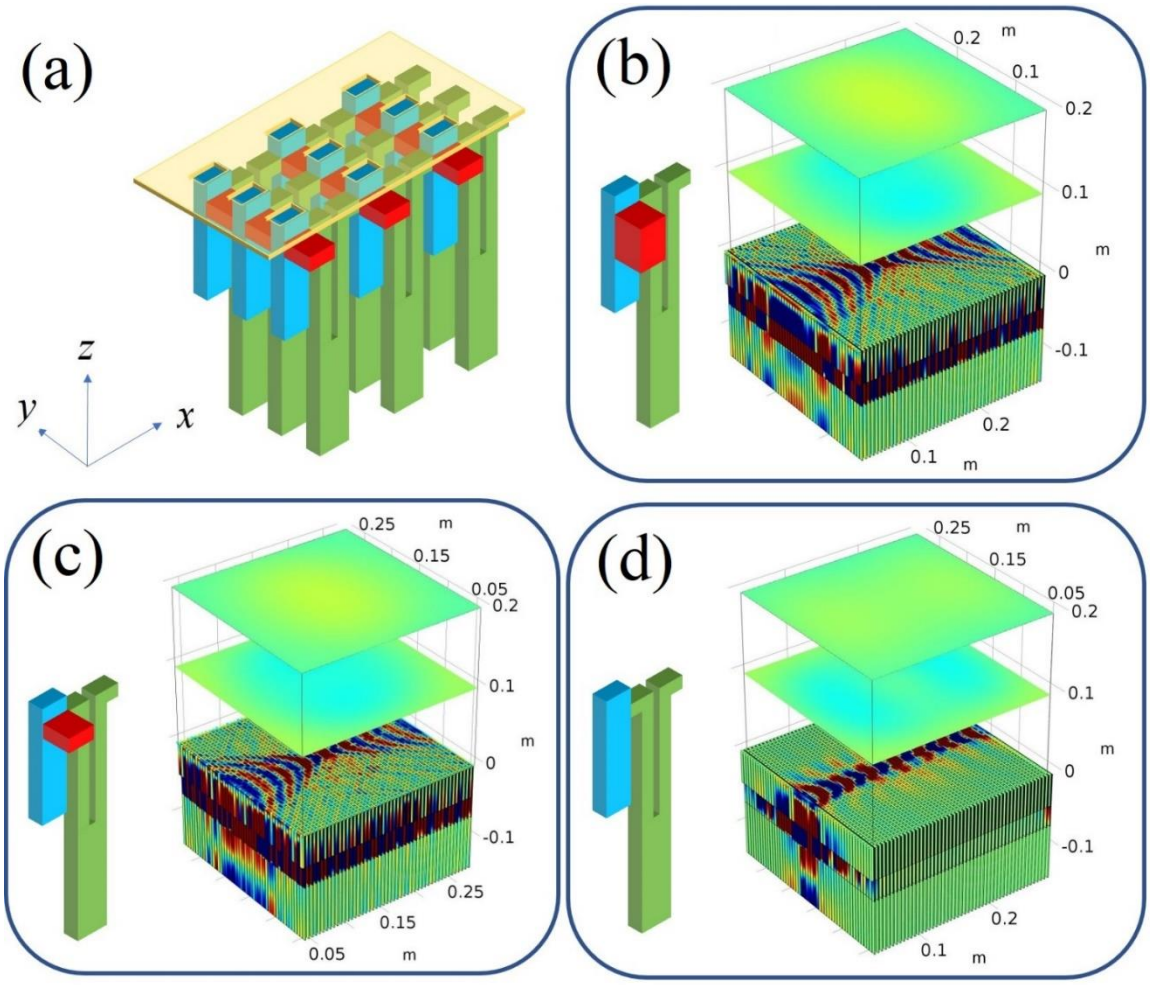

Figure 4.7. (a) Hyperbolic acoustic metasurface based on nonlocality. (b and c) Pressure distribution of the hyperbolic metasurface designed with coupling tubes with different cross-sectional area in *y*-directions. (d) Pressure distribution of hyperbolic metasurface working in the canalization region by completely removing the coupling tube in the *y*-direction.

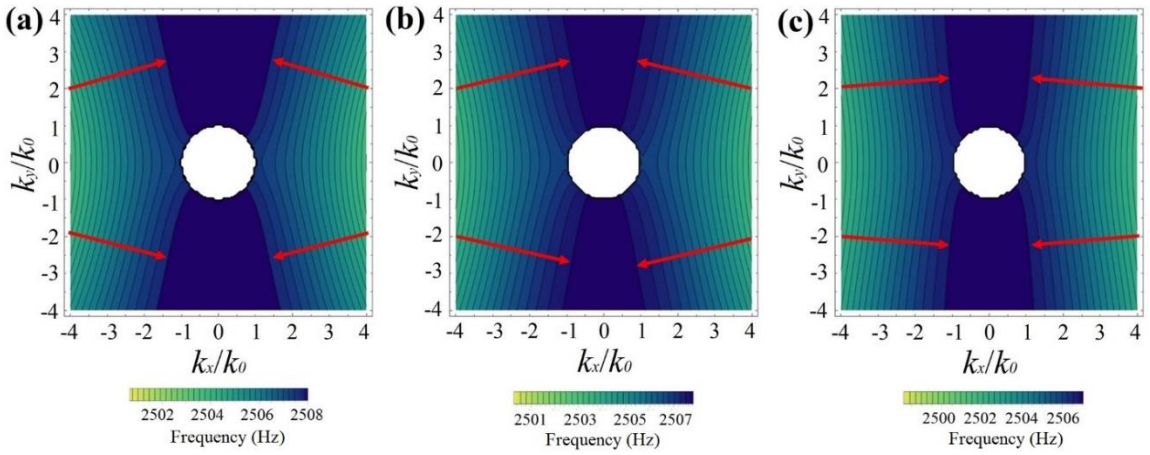

Figure 4.8. (a, b, c) Dispersion relation of the metasurface shown in Fig. 4.7 (b,c,d), respectively. The dispersion relation is obtained from the total waves including the surface waves and the tunneling waves. The dispersion relation confirms hyperbolic propagation with varying asymptotes, controlled by the nonlocality.

According to the asymptote expression $k_y = \sqrt{-Y_x/Y_y}k_x$, for smaller Y_y, the asymptote gets closer to the *y*-direction. However, compared with Fig. 4.7 (b), surface wave propagation in Fig. 4.7 (c) is more focused in the *x*-direction. This is because the phase velocity direction is different from the group velocity in hyperbolic surfaces, as shown in the isofrequency contour in Fig. 4.8. In the extreme case $k_x \to \infty$, $k_y \to \infty$, the group velocity is perpendicular to the phase velocity. Hence, an asymptote closer to the *y*-direction implies more energy flowing towards *x*. This is indeed verified in Fig. 4.7 (d), in which we consider the extreme scenario $Y_y \to 0$, i.e., no coupling in the *y*-direction. In this case, the asymptote $k_y = \sqrt{-Y_x/Y_y}k_x$ becomes parallel to the *y*-axes and energy propagates in the *x*-direction, corresponding to the canalization regime

[201][202], in which surface waves propagate without diffraction along the surface in specific directions, with exciting opportunities for imaging. The corresponding isofrequency contour is shown in Fig. 4.8 (c), confirming the canalization properties of the surface.

CHAPTER 5: CONCLUSION

This dissertation summarizes the work I have done during my Ph.D. study in the past 5 years, which is a comprehensive research of nonlocal phenomena in acoustics.

It starts by analyzing nonlocal phenomena in a single inclusion. I first introduced an analytical model for general acoustic scatterers and studied the restrictions imposed by reciprocity and energy conservation on their polarizabilities and derived tight theoretical bounds for the acoustic bianisotropic coupling coefficient. It was proven that bianisotropic coupling in acoustics can be of the same order as the diagonal components of the polarizability tensor. This finding paves the way to translate many fascinating opportunities enabled by bianisotropy from electrodynamics to acoustics. Furthermore, I proposed a systematic approach to design realistic scatterers that provide maximum bianisotropic coupling, reaching the theoretical bound. As an application of the proposed inclusions, I employed them as building blocks to realize an acoustic metagrating that reroutes a normally incident wave to extreme directions in reflection with unitary efficiency. Then I studied the nonlocal properties of a nonreciprocal inclusion. I have derived the maximum Willis coupling bound for non-reciprocal acoustic scatterers and find that the previous maximum bound derived for reciprocal scatterers cannot be exceeded even we break the reciprocal, as long as the scatterers are passive. I proposed the systematic design approach to reach maximum non-reciprocal Willis coupling in symmetric scatterers with very weak bias. I study the lossless scatterers and lossy scatterers, respectively and find that the magnitudes of both cross-coupling

polarizabilities need to be identical if the scatterers are lossless while their magnitudes can be different if the scatterers are lossy. At the end of Chapter 2, I utilize the proposed non-reciprocal scatterer to design meta-grating which can achieve non-reciprocal unitary reflections.

Next, I studied the nonlocal phenomena in bulk metamaterials. I presented a Willis metamaterial operating near the zero-index operation, yielding extreme nonreciprocal responses with modest airflow. These unusual acoustic properties are the result of a nonreciprocal bianisotropic response dominating the effective properties of the metamaterial, as the reciprocal response tends to zero. For this reason, even modest air flows can provide highly unusual responses, including opposite (positive-to-negative) refractive indices for opposite propagation directions, and nonreciprocal lenses. Within the proposed Willis metamaterial, the airflow can be modulated in real-time to reconfigure the properties of the metamaterial, making it an exciting platform to control sound beyond the conventional limitations of natural materials. By applying background flow in coiling structure metamaterials, I also mimic effective magnetic field for phonon flow with very low background flow speed and realize the synthetic phonon cyclotron. The sound wave traveling in the effective magnetic field can be derivate by the effective Lorentz force and moving in a circle. Further studies also show that the effective magnetic field can realize acoustical topological edge states which is robustness to defects and disorders.

Finally, I studied nonlocal phenomena over acoustic metasurfaces. I introduced an approach to realize low-profile planar metasurfaces with unitary efficiency in acoustic

wavefront transformation using engineered nonlocality. The nonlocal effect is realized by introducing a connecting path between neighboring unit cells, so that the energy can tunnel through, and synthesize effective loss and gain profiles in the effective local description of the surface. We then consider the presence of a viscous and thermal loss in the involved materials, showing that the phenomenon is rather robust to imperfections. Different from other approaches, my design does not require engineering additional reactive fields in the proximity of the surface, and it is directly based on an analytical approach with simple design guidelines. In its actual acoustic implementation, I consider a meandering tube to synthesize the required local and nonlocal impedance profile, achieving high efficiencies even in coarsely discretized impedance profiles. Although this approach is proposed in the field of acoustics, similar approaches may be explored in electromagnetics, optics and for elastic waves, with interesting opportunities in a wide range of applications. In the dissertation, I focus my attention on the canonical problem of beam steering, but the analysis can be straightforwardly extended to other wavefront transformations, such as for focusing or beam multiplexing. Finally, I showed that strong nonlocal responses enabled by tunneling channels connecting neighboring unit cells in acoustic metasurfaces can overcome the inherent isotropy of the acoustic surface impedance imposed by symmetry constraints in sound propagation, and enable extreme acoustic anisotropy driven by nonlocality over a surface. This new degree of freedom opens several opportunities for surface acoustic waves, e.g., wave propagation above inductive surfaces, hyperbolic surface wave transport, negative phase, and energy

velocities of surface waves. These findings can be an important tool for the design of new surface acoustic wave devices and acoustic metasurfaces.

BIBLIOGRAPHY

[1]. A. Fenster, and D. B. Downey, 3-D ultrasound imaging: A review, IEEE Eng. Med. Biol. 14, 41-51 (1996).

[2]. A. Fenster, D. B. Downey, and H. N. Cardinal, Three-dimensional ultrasound imaging, Phys. Med. Biol. 46, R67-R99 (2001).

[3]. S. Vaezy, X. Shi, R. W. Martin, E. Chi, P. I. Nelson, M. R. Bailey, and L. A. Crum, Real-time visualization of focused ultrasound therapy, Ultrasound Med. Biol. 27, 33-42 (2003).

[4]. S. Hernot, and A. L. Klibanov, Microbubbles in ultrasound-triggered drug and gene delivery, Adv. Drug. Deliv. Rev. 60, 1153-1166 (2008).

[5]. K. Ferrara, R. Pollard, M. Borden, Ultrasound microbubble contrast agents: fundamentals and application to gene and drug delivery, Annu. Rev. Biomed. Eng. 9, 415-447 (2007).

[6]. K. Y. Jhang, and K. C. Kim, Evaluation of material degradation using nonlinear acoustic effect, Ultrasonics 37, 39-44 (1999).

[7]. B. W. Drinkwater, and P. D. Wilcox, Ultrasonic arrays for non-destructive evaluation: A review. NDT&E Int. 39, 525-541 (2006).

[8]. L. Quan, X. Liu, and X. Gong, Nonlinear nonclassical acoustic method for detecting the location of cracks, J. Appl. Phys. 112, 054906 (2012).

[9]. D. Rouseff, D. R. Jackson, W. L. J. Fox, C, D, Jones, J. A. Ritcey, and D. R. Dowling, Underwater acoustic communication by passive-phase-conjugation: Theory and experimental results, IEEE J. Ocean. Eng. 26, 821-831 (2001).

[10]. B. Li, S. Zhou, M. Stojanovic, L. Freitag, and P. Willett, Multicarrier communication over underwater acoustic channels with nonuniform Doppler shifts, IEEE J. Ocean. Eng. 33, 198-209 (2008).

[11]. S. A. Cummer, J. Christensen, and A. Alu, Controlling sound with acoustic metamaterials, Nat. Rev. Mater. 1, 16001 (2016).

[12]. G. Ma, and P. Sheng, Acoustic metamaterials: From local resonances to broad horizons, Sci. Adv. 2, e1501595 (2016).

[13]. Z. Liu, X. Zhang, Y. Mao, Y. Y. Zhu, Z. Yang, C. T. Chan, and P. Sheng, Locally resonant sonic materials, Science 289, 1734-1736 (2000).

[14]. J. Li, and C. T. Chan, Double-negative acoustic metamaterial, Phys. Rev. E 70, 055602(R) (2004).

[15]. Y. Ding, Z. Liu, C. Qiu, and J. Shi, Metamaterial with simultaneously negative bulk modulus and mass density, Phys. Rev. Lett. 99, 093904 (2007).

[16]. C. Shen, J. Xu, N. X. Fang, and Y. Jing, Anisotropic complementary acoustic metamaterial for canceling out aberrating layers, Phys. Rev. X 4, 041033 (2014).

[17]. T. Klatt, and M. R. Haberman, A nonlinear negative stiffness metamaterial unit cell and small-on-large multiscale material model, J. Appl. Phys. 114, 033503 (2013).

[18]. B. M. Goldsberry, and M. R. Haberman, Negative stiffness honeycombs as tunable elastic metamaterials, J. Appl. Phys. 123, 091711 (2018).

[19]. L. Quan, F. Qian, X. Liu, and X. Gong, A nonlinear acoustic metamaterials: Realization of a backwards-travelling second-harmonic sound wave, J. Acoust. Soc. Am. 139, 3373-3385 (2016).

[20]. J. Christensen, A. I. Fernandez-Dominguez, F. de Leon-Perez, L. Martin-Moreno, and F. J. Garcia-Vidal, Collimation of sound assisted by acoustic surface waves, Nature Phys. 3, 851-852 (2007).

[21]. L. Quan, X. Zhong, X. Liu, X. Gong, and P. A. Johnson, Effective impedance boundary optimization and its contribution to dipole radiation and radiation pattern control, Nat. Commun. 5, 3188 (2014).

[22]. L. Quan, F. Qian, X. Liu, X. Gong, and P. A. Johnson, Mimicking surface plasmons in acoustics at low frequency, Phys. Rev. B 92, 104105 (2015).

[23]. B. Liang, B. Yuan, and J. Cheng, Acoustic diode: Rectification of acoustic energy flux in one-dimensional system, Phys. Rev. Lett. 103, 104301 (2009).

[24]. B. Liang, X. S. Guo, J. Tu, D. Zhang, and J. C. Cheng, An acoustic rectifier, Nat. Mater. 9, 989-992 (2010).

[25]. N. Boechler, G. Theocharis, and C. Daraio, Bifurcation-based acoustic switching and rectification, Nat. Mater. 10, 665-668 (2011).

[26]. R. Fleury, D. L. Sounas, C. F. Sieck, M. R. Haberman, and A. Alu, Sound isolation and giant linear nonreciprocity in a compact acoustic circulator, Science 343, 516-519 (2014).

[27]. J. C. Bose, On the rotation of plane of polarization of electric waves by a twisted structure, Proc. R. Soc. Lond. 63, 146-152 (1898).

[28]. V. G. Veselago, The electrodynamics of substances with simultaneously negative values of ε and μ, Sov. Phys. Usp. 10, 509 (1968).

[29]. J. B. Pendry, A. J. Holden, W. J. Stewart, and I. Youngs, Extremely low frequency plasmons in metallic mesostructures, Phys. Rev. Lett. 76, 4773 (1996).

[30]. R. Shelby, D. R. Smith and S. Schultz, Experimental verification of a negative index of refraction, Science 279, 77 (2001).

[31]. J. B. Pendry, Negative refraction makes a perfect lens, Phys. Rev. Lett. 85, 3966 (2000).

[32]. J. B. Pendry, D. Schurig, and D. R. Smith, Controlling electromagnetic fields, Science 312, 1780-1782 (2006).

[33]. D. Schurig, J. J. Mock, B. J. Justice, S. A. Cummer, J. B. Pendry, A. F. Starr, and D. R. Smith, Metamaterial electromagnetic cloak at microwave frequencies, Science 314, 977-980 (2006).

[34]. J. B. Pendry, L. Martin-Moreno, and F. J. Garcia-Vidal, Mimicking surface plasmons with structured surfaces, Science 305, 847-848 (2004).

[35]. H. J. Lezec, A. Degiron, E. Devaux, R. A. Linke, L. Martin-Moreno, and F. J. Garcia-Vidal, T. W. Ebbesen, Beaming light from a subwavelength aperture, Science 297, 820-822 (2002).

[36]. A. Alu, and N. Engheta, Achieving transparency with plasmonic and metamaterial coatings, Phys. Rev. E 72, 016623 (2005).

[37]. N. Engheta, Circuits with light at nanoscales: optical nanocircuits inspired by metamaterials, Science 317, 1698-1702 (2007).

[38]. A. Alu, M. G. Silveirinha, A. Salandrino, and N. Engheta, Epsilon-near-zero metamaterials and electromagnetic sources: Tailoring the radiation phase pattern, Phys. Rev. B 75, 155410 (2007).

[39]. N. Fang, H. Lee, C. Sun, and X. Zhang, Sub-diffraction-limited optical imaging with a silver superlens, Science 308, 534-537 (2005).

[40]. J. Valentine, S. Zhang, T. Zentgraf, E. Ulin-Avila, D. A. Genov, G. Bartal, and X. Zhang, Three-dimensional optical metamaterial with a negative refractive index, Nature 455, 376-379 (2008).

[41]. Z. Liu, H. Lee, Y. Xiong, C. Sun, and X. Zhang, Far-field optical hyperlens magnifying sub-diffraction-limited objects, Science 315, 1686 (2007).

[42]. A. J. Hoffman, L. Alekseyev, S. S. Howard, K. J. Franz, D. Wasserman, V. A. Podolskiy, E. E. Narimanov, D. L. Sivco, and C. Gmachl, Negative refraction in semiconductor metamaterials, Nat. Mater. 6, 946 (2007).

[43]. J. Li, and C. T. Chan, Double-negative acoustic metamaterial, Phys. Rev. E 70, 055602 (R) (2004).

[44]. N. Fang, D. Xi, J. Xu, M. Ambati, W. Srituravanich, C. Sun, and X. Zhang, Ultrasonic metamaterials with negative modulus, Nat. Mater. 5, 452-456 (2006).

[45]. L. Fok, and X. Zhang, Negative acoustic index metamaterial, Phys. Rev. B 83, 214304 (2011).

[46]. F. Bongard, H. Lissek, and J. R. Mosig, Acoustic transmission line metamaterial with negative/zero/positive refractive index, Phys. Rev. B 82, 094306 (2010).

[47]. S. H. Lee, C. M. Park, Y. M. Seo, Z. G. Wang, and C. K. Kim, Composite acoustic medium with simultaneously negative density, Phys. Rev. Lett. 104, 054301 (2010).

[48]. H. Chen, and C. T. Chan, Acoustic cloaking in three dimensions using acoustic metamaterials, Appl. Phys. Lett. 91, 183518 (2007).

[49]. Y. Cheng, F. Yang, J. Y. Xu, and X. J. Liu, A multilayer structured acoustic cloak with homogeneous isotropic materials, Appl. Phys. Lett. 92, 151913 (2008).

[50]. S. A. Cummer, B.-I. Popa, D. Schurig, D. R. Smith, J. Pendry, M. Rahm, and A. Starr, Scattering theory derivation of a 3D acoustic cloaking shell, Phys. Rev. Lett. 100, 024301 (2008).

[51]. S. Zhang, C. Xia, and N. Fang, Broadband acoustic cloak for ultrasound waves, Phys. Rev. Lett. 106, 024301 (2011).

[52]. J. Li, L. Fok, X. Yin, G. Bartal, and X. Zhang, Experimental demonstration of an acoustic magnifying hyperlens, Nat. Mater. 8, 931-934 (2009).

[53]. Y. Cheng, C. Zhou, Q. Wei, D.J. Wu, and X.J. Liu, Acoustic subwavelength imaging of subsurface objects with acoustic resonant metalens, Appl. Phys. Lett. 103, 224104 (2013).

[54]. D. Torrent, and J. Sanchez-Dehesa, Anisotropic mass density by two-dimensional acoustic metamaterials, New J. Phys. 10, 023004 (2008).

[55]. D. Torrent and J. Sanchez-Dehesa, Anisotropic mass density by radially periodic fluid structures, Phys. Rev. Lett. 105, 174301 (2010).

[56]. J. R. Willis, Variational principles for dynamic problems for inhomogeneous elastic media, Wave Motion 3, 1 (1981).

[57]. L. Quan, Y. Ra'di, D. Sounas, and A. Alu, Maximum Willis coupling in acoustic scatterers, Phys. Rev. Lett. 120, 254301 (2018).

[58]. A. Melnikov, Y. K. Chiang, L. Quan, S. Oberst, A. Alu, S. Marburg, and D. Powell, Acoustic meta-atom with experimentally verified maximum Willis coupling, Nat. Commun. 10, 3148 (2019).

[59]. L. Quan, D. L. Sounas, and A. Alu, Nonreciprocal Willis coupling in zero-index moving media, Phys. Rev. Lett. 123, 064301 (2019).

[60]. L. Quan, and A. Alu, Passive acoustic metasurface with unitary reflection based on nonlocality, Phys. Rev. Appl. 11, 054077 (2019).

[61]. L. Quan, and A. Alu, Hyperbolic sound propagation over nonlocal acoustic metasurfaces, Phys. Rev. Lett. 123, 244303 (2019).

[62]. N. Engheta and R. W. Ziolkowski, Metamaterials: Physics and Engineering Explorations (IEEE, Piscataway, NJ, 2006).

[63]. N. I. Zheludev and Y. S. Kivshar, From metamaterials to metadevices, Nat. Mater. 11, 917 (2012).

[64]. Y. Zhao, X.-X. Liu, and A. Alù, Recent advances on optical metasurfaces, J. Opt. 16, 123001 (2014).

[65]. N. Yu, and F. Capasso, Flat optics with designer metasurfaces, Nat. Mater. 13, 139 (2014).

[66]. S. B. Glybovski, S. A. Tretyakov, P. A. Belov, Y. S. Kivshar, and C. R. Simovshi, Metasurfaces: From microwaves to visible, Phys. Rep. 634, 1 (2016).

[67]. X. Fang, J. Wen, B. Bonello, J. Yin, and D. Yu, Ultra-low and ultra-broad-band nonlinear acoustic metamaterials, Nat. Commun. 8, 1288 (2017).

[68]. B.-I. Popa, and S. A. Cummer, Non-reciprocal and highly nonlinear active acoustic metamaterials, Nat. Commun. 5, 3398 (2014).

[69]. Y. Zhou, M.-H. Liu, L. Feng, X. Ni, Y.-F. Chen, Y.-Y. Zhu, S.-N. Zhu, and N.-B. Ming, Phys. Rev. Lett. 104, 164301 (2010).

[70]. J. Christensen, A. I. Fernandez-Dominguez, F. de Leon-Perez, L. Martin-Moreno, and F. J. Garcia-Vidal, Collimation of sound assisted by acoustic surface waves, Nat. Phys. 3, 851-852 (2007).

[71]. Z. Yang, J. Mei, M. Yang, N. H. Chan, and P. Sheng, Membrane-Type acoustic metamaterial with negative dynamic mass, Phys. Rev. Lett. 101, 204301 (2008).

[72]. M. Yang, G. Ma, Z. Yang, and P. Sheng, Coupled membranes with doubly negative mass density and bulk modulus, Phys. Rev. Lett. 110, 134301 (2013).

[73]. Y. Cheng, J. Y. Xu, and X. J. Liu, One-dimensional structured ultrasonic metamaterials with simultaneously negative dynamic density and modulus, Phys. Rev. B 77, 045134 (2008).

[74]. Z. Liang, and J. Li, Extreme acoustic metamaterials by coiling up space, Phys. Rev. Lett. 108, 114301 (2012).

[75]. Y. Xie, B.-I. Popa, L. Zigoneanu, and S. A. Cummer, Measurement of a broadband negative index with space-coiling acoustic metamaterials, Phys. Rev. Lett. 110, 175501 (2013).

[76]. G. W. Milton, and J. R. Willis, On modifications of Newton's second law and linear continuum elastodynamic, Proc. R. Soc. A 463. 855 (2007).

[77]. A. N. Norris, A. L. Shuvalov, and A. A. Kutesnko, Analytical formulation of three-dimensional dynamic homogenization for periodic elastic system, Proc. R. Soc. A 468, 1629 (2012).

[78]. M. B. Muhlestein, C. F. Sieck, A. Alu, and M. R. Haberman, Reciprocity, passivity and causality in Willis materials, Proc. R. Soc. A 472, 20160604 (2016).

[79]. C. F. Sieck, A. Alu, and M. R. Haberman, Origins of Willis coupling and acoustic bianisotropy in acoustic metamaterials through source-driven homogenization, Phys. Rev. B 96, 104303 (2017).

[80]. S. Koo, C. Cho, J. Jeong, and N. Park, Acoustic omni meta-atom for decoupled access to all octants of a wave parameter space, Nat. Commun. 7, 13012 (2016).

[81]. M. B. Muhlestein, C. F. Sieck, P. S. Wilson, and M. R. Haberman, Experimental evidence of Willis coupling in a one-dimensional effective material element, Nat. Commun. 8, 15625 (2017).

[82]. I. Sersic, C. Tuambilangana, T. Kampfrath, and A. F. Koenderink, Magnetoelectric point scattering theory for metamaterial scatters, Phys. Rev. B 83, 245102 (2011).

[83]. D. T. Blackstock, Fundamentals of Physical Acoustics (Wiley, 2000).

[84]. S. A. Tretyakov, F. Mariotte, C. R. Simovski, T. G. Kharina, and J.-P. Heliot, Analytical antenna model for chiral scatterers: Comparison with numerical and experimental data, IEEE Trans. Antennas Propag. 44, 1006 (1996).

[85]. P. A. Belov, S. I. Maslovski, K. R. Simovski, and S. A. Tretyakov, A condition imposed on the electromagnetic polarizability of a bianisotropic lossless scatterer, Tech. Phys. Lett. 29, 718 (2003) (translated from Russian).

[86]. M. Albooyeh, V. S. Asadchy, R. Alaee, S.M. Hashemi, M. Yazdi, M. S. Mirmoosa, C. Rockstuhl, C. R. Simovski, and S. A. Tretyakov, Purely bianisotropic scatterers, Phys. Rev. B 94, 245428 (2016).

[87]. F. B. Arango and A F. Koenderink, Polarizability tensor retrieval for magnetic and plasmonic antenna design, New J. Phys. 15, 073023 (2013).

[88]. M. S. Mirmoosa, Y. Ra'di, V. S. Asadchy, C. R. Simovski, and S. A. Tretyakov, Polarizabilities of nonreciprocal bianisotropic particles, Phys. Rev. Appl. 1, 034005 (2014).

[89]. Y. Ra'di, V. S. Asadchy, and S. A. Tretyakov, Total absorption of electromagnetic waves in ultimately thin layers, IEEE Trans. Antennas Propag. 61, 4606 (2013).

[90]. Y. Ra'di, V. S. Asadchy, and S. A. Tretyakov, One-way transparent sheets, Phys. Rev. B 89, 075109 (2014).

[91]. Y. Ra'di, D. L. Sounas, and A. Alù, Metagratings: Beyond the Limits of Graded Metasurfaces for Wave Front Control, Phys. Rev. Lett. 119, 067404 (2017).

[92]. N. Yu, P. Genevet, M. A. Kats, F. Aieta, J.-P. Tetienne, F. Capasso, and Z. Gaburro, Light propagation with phase discontinuities: Generalized laws of reflection and refraction, Science 334, 333 (2011).

[93]. J. Mei and Y. Wu, Controllable transmission and total reflection through an impedance-matched acoustic metasurface, New J. Phys. 16, 123007 (2014).

[94]. Y. Li, X. Jiang, B. Liang, J.-C. Cheng, and L. Zhang, Metascreen-based acoustic passive phased array, Phys. Rev. Appl. 4, 024003 (2015).

[95]. J. Rosen, Symmetry rules: How science and nature are founded on symmetry, (Springer, 2008).

[96]. S. Weinberg, Lectures on quantum mechanics, Second Edition, (Cambridge University Press, 2015).

[97]. C. Caloz, A. Alu, S. Tretyakov, D. Sounas, K. Achouri, and Z.-L. Deck-Leger, Electromagnetic nonreciprocity, Phys. Rev. Appl. 10, 047001 (2018).

[98]. Z. Wang, Y. Chong, J. D. Joannopoulos, and M. Soljacic, Observation of unidirectional backscattering-immune topological electromagnetic states, Nature (London) 461, 772 (2009).

[99]. F. D. M. Haldane and S. Raghu, Possible Realization of Directional Optical Waveguides in Photonic Crystals with Broken Time-Reversal Symmetry, Phys. Rev. Lett. 100, 013904 (2008).

[100]. T. Kodera, D. L. Sounas, and C. Caloz, Artificial Faraday rotation using a ring metamaterial structure without static magnetic field, Appl. Phys. Lett. 99, 031114 (2011).

[101]. B. I. Popa and S. A. Cummer, Nonreciprocal active metamaterials, Phys. Rev. B 85, 205101 (2012).

[102]. D. L. Sounas, C. Caloz, and A. Alù, Giant non-reciprocity at the subwavelength scale using angular momentum-biased metamaterials, Nat. Commun. 4, 2407 (2013).

[103]. N. Estep, D. Sounas, J. Soric, and A. Alù, Magnetic-free non-reciprocity based on parametrically modulated coupled-resonator loops, Nat. Phys. 10, 923 (2014).

[104]. H. Lira, Z. Yu, S. Fan, and M. Lipson, Electrically Driven Nonreciprocity Induced by Interband Photonic Transition on a Silicon Chip, Phys. Rev. Lett. 109, 033901 (2012).

[105]. D. Wang, H. Zhou, M. Guo, J. Zhang, J. Evers, and S. Zhu, Optical Diode made from a Moving Photonic Crystal, Phys. Rev. Lett. 110, 093901 (2013).

[106]. S. Lepri and G. Casati, Asymmetric Wave Propagation in Nonlinear System, Phys. Rev. Lett. 106, 164101 (2011).

[107]. M. Soljacic, C. Luo, J. D. Joannopoulos, and S. Fan, Nonlinear photonic crystal microdevices for optical integration, Opt. Lett. 28, 637 (2003).

[108]. B. Liang, X. S. Guo, J. Tu, D. Zhang, J. C. Cheng, An acoustic rectifier, Nat. Mater. 9, 989 (2010).

[109]. N. Boechler, G. Theocharis, C. Daraio, Bifurcation-based acoustic switching and rectification. Nat. Mater. 10, 665 (2011).

[110]. L. M. Brekhovskikh, I. P. Lysanov, Fundamentals of Ocean Acoustics (Springer, Berlin, 2003).

[111]. Y. Xiao, B. R. Mace, J. Wen, and X. Wen, Formation and coupling of band gaps in a locally resonant elastic system comprising a string with attached resonators, Phys. Lett. A 375, 1485-1491 (2011).

[112]. Y.-F. Wang, V. Laude, and Y.-S. Wang, Coupling of evanescent and propagating guided modes in locally resonant phononic crystals, J. Phys. D: Appl. Phys. 47,

475502 (2014).

[113]. R. Fleury, D. L. Sounas, and A. Alu, Subwavelength ultrasonic circulator based on spatio-temporal modulation, Phys. Rev. B 91, 174306 (2015).

[114]. P. M. Morse and K. U. Ingard, Theoretical Acoustics, Princeton University Press, (1987).

[115]. A. Lakhtakia, V. K. Varadan, and V. V. Varadan, Green's functions for propagation of sound in a simply moving fluid. J. Acoust. Soc. A 85, 1852 (1989).

[116]. B. Edwards, A. Alu, M. E. Young, M. Silverinha, and N. Engheta, Experimental verification of epsilon-near-zero metamaterial coupling and energy squeezing using a microwave waveguide, Phys. Rev. Lett. 100, 033903 (2008).

[117]. I. Liberal, and N. Engheta, Near-zero refractive index photonics, Nat. Photon. 11, 149-158 (2017).

[118]. I. Liberal, A. M. Mahmoud, Y. Li, B. Edwards, and N. Engheta, Photonic doping of epsilon-near-zero media, Science 355, 1058-1062 (2017).

[119]. R. Fleury and A. Alu, Extraordinary sound transmission through density-near-zero ultranarrow channels, Phys. Rev. Lett. 111, 055501 (2013).

[120]. Y. Gu, Y. Cheng, X. Liu, Acoustic planar hyperlens based on anisotropic density-near-zero metamaterials, Appl. Phys. Lett. 107, 133503 (2015).

[121]. B. Poirier, C. Maury, J.-M. Ville, The use of Herschel-Quincke tubes to improve the efficiency of lined ducts, Appl. Acoust. 72, 78-88 (2011).

[122]. G. K. Bachelor, An Introduction to Fluid Dynamics, Cambridge University Press, (2000).

[123]. J. A. Kong, Theorems of bianisotropic media, Proc. IEEE 60, 1036-1046 (1972).

[124]. G. W. Milton, M. Briane, and J. R. Willis, On cloaking for elasticity and physical equations with a transformation invariant form, New J. Phys. 8, 248 (2006).

[125]. H. Nassar, X. C. Xu, A. N. Norris, and G. L. Huang, Modulated phononic crystals: Non-reciprocal wave propagation and Willis materials, J. Mech. Phys. Solids 101, 10 (2017).

[126]. F. Liu, X. Huang, and C. T. Chan, Dirac cones at $\vec{k} = 0$ in acoustic crystals and zero refractive index acoustic materials, Appl. Phys. Lett. 100, 071911 (2012).

[127]. M. Dubois, C. Shi, X. Zhu, Y. Wang, and X. Zhang, Observation of acoustic Dirac-like cone and double zero refractive index, Nat. Commun. 8, 14871 (2017).

[128]. D. A. Genov, S. Zhang and X. Zhang, Mimicking celestial mechanics in metamaterials, Nature Phys. 5, 687-692 (2009).

[129]. C. Sheng, H. Liu, Y. Wang, S. N. Zhu and D. A. Genov, Trapping light by mimicking gravitational lensing, Nat. Photon. 7, 902-906 (2013).

[130]. F. Qian, P. Zhao, L. Quan, X. Liu and X. Gong, Broadband acoustic omnidirectional absorber based on temperature gradients, Europhysics Letters, 107, 34009 (2014).

[131]. R.-Q. Li, X.-F. Zhu, B. Liang, Y. Li, X.-Y. Zhou and J.-C. Cheng, A broadband acoustic omnidirectional absorber comprising positive-index materials, Appl. Phys. Lett. 99, 193507 (2011).

[132]. A. Climente, D. Torrent and J. Sanchez-Dehesa, Gradient index lenses for flexural waves based on thickness variations, Appl. Phys. Lett. 105, 064101 (2014).

[133]. T. P. Martin, C. J. Naify, E. A. Skerritt, C. N. Layman, M. Nicholas, D. C. Calvo, G.

J. Orris, D. Torrent and J. Sanchez-Dehesa, Transparent gradient-index lens for underwater sound based on phase advance, Phys. Rev. Applied 4, 034003 (2015).

[134]. M. Z. Hasan and C. L. Kane, Colloquium: topological insulators, Rev. Mod. Phys. 82, 3045-3067 (2010).

[135]. X. Qi and S. Zhang, Topological insulators and superconductors, Rev. Mod. Phys. 83, 1057-1110 (2011).

[136]. K. V. Klitzing, G. Dorda, and M. Pepper, New method for high-accuracy determination of the fine-structure constant based on quantized Hall resistance, Phys. Rev. Lett. 45, 494 (1980).

[137]. Y. Zhang, Y. Tan, H. L. Stormer, and P. Kim, Experimental observation of the quantum Hall effect and Berry's phase in graphene, Nature 438, 201-204 (2005).

[138]. D. C. Tsui, H. L. Stormer and A. C. Gossard, Two-dimensional magnetotransport in the extreme quantum limit, Phys. Rev. Lett. 48, 1559 (1982).

[139]. K. I. Bolotin, F. Ghahari, M. D. Shulman, H. L. Stormer and P. Kim, Observation of the fractional quantum Hall effect in graphene, Nature 462, 196-199 (2009).

[140]. K. Fang, Z. Yu, and S. Fan, Photonic Aharonov-Bohm effect based on dynamic modulation, Phys. Rev. Lett. 108, 153901 (2012).

[141]. K. Fang, Z. Yu, and S. Fan, Realizing effective magnetic field for photons by controlling the phase of dynamic modulation, Nature Photon. 6, 782-787 (2012).

[142]. Q. Lin, and S. Fan, Light guiding by effective gauge field for photons, Phys. Rev. X 4, 031031 (2014).

[143]. Q. Lin, and S. Fan, Resonator-free realization of effective magnetic field for photons,

New J. Phys. 17, 075008 (2015).

[144]. Z. Yang, F. Gao, X. Shi, X. Lin, Z. Gao, Y. Chong, and B. Zhang, Topological acoustics, Phys. Rev. Lett. 114, 114301 (2015).

[145]. R. Fleury, A. B. Khanikaev, A. Alu, Floquet topological insulators for sound, Nat. Commun. 7, 11744 (2016).

[146]. C. He, X. Ni, H. Ge, X.-C. Sun, Y.-B. Chen, M.-H. Lu, X.-P. Liu and Y.-F. Chen, Acoustic topological insulator and robust one-way sound transport, Nat. Phys. 12, 1124 (2016).

[147]. Z. Zhang, Q. Wei, Y. Cheng, T. Zhang, D. Wu and X. Liu, Topological creation of acoustic pseudospin multipoles in a flow-free symmetry-broken metamaterial lattice, Phys. Rev. Lett. 118, 084303 (2017).

[148]. P. Zhang, T. Li, J. Zhu, X. Zhu, S. Yang, Y. Wang, X. Yin, and X. Zhang, Generation of acoustic self-bending and bottle beams by phase engineering, Nat. Commun. 5, 4316 (2014).

[149]. D. Baresch, J.-L. Thomas, and R. Marchiano, Observation of a single-beam gradient force acoustical trap for elastic particles: acoustical tweezers, Phys. Rev. Lett. 116, 024301 (2016).

[150]. J. Kim, S. Park, Y. Jung, S. Chang, J. Park, Y. Zhang, J. F. Lovell and C. Kim, Programmable real-time clinical photoacoustic and ultrasound imaging system, Sci. Rep. 6, 35137 (2016).

[151]. Y. Aharonov and D. Bohm, Significance of electromagnetic potentials in the quantum theory, Phys. Rev. 115, 485 (1959).

[152]. X. Ni, Y. Wu, Z.-G. Chen, L.-Y. Zheng, Y.-L. Xu, P. Nayar, X.-P. Liu, M.-H. Lu, Y.-F. Chen, Acoustic rainbow trapping by coiling up space, Sci. Rep. 4, 7038 (2014).

[153]. E. Feigenbaum, and H. A. Atwater, Resonant guided wave networks, Phys. Rev. Lett. 104, 147402 (2010).

[154]. E. Feigenbaum, and H. A. Atwater, Resonant guided wave networks, Phys. Rev. Lett. 104, 147402 (2010).

[155]. V. C. Nguyen, L. Chen, and K. Halterman, Total transmission and total reflection by zero index metamaterials with defects, Phys. Rev. Lett. 105, 233908 (2010).

[156]. N. M. Estakhri, and A. Alu, Recent progress in gradient metasurfaces, J. Opt. Soc. Am. B 33, A21 (2016).

[157]. H. T. Chen, A. J. Talor, and N. Yu, A review of metasurfaces: physics and applications, Rep. Prog. Phys. 79, 076401 (2016).

[158]. B. Assouar, B. Liang, Y. Wu, Y. Li, J.-C. Cheng, and Y. Jing, Acoustic metasurfaces, Nat. Rev. Mater. 3, 460-472 (2018).

[159]. Y. Tian, Q. Wei, Y. Cheng, and X. Liu, Acoustic holography based on composite metasurface with decoupled modulation of phase and amplitude, Appl. Phys. Lett. 110, 191901 (2017).

[160]. Y. Cheng, C. Zhou, B. G. Yuan, D. J. Wu, Q. Wei, and X. J. Liu, Ultra-sparse metasurface for high reflection of low-frequency sound based on artificial Mie resonances, Nat. Mater. 14, 1013 (2015).

[161]. A. V. Jildishev, A. Boltasseva, and V. M. Shalaev, Planar photonics with metasurfaces, Science 339, 1232009 (2013).

[162]. F. Monticone, N. M. Estakhri, and A. Alu, Full control of nanoscale optical transmission with a composite metascreen, Phys. Rev. Lett. 110, 203903 (2013).

[163]. N. M. Estakhri, and A. Alu, Manipulating optical reflections using engineered nanoscale metasurfaces, Phys. Rev. B 89, 235419 (2014).

[164]. S. Sun, Q. He, S. Xiao, Q. Xu, X. Li, and L. Zhou, Gradient-index meta-surfaces as a bridge linking propagating waves and surface waves, Nat. Mater. 11, 426 (2012).

[165]. Y. Xie, W. Wang, H. Chen, A. Konneker, B. I. Popa and S. A. Cummer, Wavefront modulation and subwavelength diffractive acoustic with an acoustic metasurface, Nat. Commun. 5, 5553 (2014).

[166]. Y. Li, B. Liang, Z. Gu, X. Zhou, and J. Cheng, Reflected wavefront manipulation based on ultrathin planar acoustic metasurfaces, Sci. Rep. 3, 2546 (2013).

[167]. B. Yuan, Y. Cheng, and X. Liu, Conversion of sound radiation pattern via gradient acoustic metasurface with space-coiling structure, Appl. Phys. Express 8, 027301 (2015).

[168]. N. M. Estakhri, and A. Alu, Wave-front transformation with gradient metasurfaces, Phys. Rev. X 6, 041008 (2016).

[169]. V. S. Asadchy, M. Albooyeh, S. N. Tcvetkova, A. Díaz-Rubio, Y. Ra'di, and S. A. Tretyakov, Perfect control of reflection and refraction using spatially dispersive metasurfaces, Phys. Rev. B 94, 075142 (2016).

[170]. A. Díaz-Rubio and S. A. Tretyakov, Acoustic metasurfaces for scattering-free anomalous reflection and refraction, Phys. Rev. B 96, 125409 (2017).

[171]. C. Pfeiffer and A. Grbic, Metamaterial Huygens' surfaces: tailoring wave fronts with reflectionless sheets, Phys. Rev. Lett. 110, 197401 (2013).

[172]. A. Epstein, and G. V. Eleftheriades, Huygens' metasurfaces via the equivalence principle: design and applications, J. Opt. Soc. Am. B 33, A31 (2016).

[173]. M. Kim, A. M. H. Wong, and G. V. Eleftheriades, Optical Huygens' metasurfaecs with independent control of the magnitude and phase of the local reflection coefficients, Phys. Rev. X 4, 041042 (2014).

[174]. J. Zhao, B. Li, Z. Chen, and C. Qiu, Manipulating acoustic wavefront by inhomogeneous impedance and steerable extraordinary reflection, Sci. Rep. 3, 2537 (2013).

[175]. J. Zhao, B. Li, Z. N. Chen, and C. Qiu, Redirection of sound waves using acoustic metasurfaces, Appl. Phys. Lett. 103, 151604 (2013).

[176]. A. Epstein, and G. V. Eleftheriades, Synthesis of passive lossless metasurfaces using auxiliary fields for reflectionless beam splitting and perfect reflection, Phys. Rev. Lett. 117, 256103 (2016).

[177]. A. Díaz-Rubio, V. Asadchy, A. Elsakka, and S. Tretyakov, From the generalized reflection law to the realization of perfect anomalous reflectors, Sci. Adv. 3, e1602714 (2017).

[178]. A. M. H. Wong and G. V. Eleftheriades, Perfect anomalous reflection with a bipartite huygens' metasurface, Phys. Rev. X 8, 011036 (2018).

[179]. M. Chen, E. Abdo-Sanchez, A. Epstein, and G. V. Eleftheriades, Theory, design, and experimental verification of a reflectionless bianisotropic Huygens' metasurface for wide-angle refraction, Phys. Rev. B 97, 125433 (2018).

[180]. V. Asadchy, A. Diaz-Rubio, S. Tretyakov, Bianisotropic metasurfaces: physics and applications. Nanophotonics, 7, 1069-1094 (2018).

[181]. J. Li, C. Shen, A. Díaz-Rubio, S. Tretyakov, and S. Cummer, Systematic design and experimental demonstration of bianisotropic metasurfaces for scattering-free manipulation of acoustic wavefronts, Nat. Commun. 9, 1342 (2018).

[182]. A. Diaz-Rubio, J. Li, C. Shen, S. A. Cummer, and S. A. Tretyakov, Power flow-conformal metamirrors for engineering wave reflections, Sci. Adv. 5, eaau7288 (2019).

[183]. A. Salandrino, and N. Engheta, Far-field subdiffraction optical microscopy using metamaterial crystals: Theory and simulations, Phys. Rev. B 74, 075103 (2006).

[184]. D. Lu, and Z. Liu, Hyperlenses and metalenses for far-field super-resolution imaging, Nat. Commun. 3, 1205 (2012).

[185]. A. Poddubny, I. Iorsh, P. Belov, and Y. Kivshar, Hyperbolic metamaterials, Nature Photon. 7, 948-957 (2013).

[186]. A. J. Hoffman, L. Alekseyev, S. S. Howard, K. J. Franz, D. Wasserman, V. A. Podolskiy, E. E. Narimanov, D. L. Sivco, and C. Gamachl, Negative refraction in semiconductor metamaterials, Nat. Mater. 6, 946-950 (2007).

[187]. A. S. Potemkin, A. N. Poddubny, P. A. Belov, and Y. S. Kivshar, Green function for hyperbolic media, Phys. Rev. A 86, 023848 (2012).

[188]. D. R. Smith, D. Schurig, J. J. Mock, P. Kolinko, and P. Rye, Partial focusing of radiation by a slab of indefinite media, Appl. Phys. Lett. 84, 2244 (2004).

[189]. Y. Liu, G. Bartal, and X. Zhang, All-angle negative refraction and imaging in a bulk medium made of metallic nanowires in the visible region, Opt. Express 16, 15439 (2008).

[190]. J. Yao, Z. Liu, Y. Liu, Y. Wang, C. Sun, G. Bartal, A. M. Stacy, and X. Zhang, Optical negative refraction in bulk metamaterials of nanowires, Science 321, 930 (2008).

[191]. A. Fang, T. Koschny, and C. M. Soukoulis, Optical anisotropic metamaterials: Negative refraction and focusing, Phys. Rev. B 79, 245127 (2009).

[192]. C. Shen, Y. Xie, N. Sui, W. Wang, S. A. Cummer, and Y. Jing, Broadband acoustic hyperbolic metamaterial, Phys. Rev. Lett. 115, 254301 (2015).

[193]. D. Torrent, and J. Sanchez-Dehesa, Acoustic cloaking in two dimensions: a feasible approach, New J. Phys. 10, 063015 (2008).

[194]. J. B. Pendry, and J. Li, An acoustic metafluid: realizing a broadband acoustic cloak, New J. Phys. 10, 115032 (2008).

[195]. A. N. Norris, Acoustic cloaking theory, Proc. R. Soc. A 464, 2411-2434 (2008).

[196]. Y. Cheng, X. Zhou, and G. Hu, Broadband dual-anisotropic solid metamaterials, Sci. Rep. 7, 13197 (2017).

[197]. J. S. Gomez-Diaz, M. Tymchenko, and A. Alu, Hyperbolic plasmons and topological transitions over uniaxial metasurfaces, Phys. Rev. Lett. 114, 233901 (2015).

[198]. A. A. High, R. C. Devlin, A. Dibos, M. Polking, D. S. Wild, J. Perczel, N. P. de Leon,

M. D. Lukin, and H. Park, Visible-frequency hyperbolic metasurface, Nature 522, 192-196 (2015).

[199]. J. S. Gomez-Diaz, and A. Alu, Flatland optics with hyperbolic metasurfaces, ACS Photonics 2016, 3 2211-2224 (2016).

[200]. X. Wu, X. Xia, J. Tian, Z. Liu, and W. Wen, Broadband reflective metasurface for focusing underwater ultrasonic waves with linearly tunable focal length, Appl. Phys. Lett. 108, 163502 (2016).

[201]. P. A. Belov, C. R. Simovski, and P. Ikonen, Canalization of subwavelength images by electromagnetic crystals, Phys. Rev. B 71, 193105 (2005).

[202]. P. A. Belov and Y. Hao, Subwavelength imaging at optical frequencies using a transmission device formed by a periodic layered metal-dielectric structure operating in the canalization regime, Phys. Rev. B 73, 113110 (2006).